

## INFORMATION TO USERS

This manuscript has been reproduced from the microfilm master. UMI films the text directly from the original or copy submitted. Thus, some thesis and dissertation copies are in typewriter face, while others may be from any type of computer printer.

**The quality of this reproduction is dependent upon the quality of the copy submitted.** Broken or indistinct print, colored or poor quality illustrations and photographs, print bleedthrough, substandard margins, and improper alignment can adversely affect reproduction.

In the unlikely event that the author did not send UMI a complete manuscript and there are missing pages, these will be noted. Also, if unauthorized copyright material had to be removed, a note will indicate the deletion.

Oversize materials (e.g., maps, drawings, charts) are reproduced by sectioning the original, beginning at the upper left-hand corner and continuing from left to right in equal sections with small overlaps.

ProQuest Information and Learning  
300 North Zeeb Road, Ann Arbor, MI 48106-1346 USA  
800-521-0600

UMI<sup>®</sup>



NEAR-FIELD COMBINATION APERTURES FOR ULTRA-RESOLUTION

OPTICAL STORAGE

by

Shu-Guo Tang

---

A Dissertation Submitted to the Faculty of the

COMMITTEE ON OPTICAL SCIENCES (GRADUATE)

In Partial Fulfillment of the Requirements  
For the Degree of

DOCTOR OF PHILOSOPHY

In the Graduate College

THE UNIVERSITY OF ARIZONA

2002

UMI Number: 3060954

UMI<sup>®</sup>

---

UMI Microform 3060954

Copyright 2002 by ProQuest Information and Learning Company.

All rights reserved. This microform edition is protected against  
unauthorized copying under Title 17, United States Code.

---

ProQuest Information and Learning Company  
300 North Zeeb Road  
P.O. Box 1346  
Ann Arbor, MI 48106-1346

THE UNIVERSITY OF ARIZONA ©  
GRADUATE COLLEGE

As members of the Final Examination Committee, we certify that we have  
read the dissertation prepared by Shu-guo Tang  
entitled Near-Field Combination Apertures for Ultra-Resolution  
Optical Storage

and recommend that it be accepted as fulfilling the dissertation  
requirement for the Degree of Doctor of Philosophy

Tom D. Milster  
Thomas D. Milster

8/19/02  
Date

Alan Kost  
Alan Kost

8/19/02  
Date

Michael R. Descour  
Michael R. Descour

8/19/2002  
Date

\_\_\_\_\_

\_\_\_\_\_  
Date

\_\_\_\_\_

\_\_\_\_\_  
Date

Final approval and acceptance of this dissertation is contingent upon  
the candidate's submission of the final copy of the dissertation to the  
Graduate College.

I hereby certify that I have read this dissertation prepared under my  
direction and recommend that it be accepted as fulfilling the dissertation  
requirement.

Tom D. Milster  
Dissertation Director, Thomas D. Milster

8/23/2002  
Date

## STATEMENT BY AUTHOR

This dissertation has been submitted in partial fulfillment of requirements for an advanced degree at The University of Arizona and is deposited in the University Library to be made available to borrowers under rules of the Library.

Brief quotations from this dissertation are allowable without special permission, provided that accurate acknowledgement of source is made. Requests for permission for extended quotation from or reproduction of this manuscript in whole or in part may be granted by the head of the major department or the Dean of the Graduate College when in his or her judgment the proposed use of the material is in the interests of scholarship. In all other instances, however, permission must be obtained from the author.

SIGNED: 

## ACKNOWLEDGEMENTS

I would like to express my heartily gratitude to Professor Tom Milster for his patience to instruct me on this research. He is not only a research adviser but also a true educator to me. Under his guidance, I built up my confidence and found my ability. The gratitude is also given to our group members Yan Zhang and Mellisa Bailey for their tutors on FDTD simulation tools. I also thank to our group technical staff John Butz for his idea and advice to improve my experiment setup. Many thanks to the group member Jason Curtis for his assistance to setup experiment devices. Many thanks to the group member Rose Early for her help computer programs. Special thanks to Kevin Erwin and Warren Bletscher for their professional supports in the mechanical and the electronic design.

I would like to express my deeply felt gratitude to my wife Sandy for her support and companionship through out the graduate school years. I owe her more than I can repay for the rest of my life. I also acknowledge my daughter Sarah. She is the source of motivation that pushes me to face any challenge and difficulty during my graduate study. I thank my twin brother Shu-Jung for his continuous encouragement since we were in college. He always offers me spiritual supports whenever I need. I also thank my mother and in-laws for their unconditional help and faith in me.

**This dissertation is dedicated to the greatest person in my life.**

**My father**

**Lin-Chuan Tang,**

**for his constant love and faith in me.**

## TABLE OF CONTENTS

LIST OF ILLUSTRATIONS .....	8
LIST OF TABLES .....	13
ABSTRACT .....	14
1. INTRODUCTION .....	15
1.1 Basic Description of Device under Investigation .....	15
1.2 Contents of the Dissertation .....	21
1.3 Original Contributions .....	21
2. BACKGROUND .....	23
2.1 The Near-field Technology for Microscopy .....	23
2.2 The Near-field Technology for Optical Recording .....	26
2-3 Present SIL and Aperture Probe Technologies for Data Storage .....	29
3. THEORY AND DESIGN.....	32
3.1 Introduction .....	32
3.2 Illumination .....	34
3.3 Signal Detection .....	46
3.4 The Design of Combination Apertures .....	50
3.4.1 APSIL .....	50
3.4.2 Al aperture + SIL .....	56
3.5 Summary .....	61
4. FABRICATIONS AND TEST OF COMBINATION APERTURES	63
4.1 Introduction .....	63
4.2 Fabrication of an APSIL .....	64
4.3 APSIL Experiment .....	64
4.4 Fabrication of Al Aperture + SIL .....	71
4.5 Al Aperture + SIL Experiment .....	73

## TABLE OF CONTENTS-*Continued*

4.6 Summary .....	75
<b>5. HIGH-DENSITY RECORDING ON A PHASE-CHANGE MEDIUM BY AN APSIL .....</b>	<b>76</b>
5.1 Introduction .....	76
5.2 Experiment Setup and Near-Field Recording Medium .....	77
5.3 Tracking Error Signal .....	79
5.4 Recording Experiment .....	82
5.4.1 Static Recording .....	83
5.4.2 Non-Static Recording and Read Back .....	86
5.5 Summary .....	91
<b>6. CONSIDERATION AND CONTROL OF WRITING CONDITIONS WITH AN APSIL PROBE .....</b>	<b>92</b>
6.1 Introduction .....	92
6.2 Polarization Effect .....	93
6.3 Axial Focus Position .....	98
6.4 Transverse Misalignment .....	100
6.5 Summary .....	104
<b>7. CONCLUSIONS AND FUTURE WORK .....</b>	<b>105</b>
7.1 Summary of the Dissertation .....	105
7.2 Significant results from an APSIL .....	108
7.2 Suggestions for Future Work .....	109
<b>8. REFERENCES .....</b>	<b>111</b>

## LIST OF ILLUSTRATIONS

<b>Figure 1-1.</b> System for near-field recording using a solid immersion lens (SIL). ...	16
<b>Figure 1-2.</b> System for near-field recording using an aperture probe. ....	19
<b>Figure 1-3.</b> (a) Geometry of the APSIL. (b) Geometry of the metallic aperture + SIL. ....	20
<b>Figure 2-1.</b> Conceptual schematic of the near-field aperture probe. ....	24
<b>Figure 2-2.</b> Schematic of the solid immersion lens (SIL). Light from the objective lens is focused on the flat surface of the hemispherical lens without refraction at the curved interface. ....	25
<b>Figure 2-3.</b> Schematic of the aperture probe implemented with an aluminum-coated pulled glass fiber. ....	26
<b>Figure 2-4.</b> Schematic of the supersphere SIL. Light from the objective lens is bent on the curve surface of the truncated spherical lens and then focused on the bottom. ....	27
<b>Figure 2-5.</b> The experiment uses a glass slider with a supersphere SIL. Both the SIL and slider are made from LaSFN9 glass. ....	28
<b>Figure 3-1.</b> Schematic of a near-field transducer with an illumination objective lens. ....	34
<b>Figure 3-2.</b> FDTD simulation results of angular dependence of the transmitted irradiance distribution for (a) TE and (b) TM polarization, respectively. The transmitted irradiance distribution is from a 100 nm circular hole in an ideal metal. ....	36
<b>Figure 3-3.</b> Peak irradiance of each transmitted distribution in Figs. 3-2. ....	37
<b>Figure 3-4.</b> Comparison between FDTD and Bethe's prediction on the square of transmitted field $ u'_0(0,0) \cdot K(\alpha, \beta) ^2$ for unit amplitude plane wave illumination versus incidence angle through a circular hole in perfect conducting screen. ....	41

## LIST OF ILLUSTRATIONS-*Continued*

<b>Figure 3-5.</b> Illumination setting used in the FDTD simulation. ....	42
<b>Figure 3-6.</b> Profiles of $K(\alpha)$ for several transducers using (a) TE (b) TM polarized illumination. Geometries are described in Table 3-1. ....	44
<b>Figure 3-7.</b> Displays of the power transmission versus illumination NA for the geometries listed in Table 3-1. ....	46
<b>Figure 3-8.</b> The basic process of detection is shown for a DVD system. In angular (frequency) space, the overlap of the diffracted orders determines the signal contrast. ....	47
<b>Figure 3-9.</b> Angular spectra of several detection geometries. (a) SIL only; (b) aperture only; (c) aperture + SIL. Notices that the combination of an aperture and a SIL produces the most overlap area and highest contrast. ....	49
<b>Figure 3-10.</b> FDTD simulation results of individual normalized spot profiles from the APSIL in Table I for (a) TE and (b) TM polarization when the incident angle $\theta_m = 0^\circ, 12^\circ, 25^\circ, 37^\circ$ , and $50^\circ$ . ....	51
<b>Figure 3-11.</b> FDTD simulation results of individual normalized spot profiles in air for (a) TE and (b) TM illumination at incident angle $\theta_m = 37^\circ$ when the wall angle $\theta = 0^\circ, 9^\circ, 14^\circ, 20^\circ$ , and $26^\circ$ . ....	53
<b>Figure 3-12.</b> FDTD simulation results of spot profiles in air for (a) TE and (b) TM illumination at incident angle $\theta_m = 0^\circ$ when the wall angle $\theta = 0^\circ, 9^\circ, 14^\circ, 20^\circ$ , and $26^\circ$ . ....	54
<b>Figure 3-13.</b> FDTD simulation results of spot profiles in air for (a) TE and (b) TM illumination at incident angle $\theta_m = 0^\circ$ when the wall angle $\theta = 9^\circ$ and probe size $d_1 = 100$ nm, 200 nm, and 300 nm. ....	55
<b>Figure 3-14.</b> FDTD simulation results of individual normalized spot profiles from the AL aperture + SIL in Table I for (a) TE and (b) TM polarization when the incident angle $\theta_m = 0^\circ, 12^\circ, 25^\circ, 37^\circ$ , and $50^\circ$ . ....	57

## LIST OF ILLUSTRATIONS-Continued

<b>Figure 3-15.</b> FDTD simulation results of individual normalized spot profiles in air for (a) TE and (b) TM illumination at incident angle $\theta_m = 37^\circ$ when the thickness of Al $t = 30$ nm and 100 nm. ....	58
<b>Figure 3-16.</b> FDTD simulation results of spot profiles in air for (a) TE and (b) TM illumination at incident angle $\theta_m = 0^\circ$ when the thickness of Al $t = 30$ nm and 100 nm. ....	59
<b>Figure 3-17.</b> Aperture geometry used in the FDTD simulation. ....	60
<b>Figure 4-1.</b> Fabrication process for dielectric aperture probes (APSIL) combined with a SIL. ....	64
<b>Figure 4-2.</b> Detailed composite schematic of the NEFUS. ....	66
<b>Figure 4-3.</b> Two distinct pupil images from the (a) far field system (NA = 0.5) (b) SIL system (NA = 0.95) (c) APSIL system (NA = 2.4) when the grating translates. ....	68
<b>Figure 4-4.</b> The readout signals from the systems of far field, SIL and APSIL when scanning the groove edge in a phase grating of $1.6 \mu\text{m}$ pitch. ...	70
<b>Figure 4-5.</b> The readout signals from the systems of far field, SIL and APSIL when scanning a big mark on the phase-change medium. ....	71
<b>Figure 4-6.</b> Fabrication process for Al aperture array combined with SIL. ....	72
<b>Figure 4-7.</b> Image of the FIB-fabricated aperture array and a closeup of one aperture. The size of each aperture is approximately $200 \text{ nm} \times 350 \text{ nm}$ . The completed Al aperture + SIL is also shown with the array illuminated with a laser beam. ....	73
<b>Figure 4-8.</b> Surface quality of the Al apertures on the back of SIL tested by a Wyko NT-2000 interferometer. ....	74
<b>Figure 5-1.</b> Schematic of the modified NEFUS for optical recording. ....	77
<b>Figure 5-2.</b> Composite layers of the recording medium for near-field recording. ...	78

## LIST OF ILLUSTRATIONS-Continued

<b>Figure 5-3.</b> Schematic of push-pull tracking error signal generation. ....	80
<b>Figure 5-4.</b> Tracking error signal from the phase-change medium of 1.6 $\mu\text{m}$ track pitch. ....	81
<b>Figure 5-5.</b> Tracking error signal from the phase grating of 0.4 $\mu\text{m}$ track pitch. ....	82
<b>Figure 5-6.</b> Visible light microscope image of three series of marks written along the vertical tracks of a phase-change medium by the systems of APSIL, far field and SIL, respectively (from left to right). ....	84
<b>Figure 5-7.</b> Microscope image of a matrix of recorded marks by the static recording. The power is measured from the object lens. The "x" sign in the matrix represents an overexposed mark. ....	85
<b>Figure 5-8.</b> Microscope image of non-static recording marks and their readout signal. The marks are recorded on a groove of the phase-change medium with 1 $\mu\text{m}$ spacing. ....	87
<b>Figure 5-9.</b> Microscope image of non-static recording marks and their readout signal. The marks are recorded on a groove of the phase-change medium with 500 nm spacing. ....	88
<b>Figure 5-10.</b> The readout signal from a series of marks with (a) 333 nm spacing and (b) 250 nm spacing. ....	89
<b>Figure 5-11.</b> Experimental modulation transfer function (MTF) of the APSIL system. The cutoff frequency is beyond 4 $\mu\text{m}^{-1}$ . ....	90
<b>Figure 6-1.</b> FDTD simulation results of spot profile in air for TE and TM polarizations when the illumination of a current source is normal incident. ....	94
<b>Figure 6-2.</b> Experimental setup for the edge-scan test. ....	95
<b>Figure 6-3.</b> Experimental edge-scan results for TE and TM polarization. ....	95

**LIST OF ILLUSTRATIONS-Continued**

**Figure 6-4.** Mark-scan profiles for data written with (a) TE and (b) TM polarizations. The readout polarization is in the TE direction. .... 97

**Figure 6-5.** Edge-scan results for the axial focus position of the objective lens at the entrance plane of the probe and exit plane of the probe. The readout polarization is in the TE polarization. .... 99

**Figure 6-6.** Line-scan profile of two marks written by the focus position at the entrance plane and exit plane. Polarization of the write beam and readout beam are in the TE direction. .... 100

**Figure 6-7.** Comparison between results from simulation and experiment with respect to spot size change when the polarization is TE. .... 102

**Figure 6-8.** Comparison between results from simulation and experiment with respect to spot position shift relative to the center of the probe when the polarization is TE. .... 103

## LIST OF TABLES

<b>Table 3-1.</b> Geometries of transducers investigated by FDTD simulations .....	43
<b>Table 3-2.</b> The results of $ u'_0(0,0) ^2$ for the transducers in Table 3-1 .....	43
<b>Table 3-3.</b> Detailed results from FDTD study on AI aperture + SIL .....	61

## ABSTRACT

This dissertation proposes and demonstrates an innovative technique for ultra-resolution data storage. An original idea that combines two near-field techniques, aperture probes and the solid immersion lens (SIL), is implemented through modeling, fabrication, testing, phase-change recording, and writing condition studies.

In the modeling, a theory for illumination and signal detection is presented. The power transmission for different near-field transducers illuminated by a lens is calculated versus  $NA$ . In detection, the angular spectrum illustrates advantages of the combination aperture system. In addition, geometrical design considerations are discussed with the modeling. Nearly optimal designs for APSIL and AI aperture + SIL are presented for the illumination wavelength 488 nm.

Fabrication techniques are developed for dielectric probe + SIL, which is called APSIL, and AI aperture + SIL, respectively through modeling geometrical design. Both near-field transducers are tested by edge-scan experiments. Spot size and optical efficiency from the APSIL system are evaluated.

APSIL is evaluated for high-density recording on a phase-change medium. Minimum mark size and the modulation transfer function (MTF) are obtained experimentally. Control of writing conditions for an APSIL system are investigated with respect to polarization, axial focus position and transverse beam alignment. Our study shows that the APSIL system achieves much higher optical efficiency than aperture probe systems as well as exhibits better resolution than SIL systems.

## Chapter 1

### INTRODUCTION

Optical disk, in particular read-only compact discs (CDs) and digital versatile disks (DVDs), are popular for software, music and video distribution, where large amounts of digital information are mass replicated in an inexpensive removable format. Optical disks are also popular as recording devices in the formats of compact-disc-recordable (CD-R) and compact-disc-rewritable (CD-RW). Other formats, including DVD-R and DVD-RW, are just beginning to make a significant penetration into the marketplace for large capacity storage. As optical disks evolve, their data capacity increases [Tieke *et al.* 1999]. For example, the data capacity of a single-layer DVD (4.7 GB) is a factor of 7.3 more than that of a CD (0.64 GB). The CD and DVD devices use the mechanism of far-field recording. This dissertation presents a new technique based on a mechanism called near-field recording to extend the capacity of optical disks well beyond what is found in CD and DVD.

#### 1-1 Basic Description of the Device under Investigation

Both solid immersion lenses (SILs) and aperture probes are currently being developed as near-field data storage techniques [Terris *et al.* 1994], [Betzig *et al.* 1992] which utilize evanescent energy to produce extremely small optical spots. SIL systems, while offering smaller spots than a conventional far-field system, do not have the resolution observed from aperture probes. However, aperture probes suffer from low

throughput, limiting the optical efficiency. This dissertation presents a new technique that combines a SIL and an aperture probe. The combination aperture can achieve higher performance (in terms of spot size and efficiency) for optical data storage and microscopy than those observed when the SIL or the aperture probe is used alone.

A typical arrangement for the SIL system is shown in Figure 1-1. A SIL, hemispherical lens, is placed in near contact with the recording layer. Light from a laser passes through the beam splitter and is focused onto the bottom of the SIL by an objective lens. An evanescent field generated from the bottom of SIL causes a small light spot on the recording layer. A moving recording layer with tracks of data marks is shown. Light from the spot is collected by the objective lens, passes through the beam splitter, and is detected by the detector. The detector output is a current signal  $i(t)$  which is a periodic waveform with a maximum value  $i_{MAX}$  and a minimum value  $i_{MIN}$ .

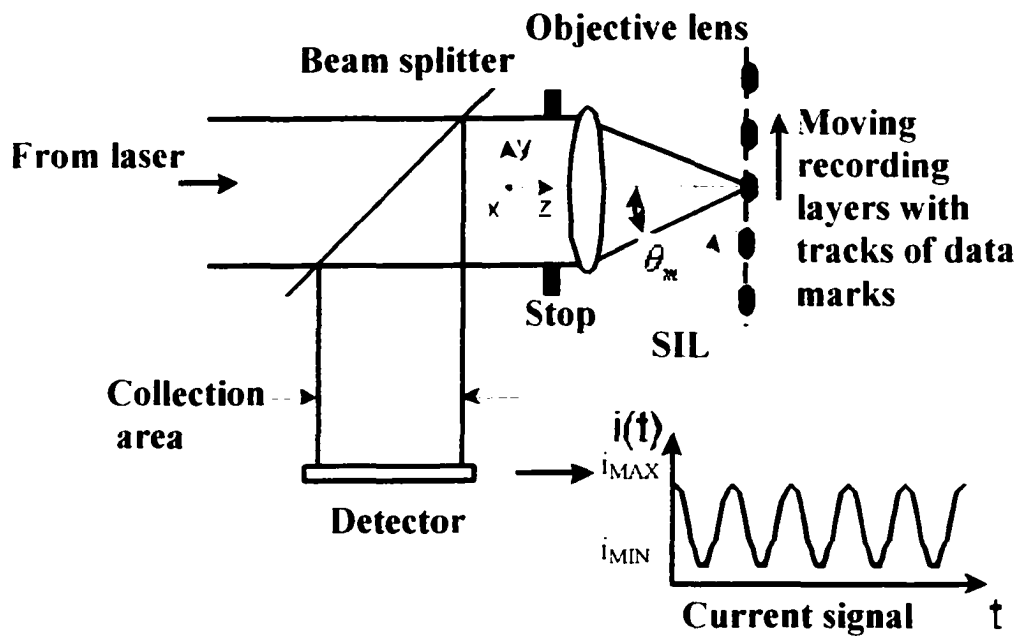


**Figure 1-1.** System for near-field recording using a solid immersion lens (SIL).

Recording layers are on a disk that spins under the objective lens. Recording layers contain spiral tracks of mark patterns that differ in reflectivity from the area between marks. As the focused laser beam passes over a mark, the reflected light level changes. Changes in the reflected light level are sensed by using the beam splitter to direct a portion of the reflected light onto a detector. The detector current, which is a representation of the mark pattern, is decoded to produce digital information. The fidelity of the detector signal determines the amount of data per unit length of track that can be decoded with high reliability.

There are several factors that influence fidelity of the detector signal. The most important factor for closely-spaced marks is the focused spot size  $s$ . Large  $s$  blurs the reflected light signal, resulting in a loss of contrast  $V$  in the detector signal. Contrast is defined as  $V = (I_{MAX} - I_{MIN}) / (I_{MAX} + I_{MIN})$ , where  $I_{MAX}$  and  $I_{MIN}$  are shown in Fig. 1-1. Conversely, if  $s$  is small, changes in the reflected signal are sharp as the marks traverse under the spot. Therefore, as  $s$  decreases, the contrast and fidelity increase. Increased fidelity and contrast lead to smaller detectable changes in the mark pattern, so smaller marks can be used and more data can be packed into each track. That is, the capacity  $\propto 1/s^2$ . In addition, for systems that are limited by media noise, the signal-to-noise ratio is maximized by maximizing contrast.

Unfortunately,  $s$  cannot be made arbitrarily small. Due to the physics of diffraction, the minimum spot size  $s$  for SIL systems is a function of the wavelength of the laser  $\lambda$ , the focusing properties of the objective lens, system aberrations, and the thin-film structure used as the recording layer [Milster *et al.* 1999]. A simple relationship

that is used to estimate the full-width-at- $1/e^2$  spot size for conventional gaussian illumination [Haskal 1979] at the stop is  $s = \lambda/n\sin\theta_m = \lambda/(n\alpha_m)$ , where  $\lambda$  is the wavelength in air.  $\theta_m$  is the marginal ray angle, and  $n$  is the refractive index of the SIL. A marginal ray passes just at the edge of the stop, which is the limiting aperture of the system.  $\alpha_m$  is the direction cosine corresponding to the marginal ray angle.  $\alpha_m = \sin\theta_m$ . The value of  $n\alpha_m$  is the effective numerical aperture  $NA_{EFF}$  of the system. Since  $n = 1$  in far-field systems, the spot size in SIL systems can be  $n$  times smaller. As  $NA_{EFF}$  increases or  $\lambda$  decreases, the spot size  $s$  gets smaller, and mark density can increase.

An aperture probe system is shown in Fig. 1-2. An aperture of diameter  $d < \lambda$  is placed in proximity to the recording layer due to the rapid decay of the evanescent field from the aperture. The mark pattern is scanned by the aperture. Illumination for the aperture can be from a fiber waveguide or a lens. Size of the light spot interacting with the marks is mainly determined by  $d$ , so a very small spot can be generated regardless of the wavelength. However, the efficiency is very low due to the constraint of the small aperture. Reflected light collected by the objective lens is passed to the detector, where the current signal is decoded to produce digital information. Like with the SIL system, smaller spots yield higher contrast and greater data density.

Two proposed geometries of combination apertures are shown in Fig. 1-3 (a) and (b), respectively. Figure 1-3 (a) shows a tapered aperture transducer attached to the bottom of a SIL, which is called an APSIL transducer, with wall angle  $\theta$ , height  $h$ , and aperture size  $d_1$  of the transducer. Figure 1-3 (b) shows a single hole in a metal

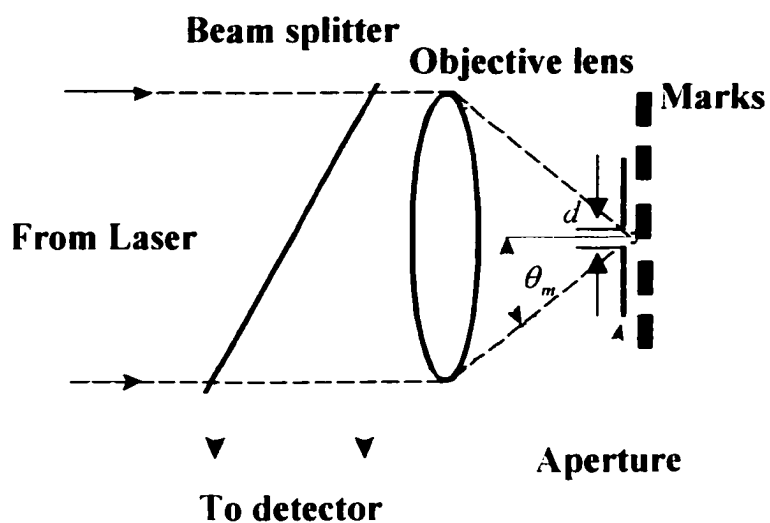


**Figure 1-2.** System for near-field recording using an aperture probe.

screen attached to the bottom of the SIL (metallic aperture + SIL) with hole size  $d_2$  and screen thickness  $t$ . Both of these systems are studied in this dissertation.

An optical system that combines a SIL with a transducer exhibits certain advantages. The spot size  $s$  is mainly determined by the transducer size. Optical efficiency is greatly improved over the transducer alone, because the light spot illuminating the transducer is smaller than is possible with fiber-based or far-field illumination. A second fundamental advantage of the combination aperture is in the detection process. In order to understand this improvement, consider the aperture-only system, where poor contrast is a result of the collection system not gathering enough

angular range. With the combination aperture system, larger angular range is possible, and improved contrast can result.

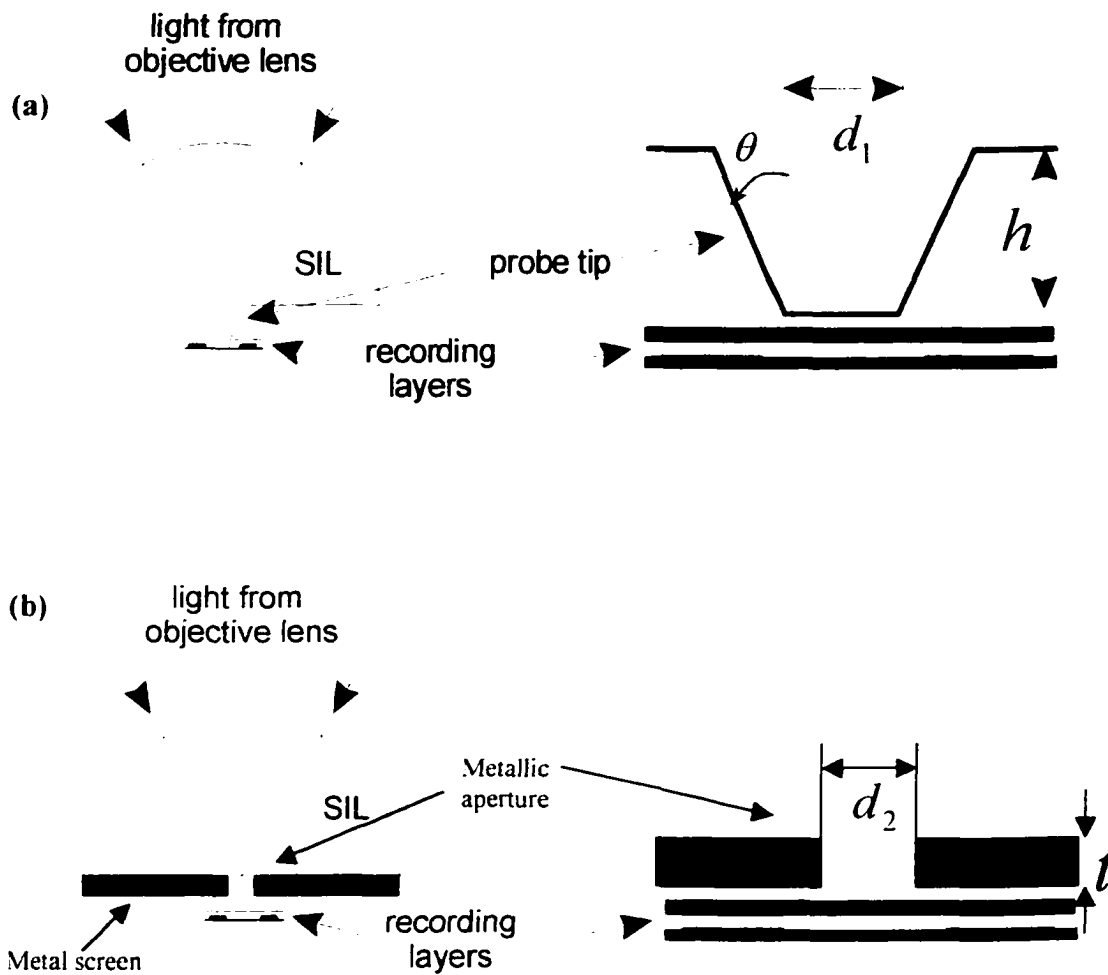


**Figure 1-3:** (a) Geometry of the APSIL. (b) Geometry of the metallic aperture + SIL.

## **1-2 Dissertation Contents**

The dissertation is organized as follows. Chapter 2 provides background of near-field techniques. The first category includes early theories and techniques of aperture probes and SILs for microscopy. The second category includes techniques of aperture probes and SILs for optical recording. The third category includes present techniques of aperture probes and SILs for data storage. Chapter 3 presents simple linear models that describe the advantage of combining a SIL with an aperture probe for data storage from the aspects of spot generation and signal detection. Chapter 3 also provides geometrical design considerations of the APSIL and the metallic aperture + SIL. Chapter 4 presents the fabrication procedure and test results of the APSIL and the metallic aperture + SIL. The spot size and optical efficiency from both systems are evaluated. Chapter 5 presents phase-change recording with the APSIL system. Minimum mark size and modulation transfer function (MTF) are evaluated. Tracking capability is also discussed. Chapter 6 discusses the control of writing conditions with the APSIL with respect to polarization, axial focus and transverse misalignment. Chapter 7 presents a summary of the major results and findings of this dissertation, as well as suggestions for future work.

## **1-3 Original Contributions**

A great deal of work has been done to reduce the spot size beyond the diffraction limit by researchers. However, none of them can actually achieve extremely small spot size without greatly affecting the optical efficiency. We present an innovative idea that combines a dielectric aperture probe and SIL to overcome this difficulty. Following a

basic description of the idea, the methods of modeling, fabrication, and testing are developed step by step for illustrating advantages of the combination technique. Through systematic study, APSIL probes achieve 200 nm  $1/e^2$  full-width spot size, 125 nm mark size and 50% optical efficiency in reflection due to the nearly optimum geometry we choose for 488nm wavelength illumination. Thus, the potential of using APSIL probes in optical data storage is estimated. Our goal is to provide a good choice to for a data storage technique for ultra high-density recording.

## Chapter 2

### BACKGROUND

This chapter presents background of near-field technology. The developments of aperture probes and SILs for microscopy and optical data storage are discussed.

#### 2-1 The Near-field Technology for Microscopy

The first proposal that uses a near-field scanning aperture to overcome the diffraction limit on resolution is in a paper by Synge [Synge 1928]. He proposed a sub-wavelength hole be constructed on an opaque screen and illuminated from below. Such an aperture probe is shown conceptually in Fig. 2-1. As shown in the figure, the aperture with the diameter  $d$  was placed immediately beneath the test sample, so the distance  $h$  between the aperture and the sample is only a fraction of aperture size. The light from the hole, after passing through the sample, is focused through a microscope upon a detector. When the sample moved in the plane relative to the stationary aperture, the super-resolution image of the sample can be plotted out through the detector current.

Bethe [Bethe 1944] provides a rigorous solution of the diffracted electromagnetic field from a single sub-wavelength hole on a perfect conducting screen. He predicts that the power transmission of the field radiation, normalized to the hole area, falls as the fourth power of the ratio of the hole radius to the radiation wavelength.

The first experimental demonstration of near-field microscopy was conducted in the microwave region by Ash and Nicholls [Ash and Nicholls 1972] who used a

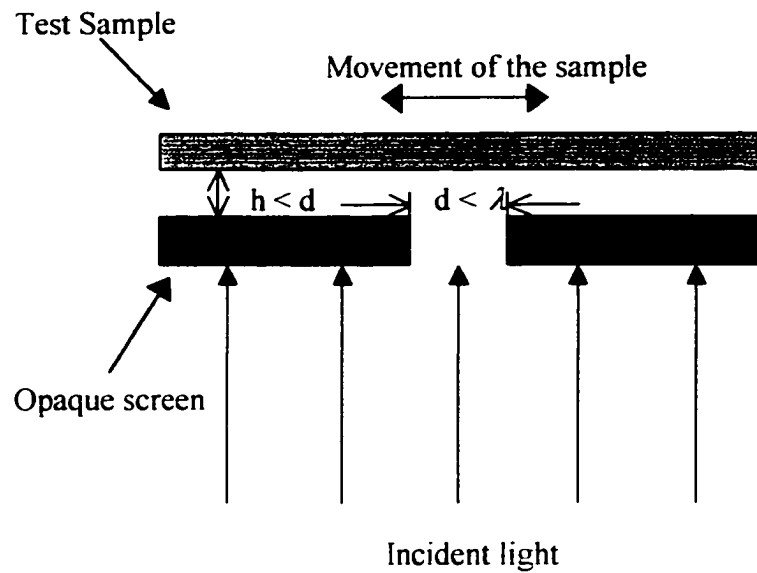


**Figure 2-1.** Conceptual schematic of the near-field aperture probe

wavelength of 3 cm and an aperture diameter of  $\lambda/20$ . They imaged features as small as  $\lambda/60$  using grating object of aluminum lines on glass.

Pohl *et al.* [Pohl *et al* 1984], at IBM-Zurich, demonstrated the first optical near-field microscope using a probe fabricated from a chemically etched quartz crystal rod coated with a metal shell. The exact aperture size and shape could not be verified, but Pohl *et al* claimed a resolution of  $\lambda/20$  when imaging with a source wavelength of 488 nm.

Researchers at Cornell University also contributed to the development of near-field technology. Harootunian *et al.* [1986] first demonstrated near-field scanning optical microscopy (NSOM) in the fluorescence mode by using a tapered metal-clad glass

pipettes. A 50 nm aperture can be fabricated by heating and pulling the glass pipettes. Collection mode operation with the pipette probes was reported by the Cornell group the following year [Betzig *et al.* 1987], and the IBM-Zurich group demonstrated reflection mode operation shortly thereafter [Fischer *et al.* 1989].

A near-field microscope with a solid immersion lens (SIL) was introduced by Mansfield and Kino [Mansfield and Kino 1990]. The SIL is a hemispherical glass lens with a refractive index  $n$  shown in Fig. 2-2. With the hemisphere, light from the objective lens is focused on the flat surface without refraction at the curved interface. The test sample is placed in near contact with the flat surface. The spot size improvement over the objective lens without the SIL is a factor of  $n$ . In an edge-response experiment, they used a SIL with a refractive index  $n = 2$  and illumination wavelength of 436 nm to achieve the resolution two times better than a far-field microscope.

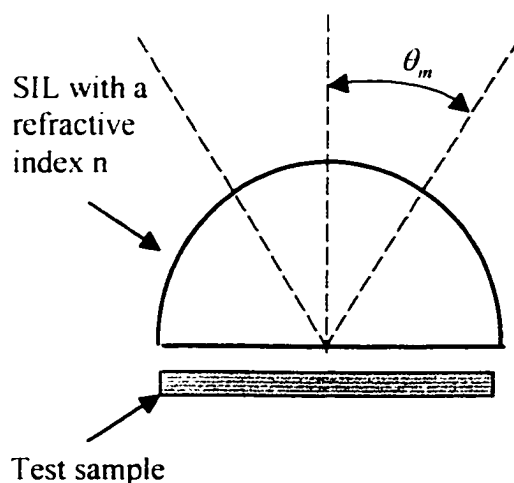


**Figure 2-2.** Schematic of the solid immersion lens (SIL). Light from the objective lens is focused on the flat surface of the hemispherical lens without refraction at the curved interface.

## 2-2 The Near-field Technology for Optical Recording

The first sub-wavelength aperture probe system for optical recording was proposed and demonstrated by Betzig *et al.* [Betzig *et al.* 1992]. In the Betzig design, the aperture is formed from a pulled optical fiber that is coated with aluminum, as shown in Figure 2-3. All but the very end of the probe tip is coated, resulting in an aperture diameter of  $\sim 50$  nm. The Al coating absorbs the exponential tail of the waveguide mode. Betzig's instrument was used to write 60 nm domains in magneto-optic material with the tip-material separation 10 nm. Data density of  $\sim 45$  Gbits/in<sup>2</sup> was achieved. However, the system suffers from very low efficiency ( $10^{-5}$ ). Thus, the data rate was limited to 10 kHz or less, which is not comparable to the commercial optical disks. Terris *et al.* [Terris *et al.* 1994] introduced a new type SIL for optical recording. The new type SIL called supersphere is a truncated glass sphere shown in Figure 2-4. As shown in the figure, the supersphere

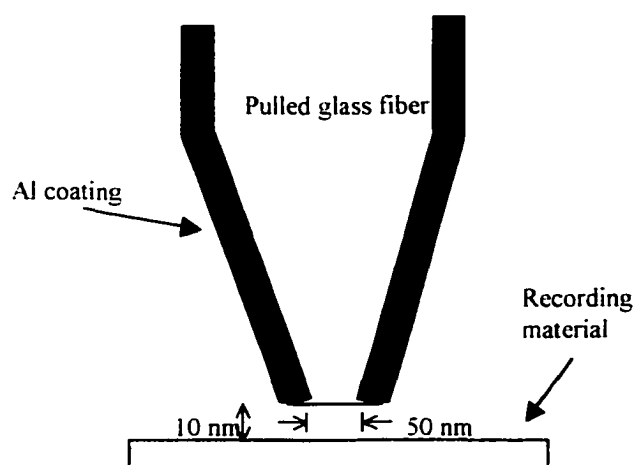


**Figure 2-3.** Schematic of the aperture probe implemented with an aluminum-coated pulled glass fiber.

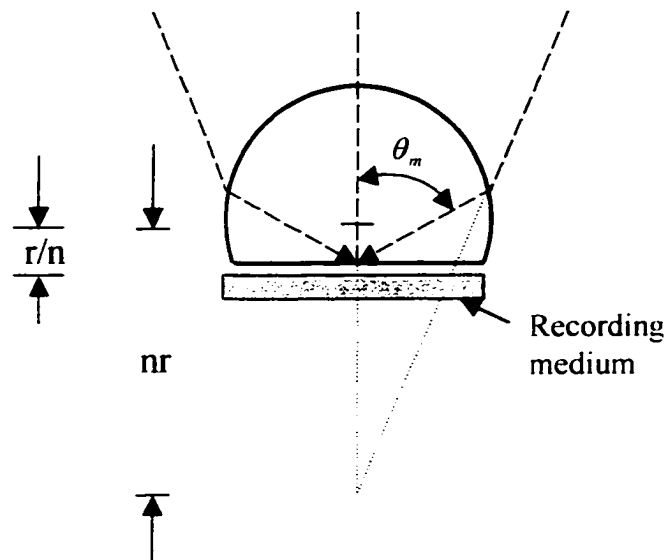


**Figure 2-4.** Schematic of the supersphere SIL. Light from the objective lens is bent on the curve surface of the truncated spherical lens and then focused on the bottom.

bends the light at the curved surface. Thickness of the supersphere is  $r(1 + 1/n)$ , where  $r$  is the radius of the curved surface. The SIL is positioned so that the center of the sphere is located a distance  $nr$  from the focal point of the objective lens in air. Spot size improvement over the objective lens is  $n^2$ . Using the supersphere with  $n = 1.83$  and illuminating with 780 nm light, a 388 nm  $\text{FWI}/e^2$  spot size was produced. In addition, a 500 nm period grating was resolved, and 350 nm diameter magnetic domains were written and read. The first published dynamic demonstration of SIL technology is

presented by Terris *et al.* [Terris *et al.* 1996]. An objective lens focuses into a SIL of supersphere type mounted on a glass slider, as shown in Figure 2-4. The slider is ion milled to create

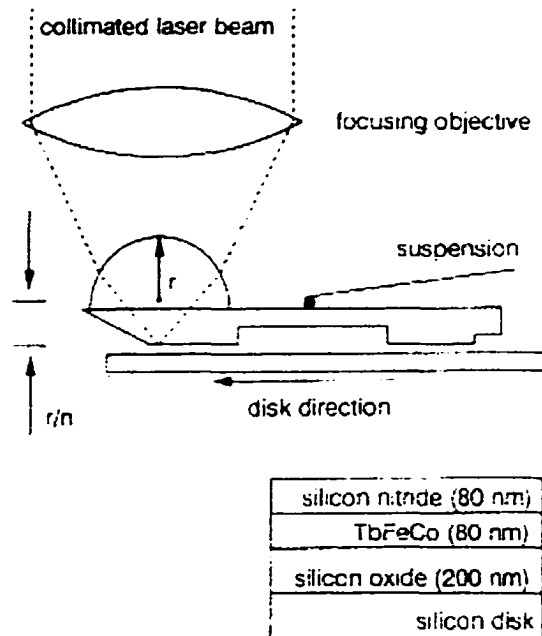


**Figure 2-5.** The experiment uses a glass slider with a supersphere SIL. Both the SIL and slider are made from LaSFN9 glass [Terris *et al.* 1996].

guiding surfaces for the air bearing that regulates distance between the focus point in the SIL and recording layer. A three-layer magneto-optic material recording layer with a silicon substrate is used. In the Terris experiment, 600 nm FW  $1/e^2$  spot size is measured with  $n = 1.83$  and illumination wavelength 830 nm. The highest density achieved is with 560 nm mark length and 700 nm track pitch, which implies a data density of 2.1 Gbits/in<sup>2</sup>.

### 2-3 Present SIL and Aperture Probe Technologies for Data Storage

Many researchers continue to work on the SIL and aperture probes for optical data storage. Hirota *et al.* [Hirota *et al.* 1998] demonstrated phase-change recording with a SIL and 830 nm wavelength illumination. 500 nm minimum mark length is achieved. Shimura *et al.* [Shimura *et al.* 2000] presented a pupil-plane filtering method for improving the contrast of detected signals in a SIL system. He showed that the reflected light off either the crystalline state or the amorphous state of a phase-change recording layer is not uniformly distributed on the pupil. By placing a x-shaped mask at the pupil of the system, the contrast of the detected signal increases. The most significant progress on a SIL data storage system is done by Sony Corporation in Japan. Ichimura *et al.* [Ichimura *et al.* 2000] dynamically demonstrated near-field recording in a customized phase-change disk with a supersphere SIL of refractive index 1.8 and illumination wavelength of 657 nm. The resulting effective numerical aperture ( $NA_{EFF}$ ) is 1.36. In the Ichimura experiment, the SIL is mounted on an electromagnetic positioning actuator above a spinning disk. An active capacitance gap servo can precisely control the air gap between the bottom of the SIL and the disk to be less than 50 nm. Ichimura also developed a near-field phase-change layer structure through a modulation transfer function (MTF) simulation. A dielectric stack of  $\text{SiO}_2/\text{SiN}/\text{SiO}_2$  is optimized with the recording layer to improve the MTF for near-field optical recording with the existence of an air gap. A 167 nm minimum mark size and areal recording density of 20 Gbits/in<sup>2</sup> are achieved. The data rate is 30 MHz. After two years, Kishima *et al.* [Kishima *et al.* 2002] in Sony Corporation used the same experiment setup but a 1.5  $NA_{EFF}$  optics and

illumination wavelength of 405 nm to perform near-field recording. Minimum recorded mark size of 107 nm is measured in a phase-change disk of 160 nm track pitch. Although quite a large amount of laser noise is observed in detection, 50.4 Gbits/in<sup>2</sup> areal density and 50 MHz data rate are achieved.

As for aperture probes, researchers focus on enhancement of power transmission beyond the Bethe's prediction. The techniques of surface plasmon-enhanced transducer were developed. Ghaemi *et al.* [Ghaemi *et al.* 1998] at the NEC Research Institute observed transmission enhancement from a two dimensional-hole array in polycrystalline silver film of 200 nm thickness with the normal incident plane wave at wavelength 750 nm. The hole diameter is 150 nm, and period of the array is 900 nm. The observed transmission is 10 % which 1000 times stronger than Bethe would predict. The enhancement is interpreted from the interaction of the incident radiation with the surface plasmons. The transmission enhancement through a single hole is observed by Grupp *et al.* [Grupp *et al.* 1999] at the NEC Research Institute. The hole is surrounded by an array of dimples, which couple the incident radiation of wavelength 525 nm to the surface plasmon. The hole diameter is 150 nm with period of dimple array 500 nm. 0.02% transmission is achieved. An alternative single plasmon-enhanced hole structure was introduced by Thio *et al.* [Thio *et al.* 2001] at the NEC Research Institute. A single hole of 440 nm in a Ni film coated with Ag layer is surrounded by a set of concentric circular grooves of the 750 nm period. The peak transmission normalized to the hole area is observed to be 3 with the groove depth 90 nm at the wavelength 750 nm. Compared with the single hole surrounded by a dimple array of the period 750 nm, the transmission is

larger by a factor of 8. A research group in Japan also has reported significant work on the surface plasmon-enhanced transducer. Yatsui *et al.* [Yatsui *et al.* 2002] proposed and demonstrated extremely high throughput from a pyramidal silicon probe coated with a thin metal film. Light propagating inside the silicon core can be converted into surface plasmon at the metallic tip due to the high refractive index of the core and the thin metal film. Yatsui claimed 85 nm spot size and 2.3% power transmission were achieved.

Future directions of SIL and aperture probe technology are described in papers by Milster [Milster 2000, 2001]. SILs can be fabricated with higher index materials to further decrease the spot size, like GaP [Hirota *et al.* 2000]. However, GaP does not transmit into the blue. Alternative materials, like SrTiO<sub>3</sub> and cubic zirconium, may be good substitutes. The fast evanescent decay associated with-high index SILs forces gap height to be extremely small, say 25 nm or less. If this small gap can be maintained,  $NA_{EFF} \sim 2.5$  may be possible. Combination of this  $NA_{EFF}$  and blue laser of 400 nm wavelength could produce spot size of 160 nm, a data density of 90.7 Gbits/in<sup>2</sup>.

Aperture probes hold the record for spot size. However, their power throughput is not high enough to be manufactured into a commercial product. Combining other technique with aperture probes, like very small aperture lasers (VSALs) [Partovi *et al.* 1999] or combination apertures [Milster *et al.* 2001], is the direction for the enhancement of aperture probe efficiency.

## **CHAPTER 3**

### **THEORY AND DESIGN**

This chapter presents simple linear models that describe the advantage of combining a SIL with an aperture for data storage from the aspects of illumination and signal detection. In addition, design considerations of the APSIL and the metallic apertures + SIL are investigated.

#### **3.1 Introduction**

Conventional optical data storage systems require most of the light from a laser source to illuminate the recording layer of an optical disk, and they require most of the reflected light off the recording layers to be collected by the system. However, near-field transducers suffer from poor light throughput and have difficulty reading data in reflection. Bethe calculated the transmission of a sub-wavelength hole in a perfectly conducting plane. He predicted that the transmitted power falls as the fourth power of the hole radius with an incidental plane wave [Bethe 1944]. Due to its wide energy distribution, a plane wave is very inefficient as the illumination source for aperture systems, because most of the laser power is reflected back to the system or dissipated in the form of heat around the aperture. Thus, to increase efficiency of the laser power, use of a lens is desired to focus the laser beam as a compact energy distribution onto the aperture. This chapter presents formulas for relating the numerical aperture (NA) of the illumination lens to the throughput from a sub-wavelength aperture. These mathematical

formulae illustrate that the combination of a SIL and an aperture, with the use of an illumination lens, has advantage in throughput enhancement compared with other transducers.

Although the difficulty with signal detection in reflection for a near-field transducer is partially due to low throughput, a more fundamental limitation is the restricted collection of light energy inherent in transducer designs. To gain insight into optimal near-field transducer design for signal detection, the principle of how modulated data are detected is illustrated. Visualization of the detection effect is most easily observed in the angular spectrum of the reflected light. In a far-field system, like a conventional objective lens focusing on a data layer, the angular spectrum is essentially the reflected light in the plane of the objective lens. Each point in the plane corresponds to an angular component of the plane-wave spectrum that comprises the reflected spot at the recording layers. In a near-field system, the reflected energy that is collected by the system is interpreted with an angular spectrum approach. Through the angular spectrum, the advantage of combining an aperture with a SIL for signal detection is illustrated.

Design details for combination apertures are also provided in this chapter. To generate optimized spot size and transmitted power, the APSIL has certain design considerations on the wall angle and size of the dielectric probe, while the metallic aperture +SIL has the design considerations on the thickness of the metal screen and shape of the hole. A finite difference time domain (FDTD) simulation tool, providing a rigorous vector EM treatment, is used to investigate the power transmission of near-field transducers and the design considerations for combination apertures.

The general idea of FDTD algorithm is applying Finite Difference analysis to Maxwell's equations to obtain time history of electric and magnetic fields in a given structure [Taflove 1995]. Finite Difference analysis is to solve differential equations by replacing the derivatives terms with finite discrete terms. For example, the derivative of the electric field with respect to time is substituted by a fraction of the finite difference of electric field at two different positions over a finite time. Hence, in order to apply FDTD to a given structure, both temporal and spatial domains have to be discretized into infinitesimal cells for solving the Maxwell's equations with initial conditions and/or boundary conditions.

### 3.2 Illumination

The dependence of transmitted power on the NA of an illumination lens is calculated by treating a near-field transducer as a linear system. As shown in Figure 3-1,

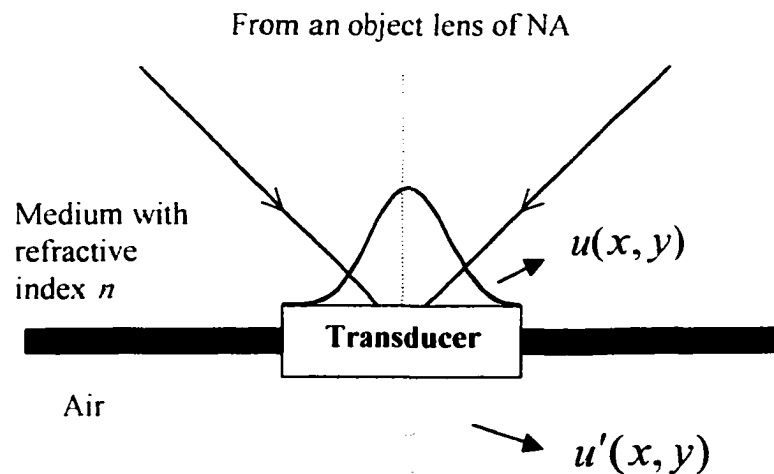


**Figure 3-1.** Schematic of a near-field transducer with an illumination objective lens.

a converging beam of wavelength  $\lambda$  from an objective lens illuminates a sub-wavelength transducer of a diameter  $d$ . The complex field distribution of the illumination on the aperture is  $u(x, y)$ , which can be expressed by

$$u(x, y) = \frac{n}{\lambda^2} \int A_0(\alpha, \beta) e^{-jkx(\alpha x + \beta y)} d\alpha d\beta, \quad (3-1)$$

where  $A_0(\alpha, \beta)$  is an angular spectrum of  $u(x, y)$ , and  $n$  is the refractive index of the medium where the incident light propagates. Note that  $A_0(\alpha, \beta)$  depends on the x- and y-direction cosines  $\alpha$  and  $\beta$ , respectively. The convenience of using  $\alpha$  and  $\beta$  as the variables of the angular spectrum is that they are equivalent to the  $NA$  of the illumination lens. From Equation (1-1),  $u(x, y)$  can be regarded as a linear superposition of unit amplitude plane wave components propagating with direction cosines  $\alpha$  and  $\beta$ . and weight  $A_0(\alpha, \beta)$ . The transducer is considered as a system that has a different response to each plane wave component. Figures 3-2 (a), (b) show FDTD simulation results of angular dependence of the transmitted irradiance distribution for TE and TM polarization, respectively. The transmitted irradiance distribution is from a 100 nm circular hole in an ideal metal. Figure 3-3 shows peak irradiance of each transmitted distribution in Figs. 3-2. Observing the FDTD simulation results, we conclude that an overall power factor changes with illumination angle, while the shape of the field distribution is not greatly affected by the illumination angle. Thus, the transmitted field is given by

$$u'(x, y) = \int u'_0(x, y) \varphi(\alpha, \beta) d\alpha d\beta, \quad (3-2)$$

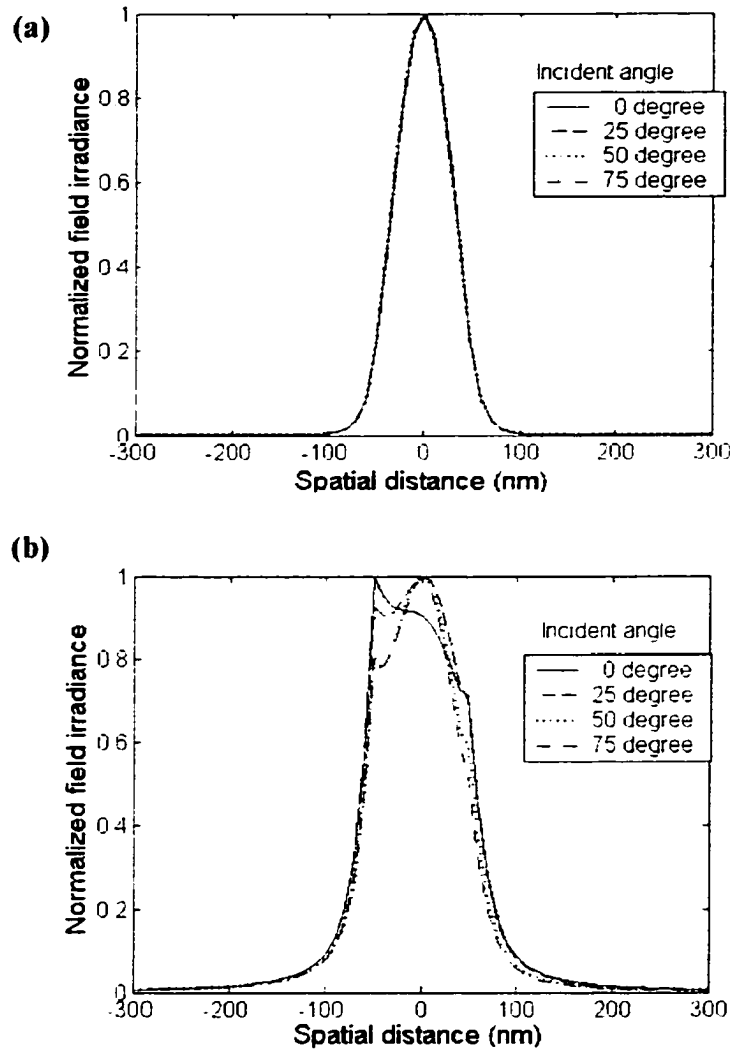


**Figure 3-2.** FDTD simulation results of angular dependence of the transmitted irradiance distribution for (a) TE and (b) TM polarization, respectively. The transmitted irradiance distribution is from a 100 nm circular hole in an ideal metal.

$$u'(x, y) = \int u'_0(x, y) \varphi(\alpha, \beta) d\alpha d\beta, \quad (3-2)$$

where  $u'_0(x, y)$  is the transmitted field distribution with a unit amplitude normal incidence plane wave and  $\varphi(\alpha, \beta)$  is an unitless weight factor that depends on the direction cosine  $(\alpha, \beta)$  of the illuminating plane wave. In fact,  $\varphi(\alpha, \beta)$  is given by

$$\varphi(\alpha, \beta) = \frac{n^2}{\lambda^2} K(\alpha, \beta) A_0(\alpha, \beta), \quad (3-3)$$

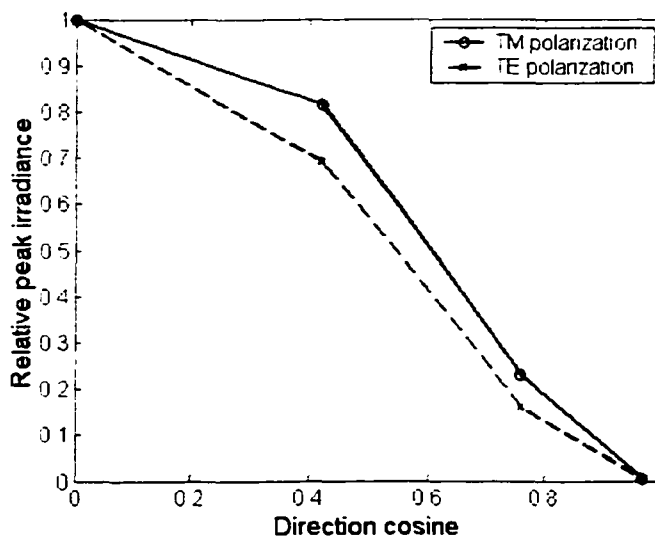


**Figure 3-3.** Peak irradiance of each transmitted distribution in Figs. 3-2.

where  $K(\alpha, \beta)$  is a unitless function that describes the change of transducer transmission versus angle, with  $K(0,0) = 1$ . Irradiance of the transmitted wave is obtained from

$$\begin{aligned} I'(x, y) &= \frac{1}{2} C n' \varepsilon_0 |u'(x, y)|^2 \\ &= \frac{n' \varepsilon_0 n^4 C}{2 \lambda^4} \left| \int u'_0(x, y) K(\alpha, \beta) A_0(\alpha, \beta) d\alpha d\beta \right|^2, \quad (3-4) \\ &= \frac{n' \varepsilon_0 n^4 C}{2 \lambda^4} |u'_0(x, y)|^2 \eta \left| \int A_0(\alpha, \beta) d\alpha d\beta \right|^2 \end{aligned}$$

where

$$\eta = \frac{\left| \int K(\alpha, \beta) A_0(\alpha, \beta) d\alpha d\beta \right|^2}{\left| \int A_0(\alpha, \beta) d\alpha d\beta \right|^2} \quad (3-5)$$

is an angular efficiency factor,  $C$  is the speed of light, and  $n'$  is the refractive index of the medium where the transmitted light propagates. According to the central ordinate theorem of Fourier transforms,

$$I(0,0) = \frac{\varepsilon_0 n^5 C'}{2 \lambda^4} \left| \int A_0(\alpha, \beta) d\alpha d\beta \right|^2 \quad (3-6)$$

It is found that

$$I'(x, y) = \frac{n'}{n} |u'_0(x, y)|^2 \eta I(0,0), \quad (3-7)$$

where  $I(0,0)$  is the central irradiance of the illumination on the aperture. Thus, the transmitted power is

$$\begin{aligned}
 P' &= \int I'(x, y) dx dy \\
 &= \eta \frac{n'}{n} I(0,0) \int |u'_0(x, y)|^2 dx dy
 \end{aligned} \tag{3-8}$$

When the transmitted field is approximately a disk with diameter  $d$ ,

$$P' \approx \eta \frac{n'}{n} I(0,0) |u'_0(0,0)|^2 \pi \left( \frac{d}{2} \right)^2 \tag{3-9}$$

For an illumination system that uses a Gaussian beam at the objective lens, such that the irradiance drops to  $1/e^2$  at the edge of the exit pupil, total power  $P$  in the illuminating beam is

$$\begin{aligned}
 P &= \frac{1}{2} \varepsilon_0 n c \iint |u(x, y)|^2 dx dy \\
 &= \frac{1}{2} \varepsilon_0 \frac{n^3}{\lambda^2} \iint |A_0(\alpha, \beta)|^2 d\alpha d\beta \\
 &= \frac{1}{\lambda^2} \int_0^{NA} \left| A_0(0,0) e^{-\left(\frac{\sigma}{NA}\right)^2} \right|^2 2\pi\alpha d\sigma \\
 &= \frac{\pi \varepsilon_0 n^3 NA^2}{4\lambda^2} |A_0(0,0)|^2 \left( \frac{e^2 - 1}{e^2} \right)
 \end{aligned} \tag{3-10}$$

In addition, Equation (3-6) is further expanded to

$$\begin{aligned}
I(0,0) &= \frac{\varepsilon_0 n^5}{2\lambda^4} \left| \int A_0(\alpha, \beta) d\alpha d\beta \right|^2 \\
&= \frac{\varepsilon_0 n^5}{2\lambda^4} |A_0(0,0)|^2 \left| \int_0^{NA} e^{-\left(\frac{\sigma}{NA}\right)^2} 2\pi\sigma d\sigma \right|^2 \\
&= \frac{\pi^2 \varepsilon_0 n^5}{2\lambda^4} |A_0(0,0)|^2 \left( \frac{e-1}{e} \right)^2 NA^4
\end{aligned} \tag{3-11}$$

By substitution of Eq. (3-11) into Eq. (3-9), power transmission  $T$  of the aperture is

$$\begin{aligned}
T &= \frac{P'}{P} \\
&= 2\pi^2 \frac{n'n}{\lambda^2} \left( \frac{e-1}{e+1} \right) \eta |u'_0(0,0)|^2 \left( \frac{d}{2} \right)^2 NA^2
\end{aligned} \tag{3-12}$$

Equation (3-12) does not give an explicit expression to relate  $T$  and  $NA$ , because the angular efficiency factor  $\eta$  also depends on  $NA$ . In Eq. (3-5), the angular factor of the field transmittance  $K(\alpha, \beta)$  in the integral of the numerator is important to determine the dependence of  $\eta$  on  $NA$ .  $K(\alpha, \beta)$  varies with the design of an transducer, which includes geometry, material characteristics and other factors.

The square of transmitted field  $|u'_0(0,0) \cdot K(\alpha, \beta)|^2$  for unit amplitude plane wave illumination versus incidence angle through a circular hole in perfect conducting screen is investigated with the Bethe prediction and FDTD simulation results. Figure 3-4 is a summary of the comparison. The dashed lines stand for Bethe prediction that is obtained from Reference [Bethe 1944] with 488 nm wavelength and a 100 nm in diameter aperture. The solid lines stand for the results of FDTD simulation that are obtained with

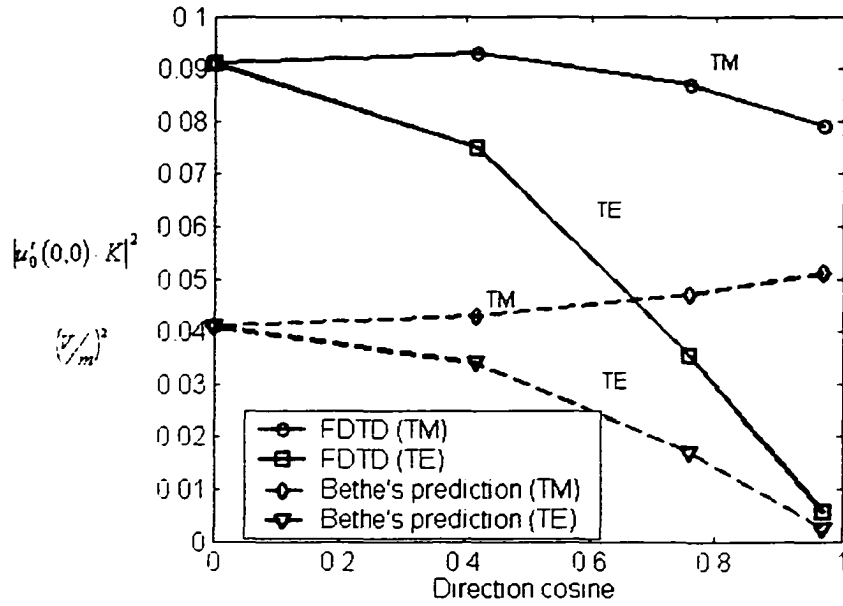


**Figure 3-4.** Comparison between FDTD and Bethe's prediction on the square of transmitted field  $|u'_0(0,0) \cdot K(\alpha, \beta)|^2$  for unit amplitude plane wave illumination versus incidence angle through a circular hole in perfect conducting screen

the illumination setting shown in Fig.3-5. A small current source is used to illuminate the aperture with incident angles  $\theta_m = 0^\circ, 25^\circ, 50^\circ, 75^\circ$ . TE polarization exhibits an oscillating electric field in the y direction. TM polarization exhibits electric field oscillation in the x direction. The observation plane is located 20 nm below the aperture.

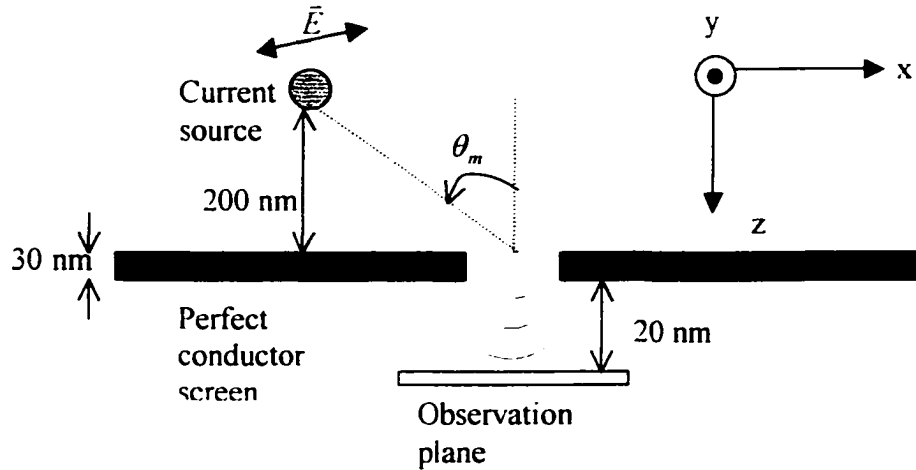


**Figure 3-5.** Illumination setting used in the FDTD simulation.

Both methods show similar trend. Both TM curves are steady, but both TE curves decline rapidly. On the other hand, due to the difference that the Bethe method uses a plane wave and FDTD uses a current source, the curves of the FDTD simulation are offset 0.05 from those of the Bethe prediction. With the exception of an offset, FDTD simulation predicts basic electromagnetic field behavior, and thus FDTD simulation is adapted in our forthcoming investigation.

Five transducers listed in Table 3-1 are investigated in terms of  $u'_0(0,0)$  and  $K(\alpha, \beta)$  by FDTD simulations. Table 3-2 are the results of  $|u'_0(0,0)|^2$  for the transducers in Table 3-1. We found that the Al aperture + SIL has the smallest value of  $|u'_0(0,0)|^2$  while the other transducers have similar value of  $|u'_0(0,0)|^2$ .

**Table 3-1.** Geometries of transducers investigated by FDTD simulations

	PEC* aperture	Al aperture	APSIL probe	Al aperture + SIL	Plasmon_enhanced holes [Ghaemi <i>et al.</i> 1998]
Wavelength	488 nm	488 nm	488 nm	488 nm	750 nm
Geometry	Circular hole 200 nm in diameter	Circular hole 200 nm in diameter	Wall angle 9° Height 400 nm Size 200 nm	Circular hole 200 nm in diameter	150nm hole array
$n$	1	1	1.843	1.843	1

Note: \* Perfect Electric Conductor (PEC)

**Table 3-2.** The results of  $|u'_0(0,0)|^2$  for the transducers in Table 3-1.

	PEC aperture	Al aperture	APSIL probe	Al aperture + SIL	Plasmon_enhanced holes [Ghaemi <i>et al.</i> 1998]
$ u'_0(0,0) ^2$ (V/m) <sup>2</sup>	2.3	2.1	2.1	1.4	2

Figures 3-6 (a), (b) are the results from the FDTD simulation for the angular dependence of  $|K|^2$  for TE and TM polarization, respectively. For TE polarization, the

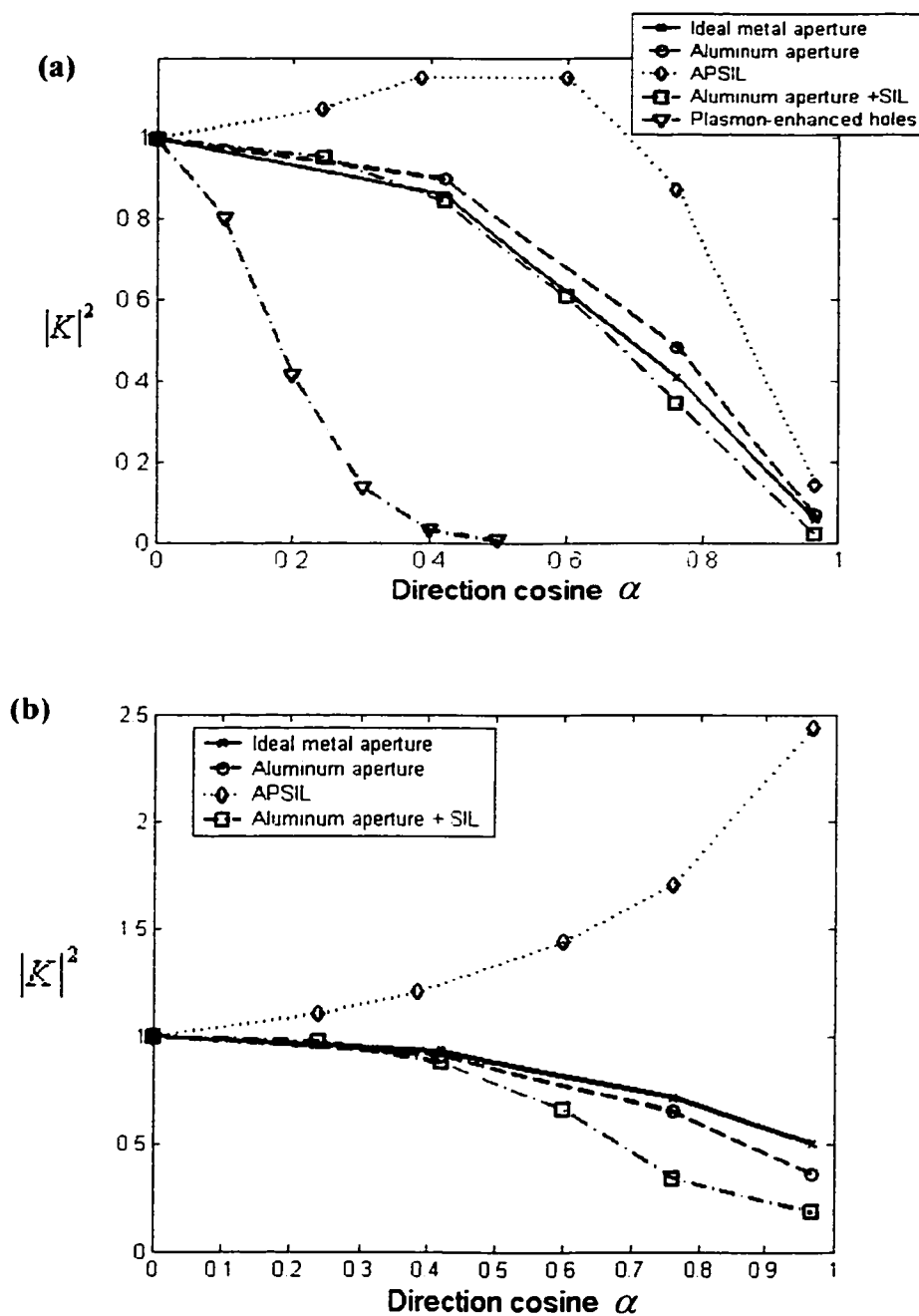


**Figure 3-6.** Profiles of  $K(\alpha)$  for several transducers using (a) TE (b) TM polarized illumination. Geometries are described in Table 3-1.

curves of PEC aperture, Al aperture, and Al aperture + SIL follow the same quadratic trend. The curve of plasmon-enhanced holes decline as a gaussian curve with  $1/e^2$  width of 0.3. The curve of APSIL rises up from zero direction cosine  $\alpha$  and drops at 0.6 direction cosine  $\alpha$ , which behaves like a super-gaussian curve with  $1/e^{10}$  width of 0.85. For TM polarization, the curves of PEC aperture, Al aperture, and Al aperture + SIL all tend to fall off immediately from the zero direction cosine. The curve of APSIL tends to rise up from  $\alpha = 0$ . For both TE plot and TM plot, the APSIL is apparently much less sensitive to illumination angle in comparison with other transducers. In the TM plot, the plasmon-enhanced holes are most sensitive to the illumination angle. These results warrant further use of fitted functions of the curves in the TE plot to model the effect of K factors on the power transmission of the transducer. The simple function for the PEC aperture, Al aperture, and Al aperture + SIL curves is

$$K_{TE}(\alpha) = (1 - \alpha^2)^2 \quad (3-13)$$

The simple function for the APSIL curve is

$$K_{TE}(\alpha) = e^{-\left(\frac{\alpha}{0.85}\right)^{10}} \quad (3-14)$$

The simple-fitted function for the plasmon-enhanced holes curve is

$$K_{TE}(\alpha) = e^{-\left(\frac{\alpha}{0.3}\right)^2} \quad (3-15)$$

Equations 3-13, 3-14 and 3-15 are substituted into Equation 3-5 for  $\eta$  of each transducer. The  $\eta$  just obtained and the parameters in Table 3-1 and Table 3-2 are then substituted into Equation 3-12 to yield Figure 3-7, which shows the relationship between the power transmission of each transducer and  $NA$  of the illumination lens. Figure 3-6 clearly shows that the plasmon-enhanced holes have the worst transmission among all the transducers due to its narrow range of angular selectivity, as shown in Figure 3-5 (a). The transmission of the SIL + Al aperture is only slightly better than that of Al aperture alone because of the larger refractive index from the SIL and smaller value of  $|\mu'_0(0,0)|^2$ . APSIL has superior transmission because of the advantage of broad range angular selectivity and

high refractive index from the SIL. Figure 3-7 shows ~50 % transmission can be achieved with a 0.5 NA illumination lens. Even better performance of APSIL than that in Figure 3-7 is expected, if the K factor of the TM polarization can be incorporated to  $\eta$  in Eq. 3-5.

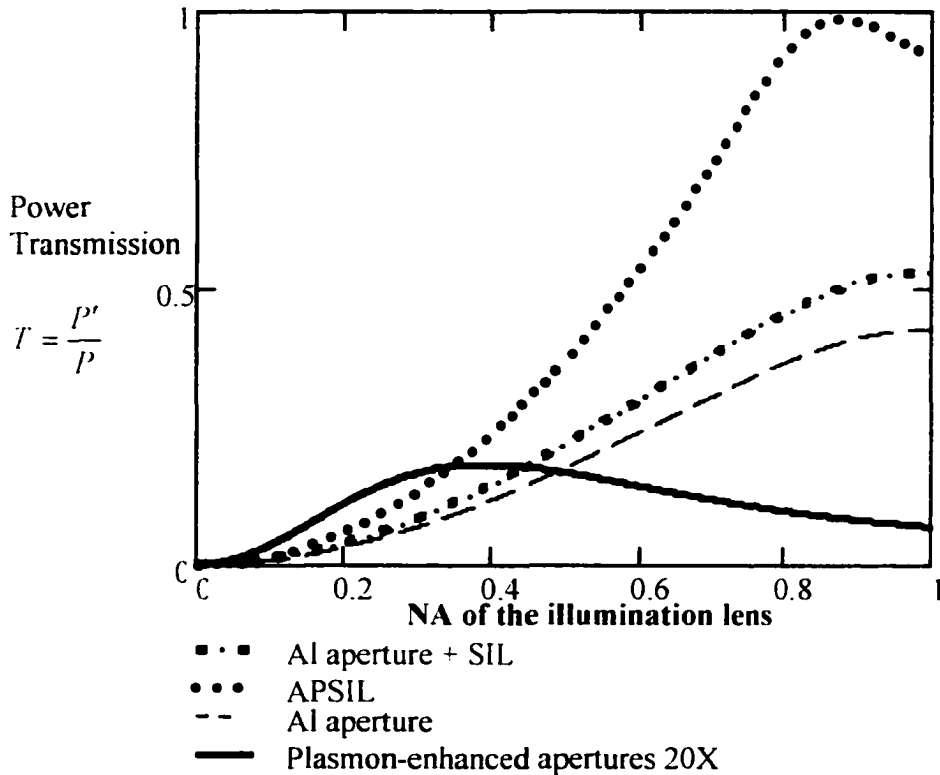


**Figure 3-7.** Displays of the power transmission versus illumination NA for the geometries listed in Table 3-1.

### 3.3 Signal Detection

Reference [Milster *et al.* 2001] reviews the detection process in terms of a simple scalar model to illustrate the fundamental benefit of combining an aperture with a SIL.

Specifically, the detection process of a DVD system is used as an example, as shown in Figure 3-8. A profile of the focused spot  $h(x,y)$  exhibits a spot size  $s$ . The angular-spectrum representation  $H(\alpha, \beta)$  of the focused spot is found by the Fourier transform of  $h(x,y)$ . Coordinates of  $H$  are the direction cosines  $\alpha, \beta$  corresponding to the  $x, y$ -axes, respectively.  $H(\alpha, \beta)$  is a representation of the light pattern in the exit pupil. The limits of  $H(\alpha, \beta)$  correspond to the  $NA$  of the system.

Figure 3-8 shows the interaction of the mark pattern  $m(x,y)$  and spot  $h(x,y)$  as a

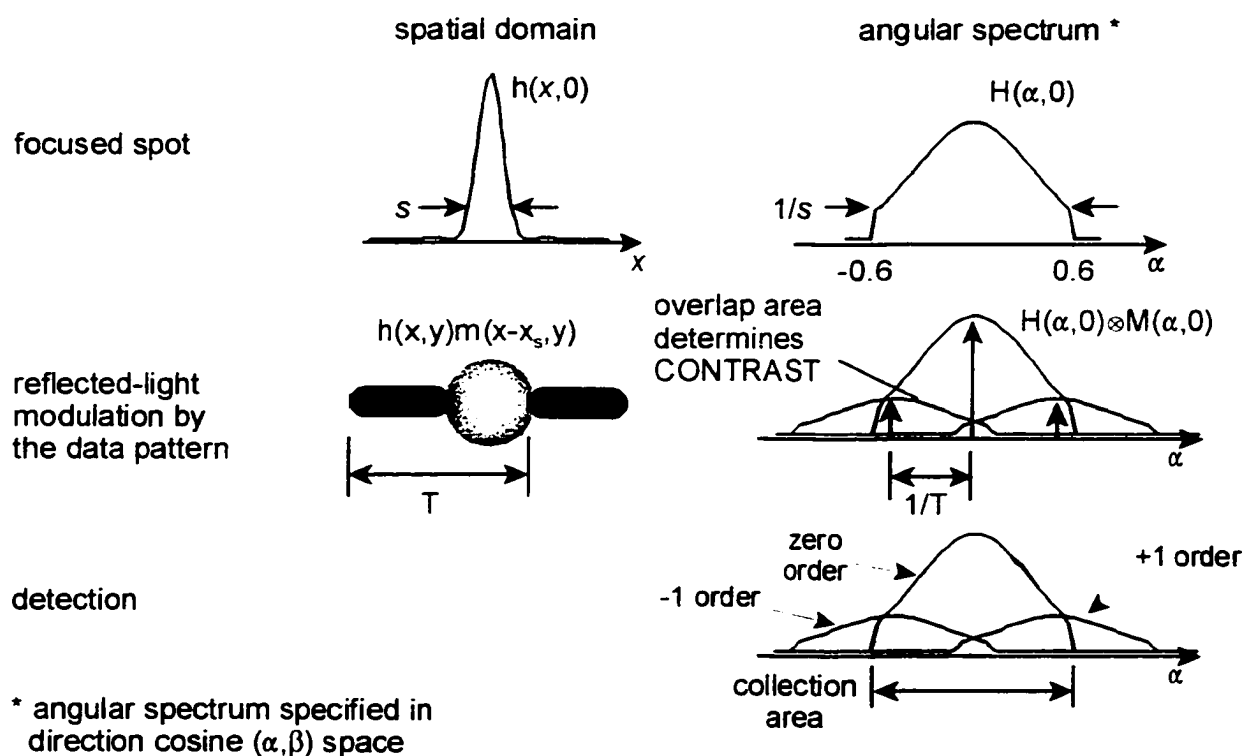


**Figure 3-8.** The basic process of detection is shown for a DVD system. In angular (frequency) space, the overlap of the diffracted orders determines the signal contrast

simple multiplication. The reflected-light angular spectrum contains overlapping orders of diffraction. As the mark pattern  $m(x-x_s, y)$  moves under the focused spot with displacement  $x_s$ , the phase of the  $\pm$  orders change relative to the phase of the zero order. The resulting changes in the interference pattern produce modulation in the overlap areas. The size of the stop and the size of the detector determine the range of the collection area in which the modulation is detected. In DVD optical data storage systems, the collection area is equal to the width of the zero diffraction order.

Now we consider a SIL system. The angular spectrum for a SIL with  $NA = 0.6$ ,  $n = 2$  and  $NA_{EFF} = 1.2$  is shown in Figure 3-9 (a). The direction cosine axes are multiplied by  $n$ , because the light spot focuses inside the SIL material. Notice that the diffracted orders are spread far in direction cosine space, because the mark period  $T$  is only  $\lambda/2$ . In this case, there is little overlap and low contrast. However, the collection area for the detector gathers all the modulation.

Figure 3-9 (b) shows the angular spectrum for an aperture system where the hole diameter is  $\lambda/4$  and  $T = \lambda/2$ . In this case, there is more overlap than Fig. 3(a). However, the amount of modulation passing through to the collection area is only a small percentage of the total modulation. Therefore, contrast is low, and detection is difficult.

Figure 3-9 (b) illustrates a common problem with all aperture-probe systems. That is, the collection area is smaller than the angular range of the modulation. For example, a fiber-optic illumination system with a small hole in the end of the fiber will produce a modulation over a wide angular range, but the collection area is limited due to the  $NA$  of

the fiber. Therefore, when the fiber is used to collect the reflected light, much of the modulation is lost. The high angular-frequency information simply does not propagate down the fiber to the detector. As a simple rule-of-thumb guide, the percent of overlap in the collection area should be at least 20% for reliable data recovery.

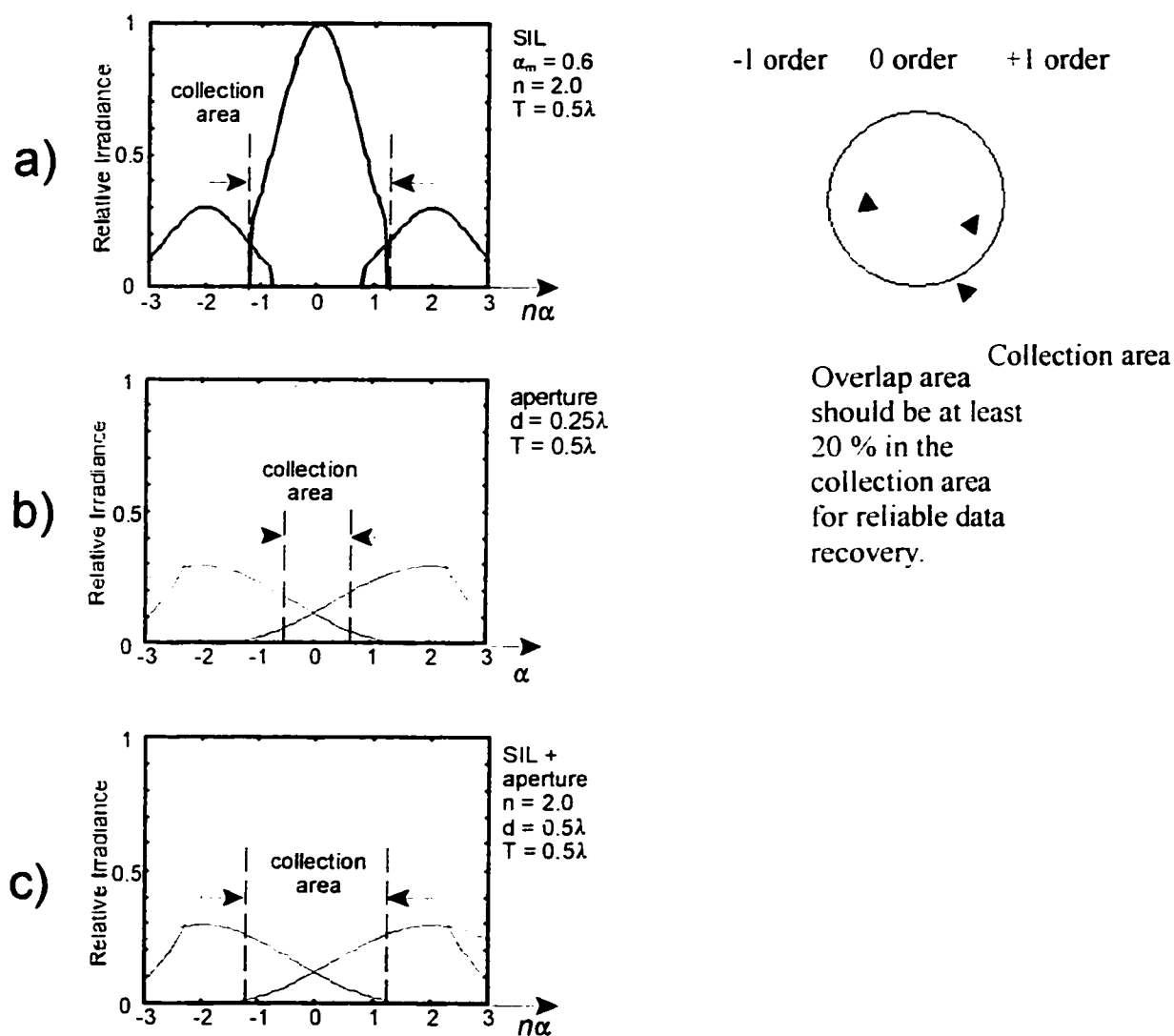


**Figure 3-9.** Angular spectra of several detection geometries. (a) SIL only; (b) aperture only; (c) aperture + SIL. Notice that the combination of an aperture and a SIL produces the most overlap area and highest contrast.

Figure 3-9 (c) shows the angular spectrum of the combination SIL-aperture system. Figure 3-9 (c) is similar to Figure 3-9 (b), except the collection area is much larger. Therefore, higher contrast and signal-to-noise ratio is achieved with the combination probe. A fundamental advantage of the SIL in combination with the aperture probe is that the contrast of the signal is greatly improved over using the aperture alone.

### 3.4 The Design of Combination Apertures

In Sections 3.2, 3.3, it is found that the best two choices of the near-field transducers in terms of efficiency and signal detection are the APSIL and the SIL + Al aperture. Design considerations of these two transducers are investigated in this section.

#### 3.4.1 APSIL

Figure 1-3 (a) shows that the basic geometry of the APSIL is a tapered conical probe attached to the bottom of a SIL. As shown in Figure 1-3 (a), the probe height  $h$ , wall angle  $\theta$ , and probe size  $d_1$  are important parameters in the design of this transducer. Reference [Hirota 2000] provides design considerations of the APSIL probe. First,  $h$  is just longer than evanescent decay length associated with the marginal ray angle in the SIL. Second,  $\theta$  allows the incident light to be well confined in the probe by internal reflections. Third,  $d_1$  is significant smaller than spot size achievable by the SIL.

In this section, FDTD is used to obtain spot profiles at various incident angles to further investigate the optimal wall angle of the probe. The same illumination setting in

Fig. 3-5 and APSIL probe listed in Table 3-1 ( $h = 400$  nm,  $\theta = 9^\circ$ ,  $d_i = 200$  nm) are used in FDTD simulation. The results of individual normalized spot profiles for TE and TM polarization given in Figs. 3-10 (a) and (b), respectively when incident angle

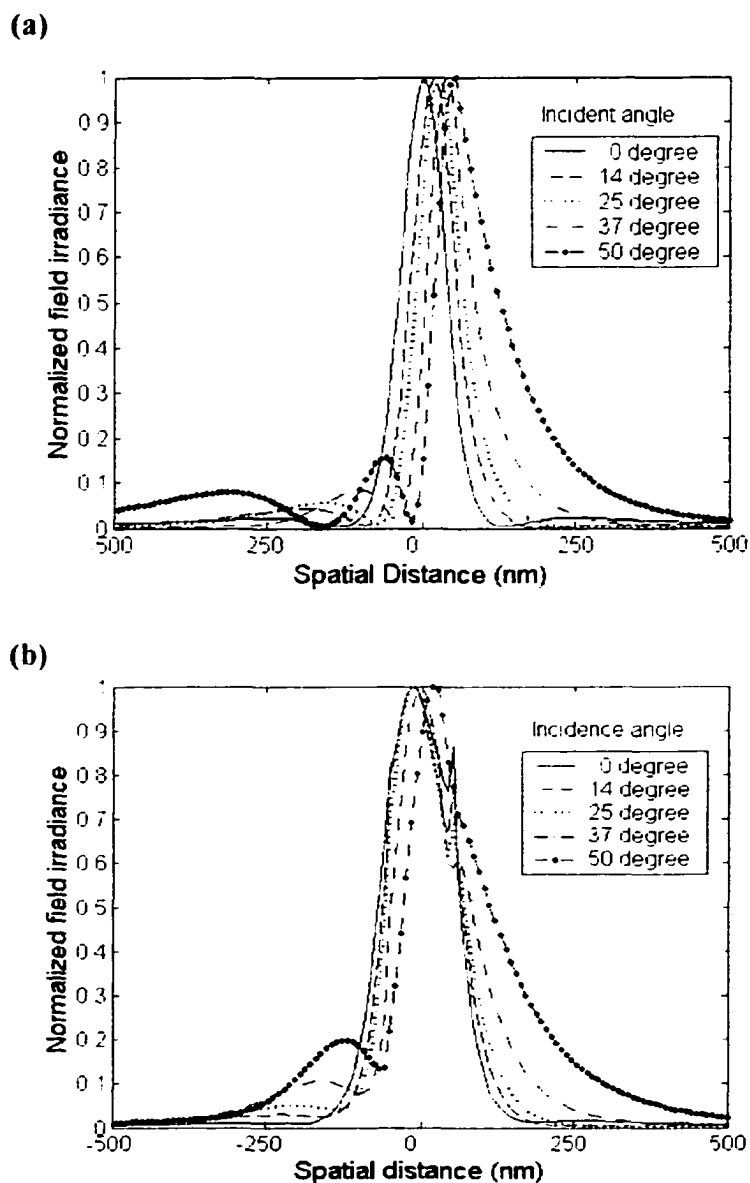


**Figure 3-10.** FDTD simulation results of individual normalized spot profiles from the APSIL in Table I for (a) TE and (b) TM polarization when the incident angle  $\theta_m = 0^\circ, 12^\circ, 25^\circ, 37^\circ$ , and  $50^\circ$ .

$\theta_m = 0^\circ, 12^\circ, 25^\circ, 37^\circ$ , and  $50^\circ$ . The TE plot shows the peak irradiance shifts as the incident angle of the illumination increases. In addition, the shape of spot profile starts to spread out at an incident angle of  $37^\circ$ . The TM plot shows that peak irradiance shifts only at large incident angle and the shape of spot profile, similar to that in TE plot, starts to spread out at an incident angle of  $37^\circ$ . The observed behavior of spot profile in Figs. 3-10 (a) and (b) implies that  $37^\circ$  is a critical incident angle for maximizing performance of the APSIL system with respect to spot size. In other words, the maximum  $NA$  of the illumination for this APSIL geometry is 0.6, based on spot size. With this result, the optimal wall angle  $\theta$  is investigated for the spot profile with an incident angle of  $37^\circ$ . Figures 3-11 (a) and (b) show individually normalized spot profiles from  $\theta = 5^\circ, 9^\circ, 14^\circ, 20^\circ, 26^\circ$  for TE and TM polarization, respectively, when the incident angle is  $37^\circ$ . In both TE plots and TM plots, the spot profile shows increased improvement, in terms of suppressed side lobes, as the wall angle increases to  $\theta = 20^\circ$ .

Although the wall angle of  $20^\circ$  yields the best spot performance at  $37^\circ$  incidence angle, the optimal wall angle at  $0^\circ$  incidence angle is also determined. Figures 3-12 (a) and (b) show spot profiles from different wall angles for TE and TM polarization, respectively, at an incident angle of  $0^\circ$ . Both plots show the maximum peak irradiance is generated with the wall angle at  $14^\circ$ . However, the spot profile from the wall angle at  $14^\circ$  in the TE plot has a side lobe. Thus, the wall angle of  $9^\circ$ , which generates the second largest peak irradiance without a side lobe, is preferred for spot performance. Combining spot performance in previous paragraph and spot performance in this paragraph, a trade-

off is observed for choosing the optimal wall angle of the APSIL system. However, the  $9^\circ$  wall angle is chosen as a reasonable wall angle for the APSIL with the low  $NA$  illumination.

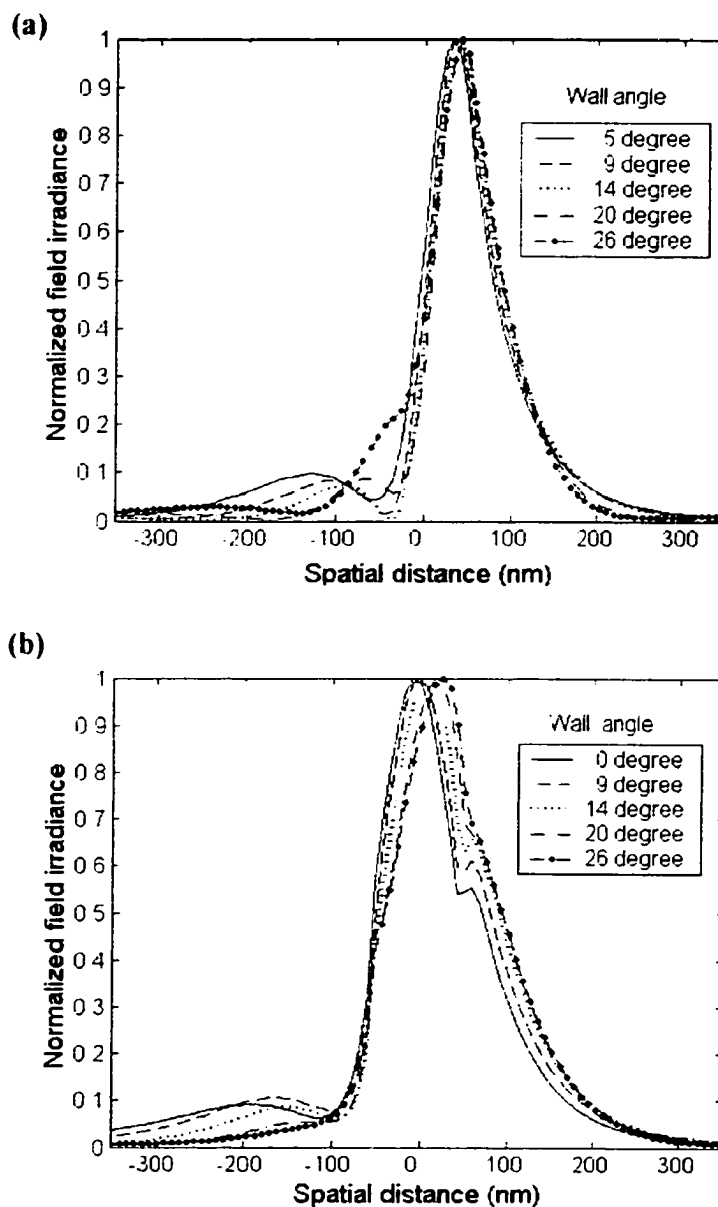


**Figure 3-11.** FDTD simulation results of individual normalized spot profiles in air for (a) TE and (b) TM illumination at incident angle  $\theta_m = 37^\circ$  when the wall angle  $\theta = 0^\circ, 9^\circ, 14^\circ, 20^\circ$ , and  $26^\circ$ .

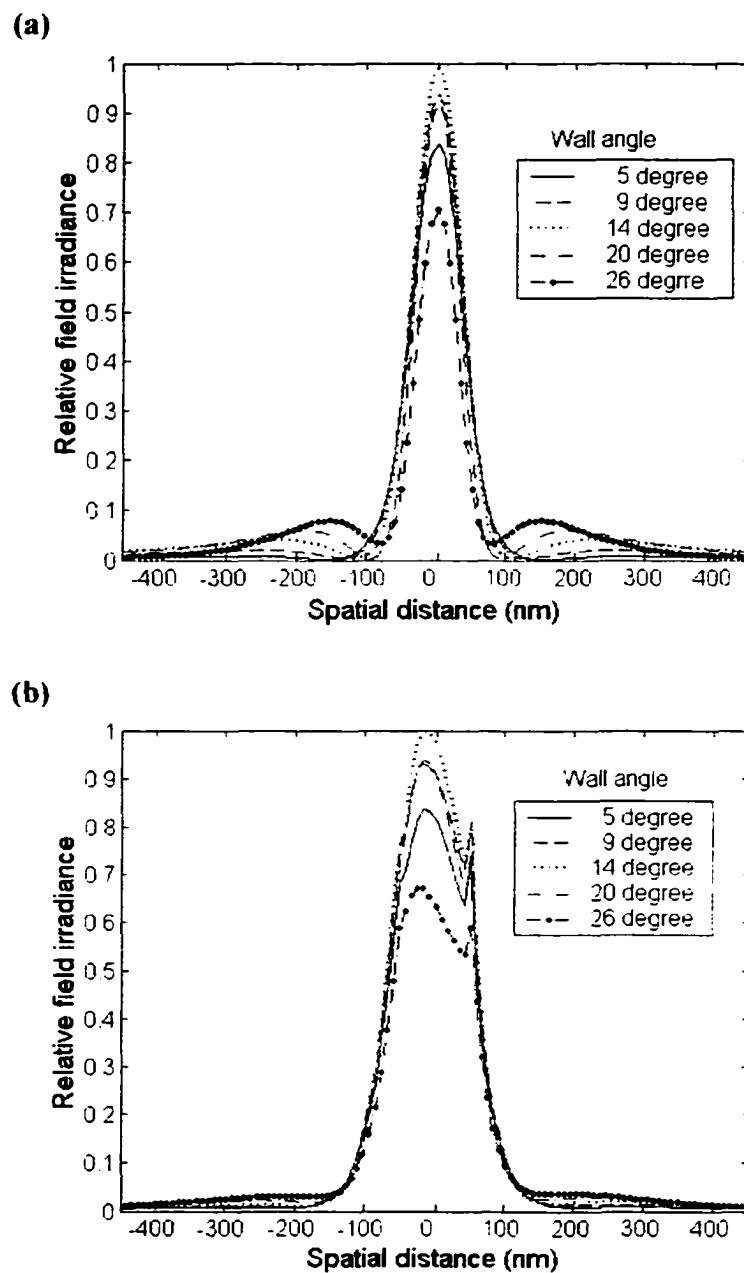


**Figure 3-12.** FDTD simulation results of spot profiles in air for (a) TE and (b) TM illumination at incident angle  $\theta_{in}=0^\circ$  when the wall angle  $\theta=0^\circ, 9^\circ, 14^\circ, 20^\circ$ , and  $26^\circ$ .

The optimal probe size  $d_1$  is investigated with a wall angle of  $9^\circ$ . Figures 3-13

(a) and (b) show spot profiles with  $d_1 = 100$  nm, 200 nm and 300 nm for TE and TM

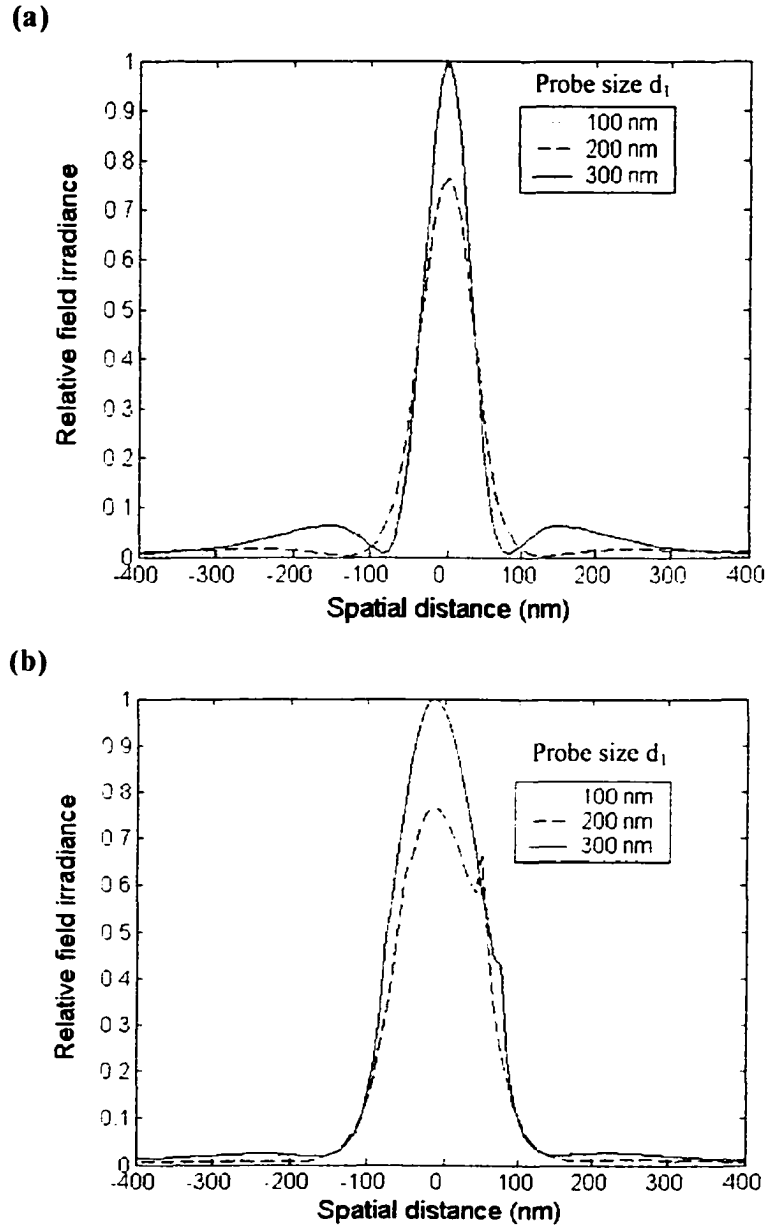


**Figure 3-13.** FDTD simulation results of spot profiles in air for (a) TE and (b) TM illumination at incident angle  $\theta_m = 0^\circ$  when the wall angle  $\theta = 9^\circ$  and probe size  $d_1 = 100$  nm, 200 nm, and 300 nm.

polarizations, respectively. In both plots,  $d_1 = 300$  nm produces maximum peak irradiance, but side lobes in the spot profile in TE plots are observed. Therefore, probe size of 200nm, which generates the second largest peak irradiance without side lobes, is the optimal choice for the APSIL system. For the probe height,  $h = 400$  nm is chosen for the  $37^\circ$  marginal ray angle in the SIL according to the calculation of  $1/e^2$  evanescent decay distance in Reference [Milster 2001].

### 3.4.2 Al aperture + SIL

The geometry of Al aperture + SIL is simply a hole of size  $d_2$  in an aluminum screen attached to the bottom of SIL. The thickness of the aluminum screen  $t$  in Fig. 1-4 (b) and the shape of the hole are two important considerations for design of this transducer. Following the same strategy used in the APSIL design, we obtain spot profiles at various incident angles and investigate optimal thickness of the aluminum. Figures 3-14 (a) and (b) give FDTD simulation results of individually normalized spot profiles for TE and TM polarization from the Al aperture + SIL system used in Section 3.2 ( $t = 30$  nm, circular hole with  $d_2 = 200$  nm). Both TE and TM plots show side lobes in the profiles when the incident angle of illumination is increased to  $50^\circ$ . At an incident angle of  $50^\circ$ , effects of aluminum thickness are investigated. Figures 3-15 (a) and (b) show individually normalized spot profiles from  $t = 30$  nm and 100 nm for TE and TM polarizations, respectively, when the incident angle is  $50^\circ$ . In both TE plots and TM

plots, the spot profile shows improvement in terms of a suppressed side lobes when aluminum thickness is 100 nm.

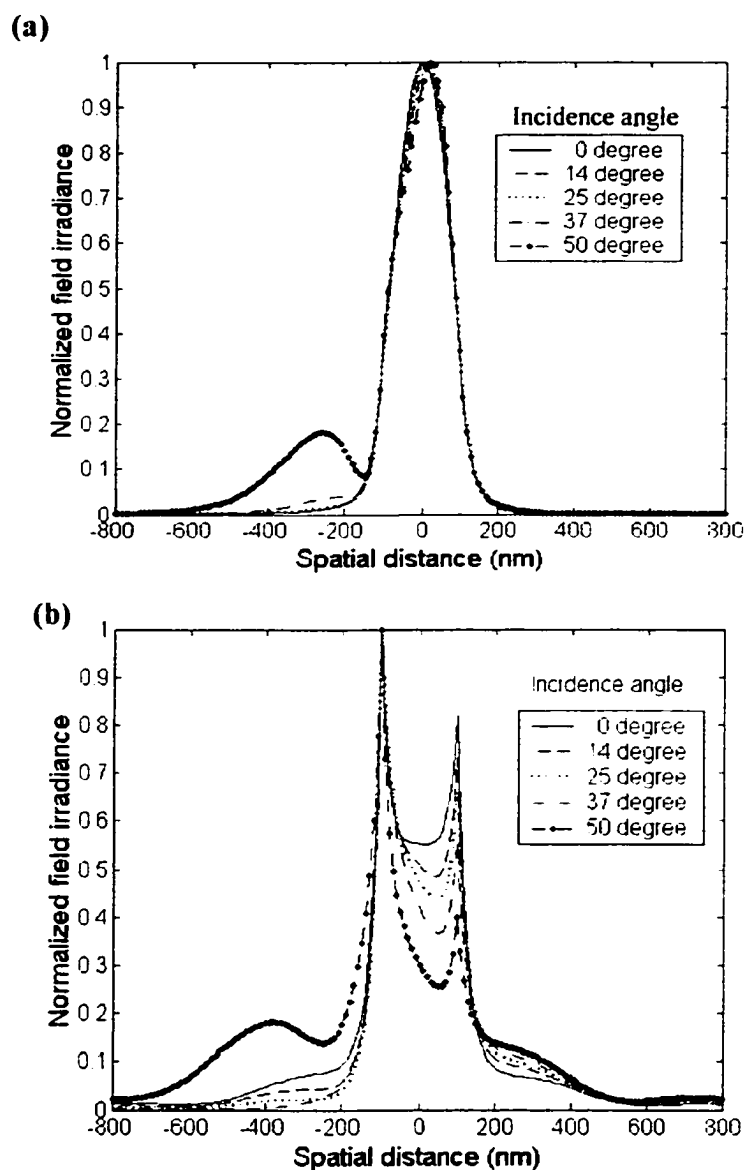


**Figure 3-14.** FDTD simulation results of individual normalized spot profiles from the AL aperture + SIL in Table I for (a) TE and (b) TM polarization when the incident angle  $\theta_m = 0^\circ, 12^\circ, 25^\circ, 37^\circ, \text{ and } 50^\circ$ .

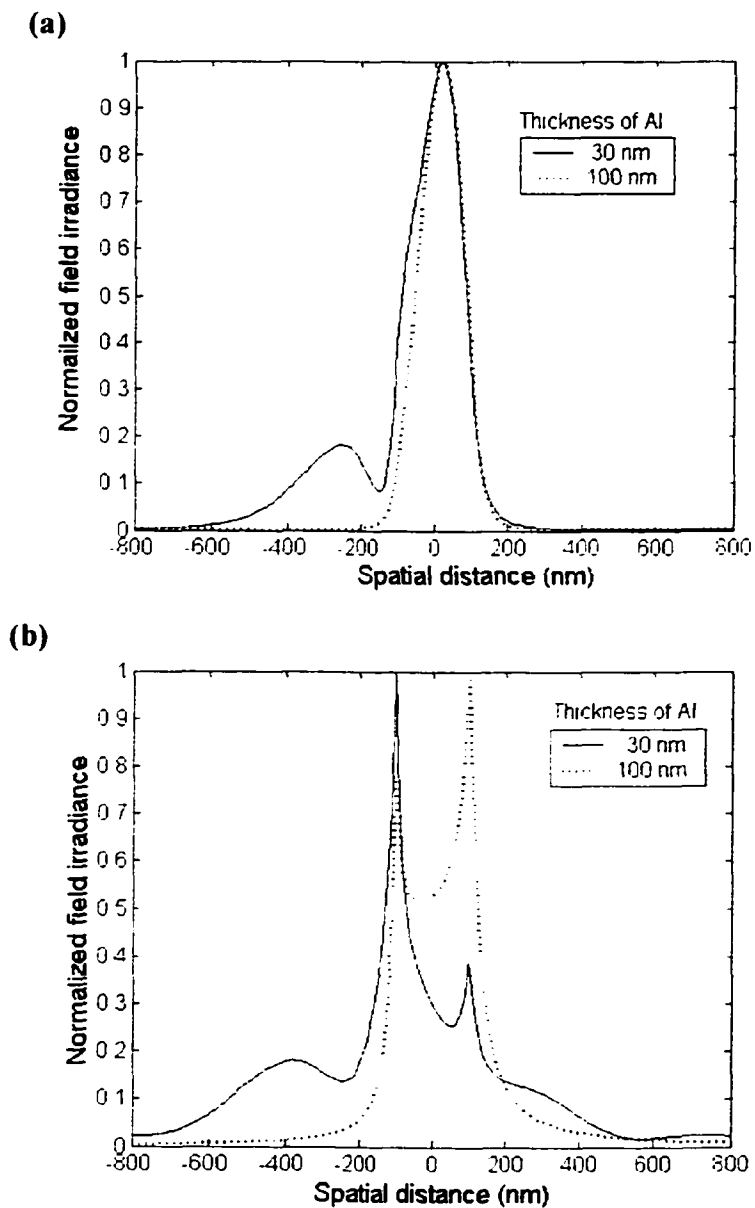


**Figure 3-15.** FDTD simulation results of individual normalized spot profiles in air for (a) TE and (b) TM illumination at incident angle  $\theta_m = 37^\circ$  when the thickness of Al  $t = 30$  nm and 100 nm.

The effect of the aluminum thickness for normal incidence is also investigated.

Figures 3-16 (a) and (b) show spot profiles from  $t = 30$  nm and 100 nm for TE

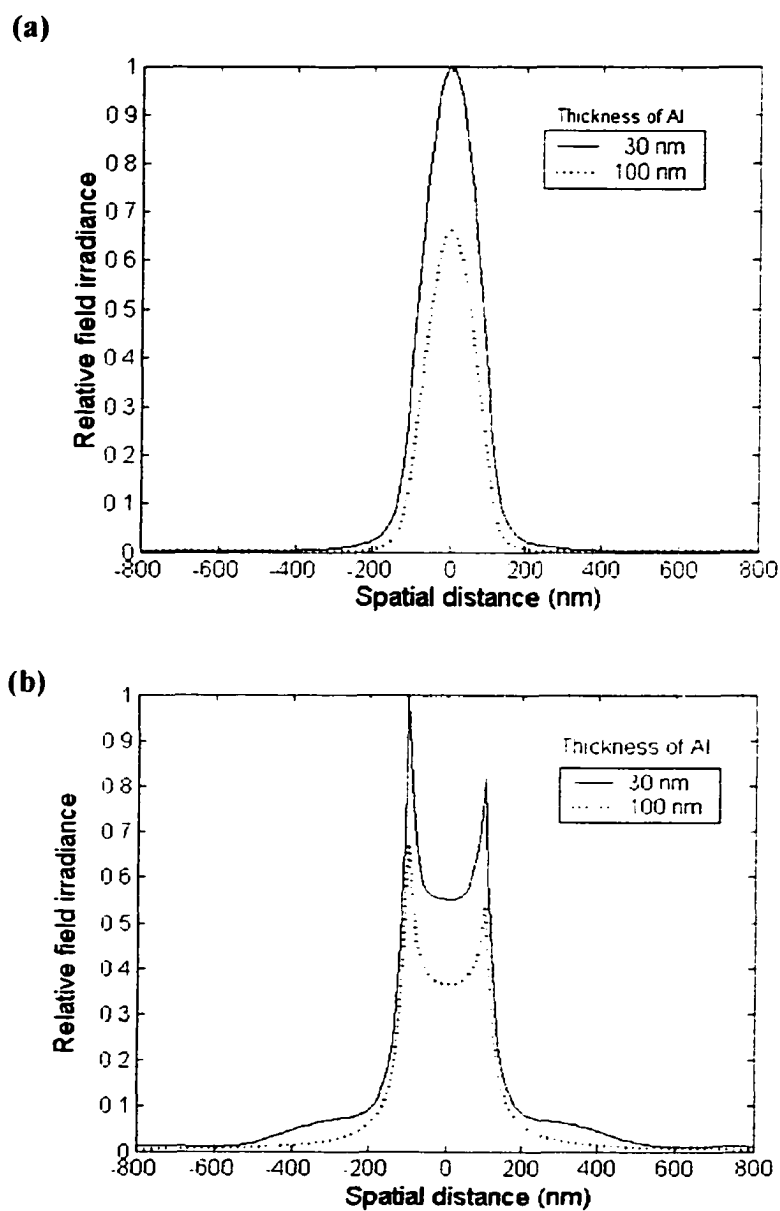


**Figure 3-16.** FDTD simulation results of spot profiles in air for (a) TE and (b) TM illumination at incident angle  $\theta_m = 0^\circ$  when the thickness of Al  $t = 30$  nm and 100 nm.

and TM polarizations, respectively, with the incident angle at  $0^\circ$ . In both plots, larger peak irradiance is found from the aluminum thickness of 30 nm, while smaller spot size is found from the thickness of 100 nm. Combining performance in previous paragraph and that of the performance in this paragraph, 100 nm is chosen as optimal aluminum thickness for generating smaller spot size.

Reference [Milster *et al.* 2001] provides a detailed investigation on the shapes of holes on a 100 nm thick aluminum screen. Four shapes are considered, as shown in Fig. 3-17. The smallest shape, Aperture A, is a circular hole approximately  $\lambda/4n$  in diameter. Aperture B is about  $\lambda/3n$  in diameter. Aperture C is a rectangular hole that is  $\lambda/4n \times \lambda/3n$ , and Aperture D is a rectangular hole that is  $\lambda/3n \times \lambda/2n$ . The rectangles are aligned with the short side in the direction of the primary incident polarization. Aperture D is found to be the best aperture, which exhibits both high throughput and small spot size. Table 3-3 lists the detailed simulation results for Apertures A, B, C, and D when  $\lambda = 650$  nm and  $n = 1.9$ . Light distributions are analyzed on observation planes in air at 30 nm and 100 nm past the bottom of the apertures.

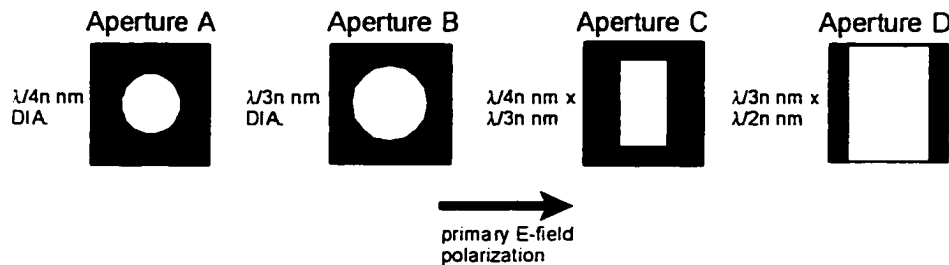


**Figure 3-17.** Aperture geometry used in the FDTD simulation.

**Table 3-3.** Detailed results from FDTD study on Al aperture + SIL

Aperture	Peak irradiance		TM profile FW $1/e^2$ (nm)		TE profile FW $1/e^2$ (nm)	
	Plane 1	Plane 2	Plane 1	Plane 2	Plane 1	Plane 2
140 nm dia. (A)	0.05	0.02	455	630	385	455
210 nm dia. (B)	0.27	0.1	280	560	245	315
140 x 210 nm <sup>2</sup> (C)	0.10	0.04	280	455	175	385
210 x 280 nm <sup>2</sup> (D)	0.31	0.12	210	280	245	315

### 3.5 Summary

Near-field transducers are investigated with respect to power transmission with a linear model. A transducer is treated as a linear system, whose transmitted power has a dependence on the incident angle of the illumination. Shape of the transmitted field distribution does not. FDTD simulation results show the APSIL has a great range of angular selectivity for illumination in both TE and TM polarizations. With the advantages of large angular selectivity and high refractive index provided by SIL, the APSIL exhibits superior performance in power transmission. As for the Al aperture + SIL, the angular selectivity and field transmittance from a normally incident plane wave are not better than the Al aperture alone, thus only slightly better performance than an Al aperture is

obtained. The transducer of plasmon-enhanced holes has very poor transmission due to its narrow range of the angular selectivity.

The detection process is reviewed in terms of a scalar model. The angular spectrum is used to visualize how modulated data are detected. Compared with those of a SIL or aperture system independently, the angular spectrum of a combination aperture shows both large overlap area between diffracted orders and large data collection area. Thus, higher contrast and signal-to-noise ratio is achieved with the combination aperture.

The design of the APSIL and Al aperture + SIL is investigated by FDTD simulation. For APSIL, probe height 400 nm, probe size 200 nm, and wall angle  $90^\circ$  are chosen due to good spot profile for normally incident light of 488 nm wavelength. The smaller probe size than 200 nm cannot reduce the spot size. The maximum  $NA$  of the illumination for the optimal geometry is 0.6. For Al aperture + SIL, the result shows the best geometry in our investigation is an aluminum thickness of 100 nm and a  $\lambda/3n \times \lambda/2n$  rectangular hole.

## **CHAPTER 4**

### **FABRICATION AND TEST OF COMBINATION APERTURES**

This chapter presents fabrication procedures and test results of the APSIL and the metallic aperture + SIL. The spot size and optical efficiency from the APSIL system are evaluated.

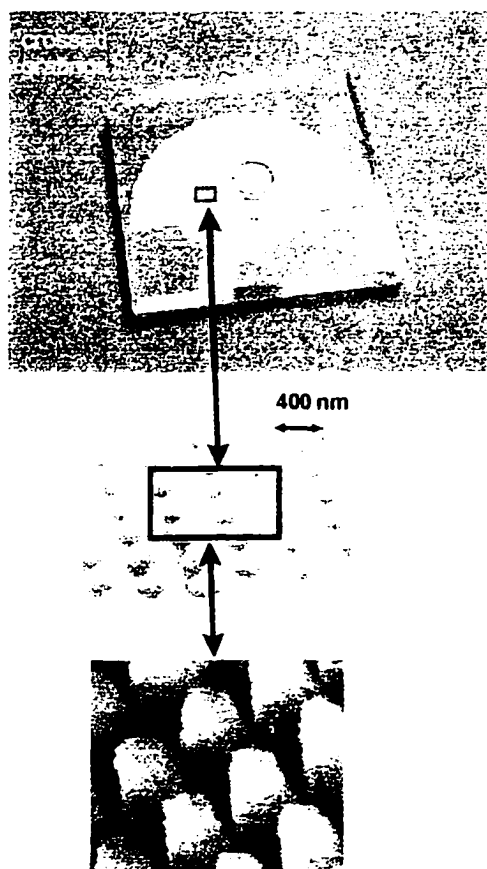
#### **4.1 Introduction**

In Chapter 3 it is demonstrated that combination apertures, APSILs and Al aperture + SIL, have advantages with respect to power transmission and signal detection efficiency. Especially, the APSIL system shows superior performance in power transmission among all the investigated transducers. Results support the idea that combination apertures have the potential to exhibit both good resolution and optical efficiency for data storage applications.

Although the idea of the combination apertures is good, techniques to fabricate the probe tip or hole on the bottom of the SIL need to be developed. In this chapter, two fabrication methods are introduced to show how APSIL and Al aperture + SIL transducers are fabricated for the illumination wavelength of 488 nm. In addition, APSIL and SIL + Al apertures are tested to evaluate spot size and optical efficiency compared to a SIL only and far field systems. Pupil modulation images are also captured to show characteristics of signal detection.

## 4.2 Fabrication of an APSIL

Fabrication of dielectric probe tips is illustrated in Fig. 4-1. First, the SIL made of LaSFN9 glass ( $n=1.843$ ) is placed in a precision hole cut in a carrier glass and glued in place. The flat side of the SIL is flush with the carrier. Next, the carrier/SIL



- 1) Mount SIL in carrier
- 2) Coat with photoresist
- 3) Expose photoresist to cross-grating pattern
- 4) Develop photoresist
- 5) Ion mill

**Figure 4-1.** Fabrication process for dielectric aperture probes (APSIL) combined with a SIL.

combination is coated with photoresist and exposed holographically with a crossed grating pattern. The period of the grating is adjustable. In the first experiment, a 400 nm pitch grating is exposed in each dimension. The exposed resist is developed, which leaves a regular array of bumps on the surface of the SIL. Next, an ion mill etches the glass to form the array of conically shaped tips. By controlling the etching rate, the dimension of the probe tip is 320 nm at the entrance, 200 nm at the bottom, and 400 nm between the entrance and exit planes. Although there is an array of probe tips on the bottom of the SIL, only one of them is used at a time during testing. The advantage of using an array of probes is for the purpose of reducing the alignment difficulty

### **4.3 APSIL Experiment**

In order to test the APSIL, a NEar-Field MicroScope (NEFUS) is constructed, which is composed of a laser optics system, a commercial microscope (Olympus IX 70), and high-accuracy positioning devices. A detailed schematic of the experimental setup is shown in Fig. 4-2. A collimated laser beam of 488 nm wavelength propagates through a polarizing beam splitter, relay lens, and quarter wave plate. The beam is then focused into the APSIL by an objective lens of 0.5 NA. The APSIL is mounted on a thin metal plate that can be positioned by a picomotor with a resolution of 20 nm per step. Spacing between the probe and the recording medium is controlled to  $\sim 40$  nm by fine movement of the picometer along the z direction, as well as indication from a strain gauge attached on a flexure of the APSIL mount. High precision spot/aperture alignment is achieved by fine movement of the picomotor along x and y directions. A microscope slide holds the

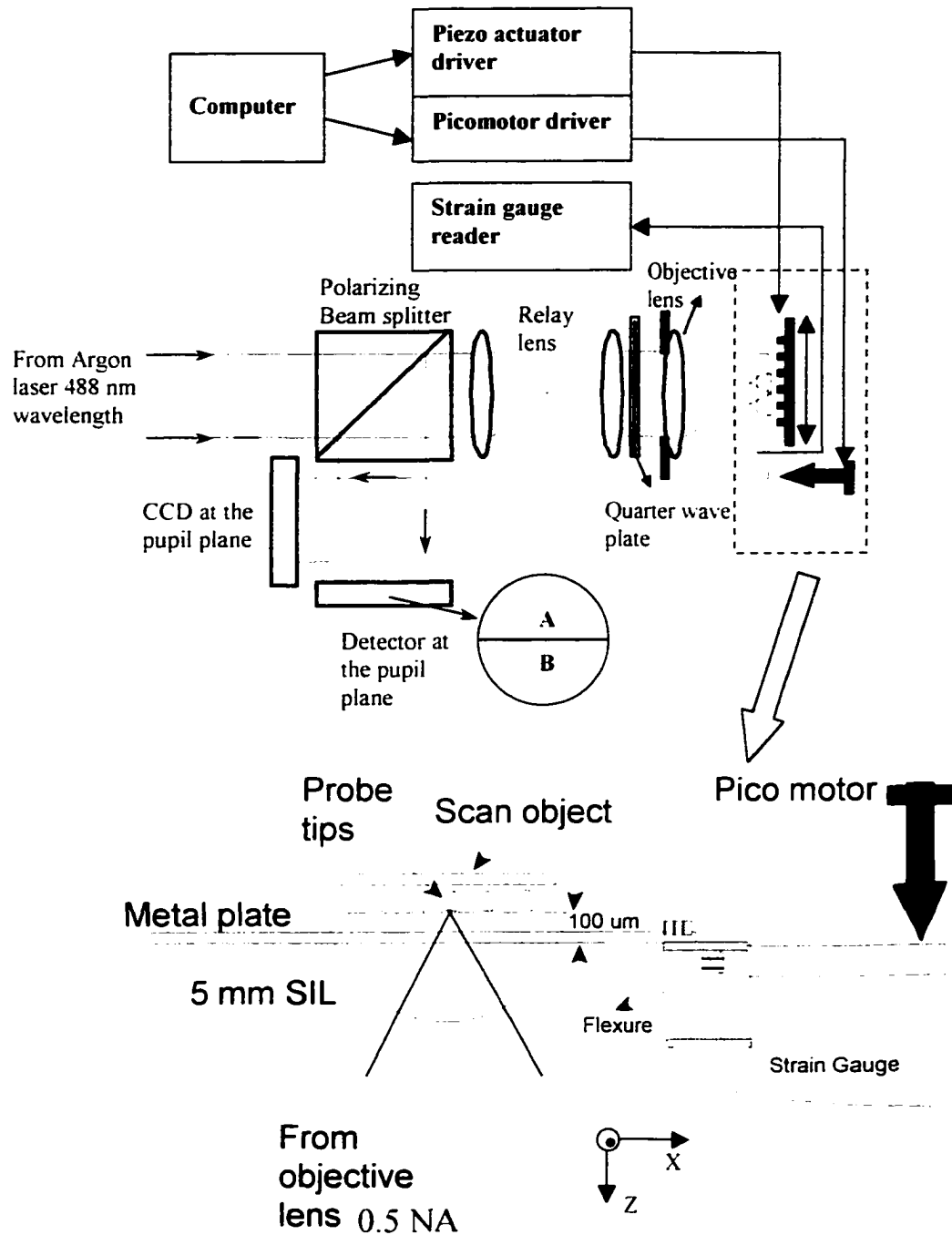


**Figure 4-2.** Detailed composite schematic of the NEFUS.

scan object and is translated along x or y directions by a piezo actuator. The small light spot formed by the probe tip scans across features on the moving object. The slide speed is 12 mm/sec, which is slow enough to neglect air disturbance between the probe and medium. The reflected light is collected by the objective lens and directed into the CCD and the detector at the pupil plane conjugate to the stop by action of the relay lens. Use of the polarizing beam splitter and the quarter wave plate can eliminate most of the reflected light that propagates toward the detector. The detector has two segments (A and B), which can provide electrical sum and difference voltages from the light levels detected on A and B.

To evaluate the spot size and optical efficiency from the APSIL, an edge-scan experiment is adopted using a phase grating with a  $1.6 \mu\text{m}$  period as a scan object. Two aspects of the read-out experiment results are studied. One is the pupil modulation pattern captured by the CCD. The other is readout signal generated by the detector. When the grating translates, the pupil modulation patterns for the far field system ( $NA = 0.5$ ), SIL system ( $NA_{EFF} = 0.95$ ) and the APSIL ( $NA_{EFF} = 2.4$ ) system are shown in Figs. 4-3 (a), (b), (c), respectively. In Figs.4-3 (a) and (b), the pupils show a typical overlap pattern due to diffraction from the  $0^{\text{th}}$  and  $\pm 1^{\text{st}}$  orders of grating. The  $0^{\text{th}}$  diffracted order fills the pupil entirely while the  $\pm 1^{\text{st}}$  diffracted orders appear as sections of circles displaced on opposite sides of the  $0^{\text{th}}$  order. Modulation in the pupil occurs where the  $\pm 1^{\text{st}}$  orders overlap the  $0^{\text{th}}$  order. Comparing Fig. 4-3 (a) with Fig. 4-3(b), the SIL system has larger overlap on the pupil and provides stronger modulation than the far field system does. In Fig. 4-3 (c), a unique pupil modulation pattern from the APSIL system is shown.

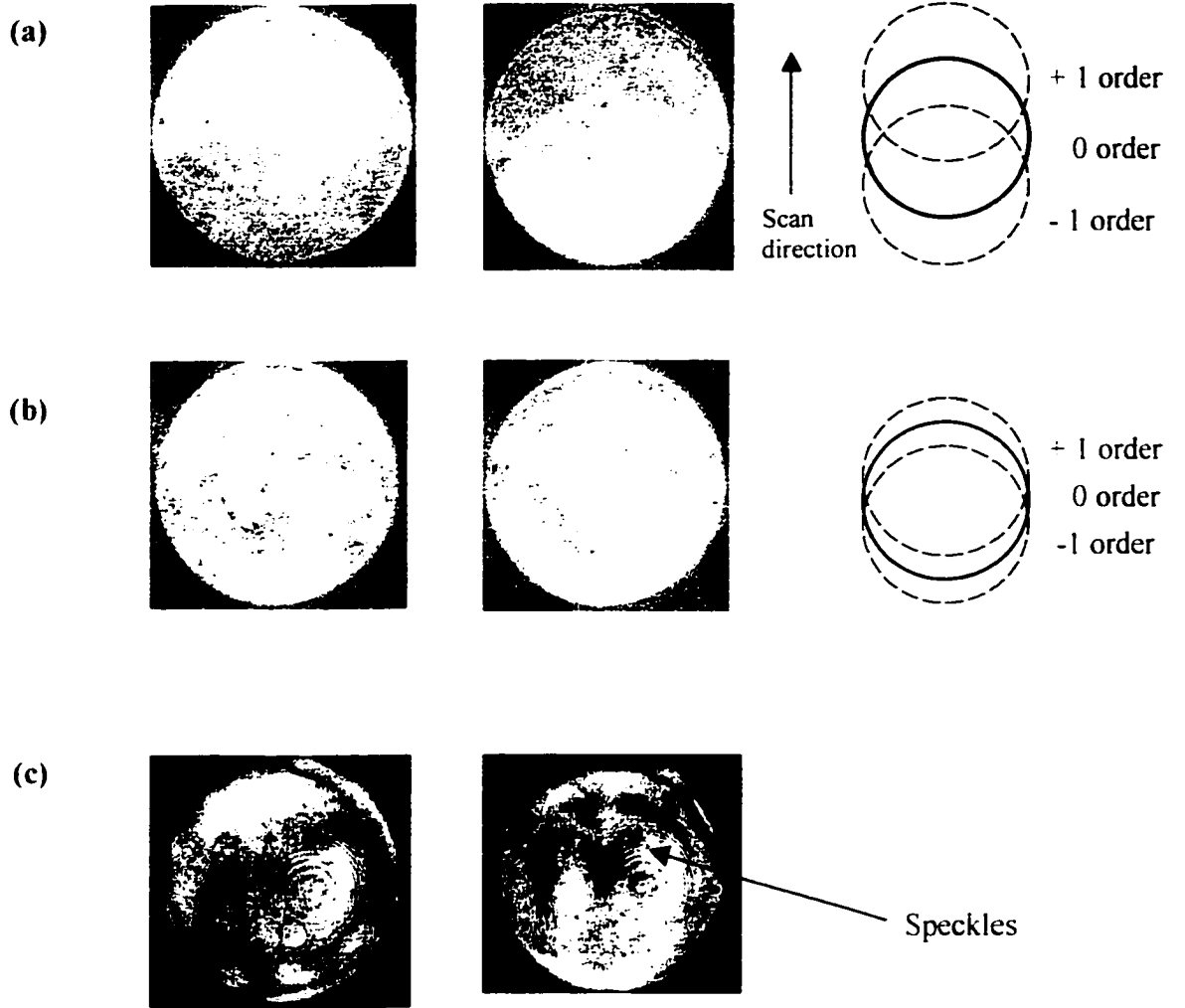


**Figure 4-3.** Two distinct pupil images from the (a) far field system (NA = 0.5) (b) SIL system (NA = 0.95) (c) APSIL system (NA = 2.4) when the grating translates.

Compared with Figure 4-3 (a), 4-3 (b), the boundary of  $\pm 1^{\text{st}}$  order is less clear, because the spatial limits imposed by the aperture produce a wider angular spectrum in the pupil, as described in Reference [Milster 2001]. Therefore, a larger area of modulation is observed, and higher contrast results. However, the experimental pupil patterns shown in Figure 4-3 (c) are more complicated than can be predicted by simple theory. The speckles observed on the pupil might result from the light scattering off the probe tips on the bottom of the SIL.

The readout signals from the difference A-B when scanning an edge are shown in Figure 4-4, which includes output from the far field, SIL and the APSIL systems. The APSIL system gives the best improvement in readout performance, because the signal has the sharpest rise when scanning over the edge of the grating. The  $\text{FW}1/e^2$  spot size for the APSIL system is  $\sim 200$  nm and is found by estimating the scan distance between the 5% height and 95% height of the signal. The 200 nm spot size agrees well with the aperture size of 200 nm. In addition, since the vertical signal produced by the APSIL is in 2x scale, the signal loss from the system is only 50% in reflection. Figure 4-5 gives the readout signals from the sum A+B when a large mark written on a phase-change medium is used as a scan object. It shows  $\sim 300$  nm  $\text{FW}1/e^2$  spot size and 50 % efficiency in reflection from the APSIL system. The 300 nm spot size is larger than that obtained from the phase grating because the scan was taken over a groove, where the air gap is 100-200 nm.

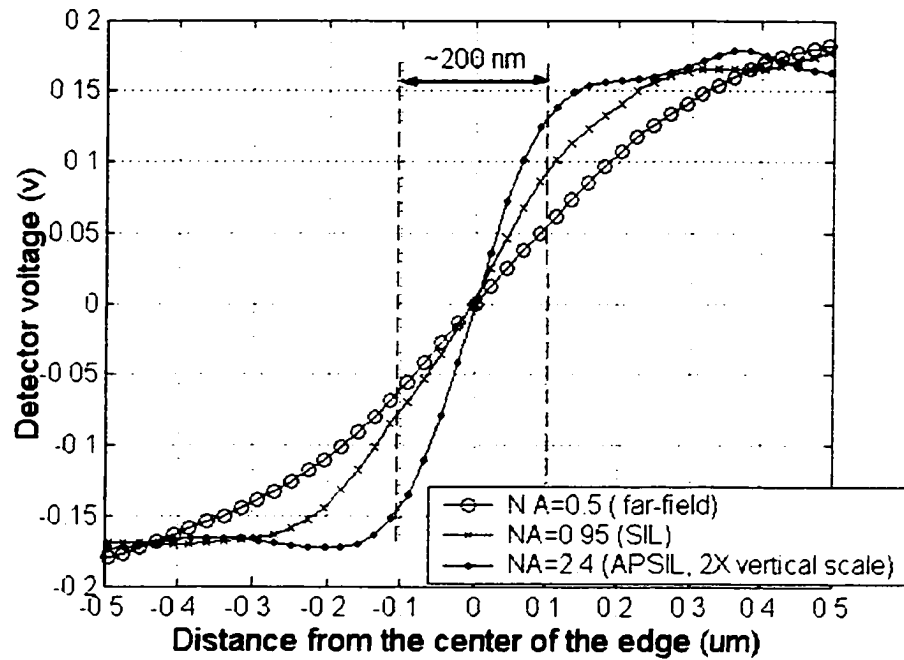


**Figure 4-4.** The readout signals from the systems of far field, SIL and APSIL when scanning the groove edge in a phase grating of  $1.6 \mu\text{m}$  pitch.

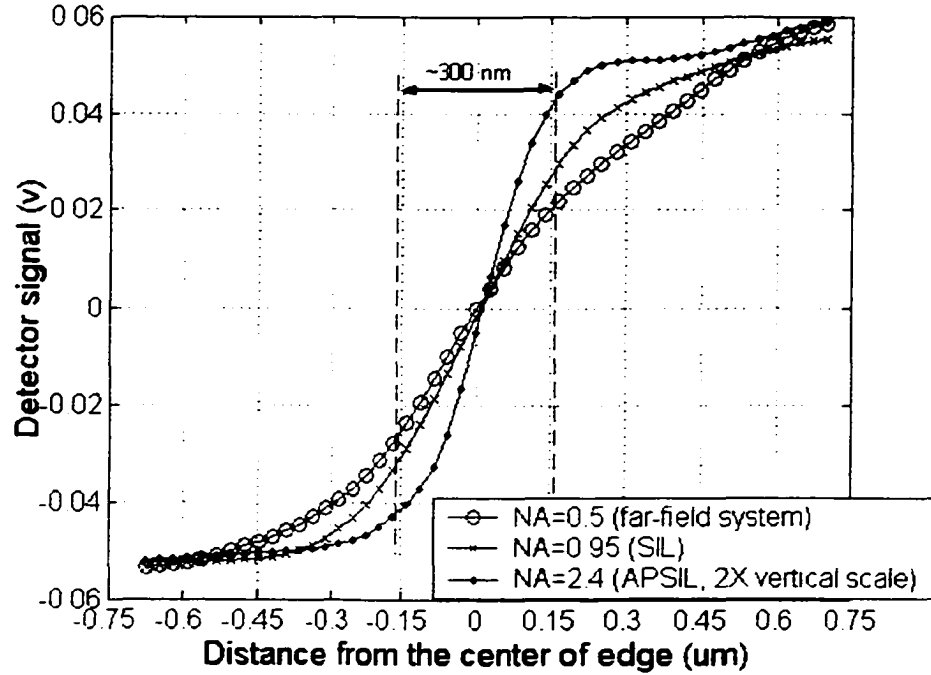


**Figure 4-5.** The readout signals from the systems of far field, SIL and APSIL when scanning a big mark on the phase-change medium.

#### 4.4 Fabrication of Al aperture + SIL

The fabrication process for our metallic apertures is shown in Figure 4-6. First, a  $2\ \mu\text{m}$  thick SiN membrane is fabricated [Akaisi 1998]. Next, 100 nm of Al is deposited on the membrane. A  $5\times 5$  array of small rectangular holes of  $200\ \text{nm} \times 350\ \text{nm}$  are then cut into the Al by a focus ion beam (FIB) at Carnegie-Mellon University [Chen and Schlesinger]. Finally, the SIL is attached to the backside of the membrane. The SIL is then detached from the membrane and mounted on a mechanical carrier for experiments.

A partial image of the array along with a close view of one aperture is shown in Fig. 4-7. The rectangular shape is well preserved, except for a small elongation on one side. Also shown in Fig. 4-8 is a picture of the combination SIL-aperture probe with the aperture array illuminated with a laser beam.

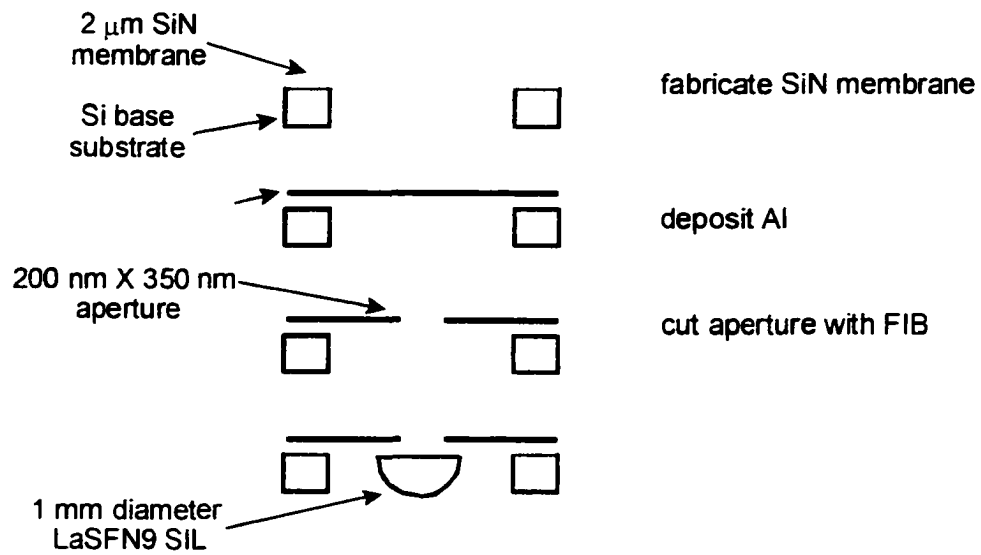


**Figure 4-6.** Fabrication process for Al aperture array combined with SIL.

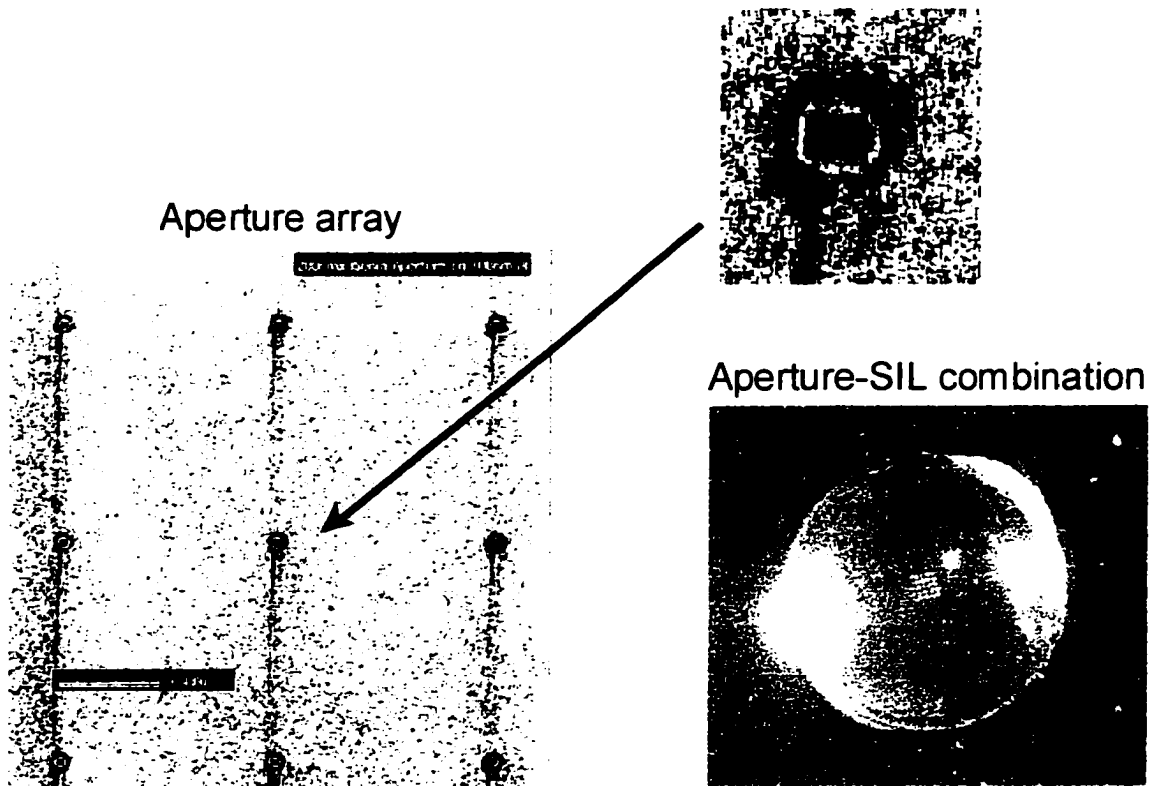


**Figure 4-7.** Image of the FIB-fabricated aperture array and a closeup of one aperture. The size of each aperture is approximately 200 nm x 350 nm. The completed Al aperture + SIL is also shown with the array illuminated with a laser beam.

#### 4.5 Al aperture + SIL Experiment

Al aperture + SIL aperture is also tested by NEFUS with the same phase grating used in the APSIL system. A large background reflection from the Al layer is observed on the pupil image. When the grating translates, no modulation pattern can be found due to strong background light. Thus, no modulated signal can be generated from the

detector. The objective lens of 0.8 NA is also used in NEFUS for Al aperture + SIL. The detected signal doesn't show any improvement. To verify that apertures are correctly fabricated, a Wyko NT-2000 interferometer is used. If asperities in the form of bumps or protrusions are found, the lack of the signal could be attributed to the asperities. The result shown in Fig. 4-8 indicates no asperities observed on the back of the SIL.

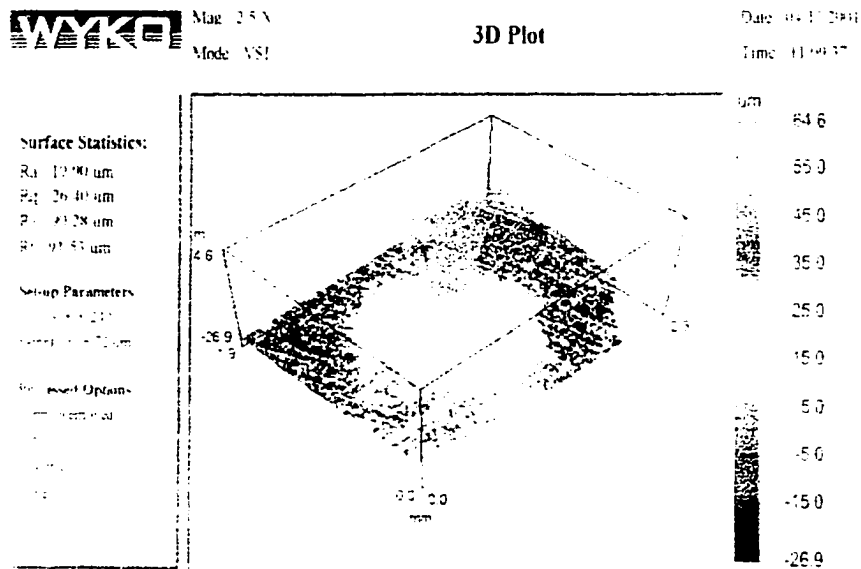


**Figure 4-8.** Surface quality of the Al apertures on the back of SIL tested by a Wyko NT-2000 interferometer.

#### 4.6 Summary

APSIL is successfully fabricated by a holographic exposure technique. The dielectric probe tips are probe height 400 nm, probe size 200 nm, and wall angle  $9^\circ$ , suggested in Chapter 3. NEFUS, which combines the laser optical system with the microscope, tests the fabricated APSIL with the edge-scan method. Results indicate resolution of  $200 \text{ nm}/e^2$  spot size and 50 % optical efficiency in reflection compared to the far field system. The pupil image shows that the APSIL system produces a wider angular spectrum than those produced by the far field system and the SIL system, although it has some unknown speckles.

An Al aperture + SIL is fabricated by a focused ion beam. The apertures are a rectangular shape with the size of  $200 \text{ nm} \times 350 \text{ nm}$ . Experimental results indicate that a large background reflection from the Al layer surrounding the aperture limits the detectable signal. The use of higher NA objective lens above  $NA = 0.5$  doesn't show improved detection. Al aperture - SIL is no good for detection.

## **CHAPTER 5**

### **HIGH-DENSITY RECORDING ON A PHASE-CHANGE MEDIUM**

#### **BY AN APSIL**

This chapter presents phase-change recording of the APSIL system. Tracking capability is demonstrated. Minimum mark size and the modulation transfer function (MTF) are evaluated experimentally.

#### **5.1 Introduction**

Current optical data storage technology requires not only reading data from optical disks, but also writing data to optical disks. Compact-Disc-Recordable (CD-R) and Compact-Disc-Rewritable (CD-RW) are widely used formats in CD recording drives. CD-R uses a dye medium as the recording layer and only can be written once. CD-RW uses a phase-change medium as recording layer and can be rewritten many times. Data density of a CD-R or CD-RW is mainly determined by the size of data marks written in the medium of the disk. In Chapter 5, our experiment with edge-scan test demonstrates that the APSIL system exhibits a readout resolution of 200 nm full-width  $1/e^2$  spot size and 50% optical efficiency in reflection. 200 nm spot size is one-eighth of the spot size in CD recording drive (1660 nm full-width  $1/e^2$  spot size). Thus, much smaller marks than those in CD-R or CD-RW (1800 nm) can be written with APSIL, and correspondingly higher capacity disks in the APSIL system are expected.

This chapter investigates characteristics of APSIL recording on a phase-change medium. The modulation transfer function (MTF) and minimum mark size are evaluated experimentally. In addition, the tracking capability of APSIL on a land-and-groove structure recording medium is demonstrated.

## 5.2 Experiment Setup and Near-field Recording Medium

A schematic of the experimental setup is shown in Figure 5-1. The arrangement of

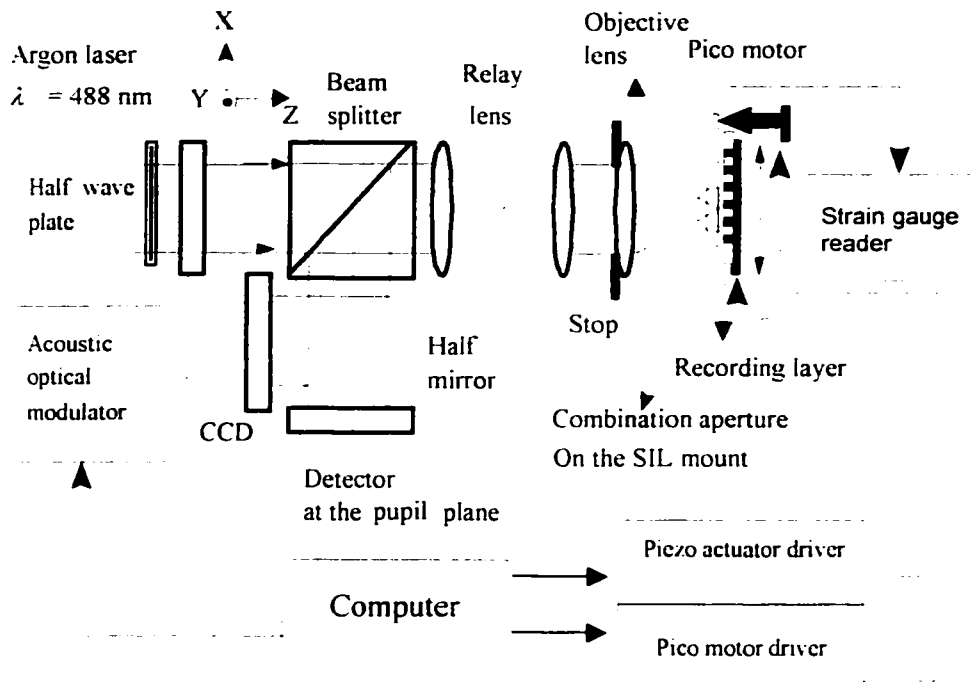


**Figure 5-1.** Schematic of the modified NEFUS for optical recording.

the experiment and operating procedure are similar to those described in Chapter 4, except the polarizing beam splitter and the quarter wave plate in Fig. 4-2 are replaced by a non-polarizing beam splitter and half wave plate. The half wave plate is used to change the polarization direction with respect to the tracks of the recording medium. In addition, an acoustic optical modulator is added to modulate the laser light for recording.

The near-field recording medium adopted for the experiment is a phase-change medium that is made from stripping the protective layer and reflective layer off a commercial IMATION CD-RW disk with a 1.6  $\mu\text{m}$  track pitch. The focused beam is incident onto recording layers from the backside, instead of the conventional approach of through-the-substrate recording. Figure 5-2 shows the recording medium structure with

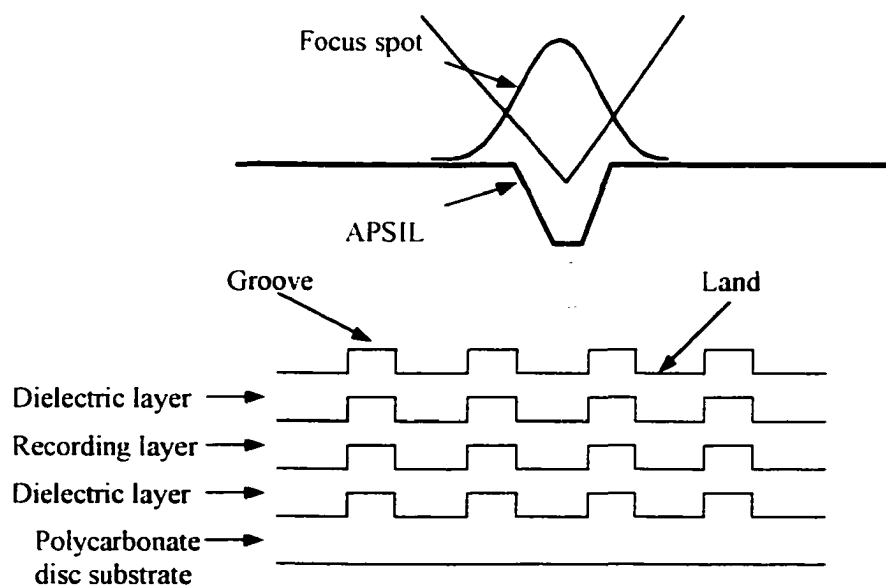


**Figure 5-2:** Composite layers of the recording medium for near-field recording.

the incident writing beam. The recording layer, which is a mix of silver, indium, antimony, and tellurium, is sandwiched between two layers of dielectric materials that draw excess heat from the recording layer. Our approach allows the evanescent energy from the probe tip to transfer to the recording layer. However, this medium from CD-RW is designed for illumination wavelength 780 nm. Since our experiment uses 488 nm wavelength, readout contrast and absorption during writing can be significantly affected. In addition, the medium is not designed for small marks.

### 5.3 Tracking Error Signal

In conventional CD-RW drive, a push-pull tracking error signal is generated when the readout or writing spot is not on track. The nature of the tracking error signal can be understood in terms of the diffraction of light from a grating structure of the disk [Wilson and Sheppard 1984]. As shown in Fig. 5-3, the diffracted order overlap is generated from the disk. When the spot shifts from the track center to the track edge, the irradiance of the overlap between 0<sup>th</sup> order and 1<sup>st</sup> order will differ from the irradiance of the overlap between 0<sup>th</sup> order and -1<sup>st</sup> order. The diffracted orders are collected by an objective lens and directed to the detection area by a beam splitter. The two-segment (A and B) detector senses the irradiance difference between two overlaps and generates push-pull track error signals. It is very important to understand if APSIL probes can be used for tracking, since no other aperture probe system has demonstrated tracking error signal in reflection due to its small collection area.

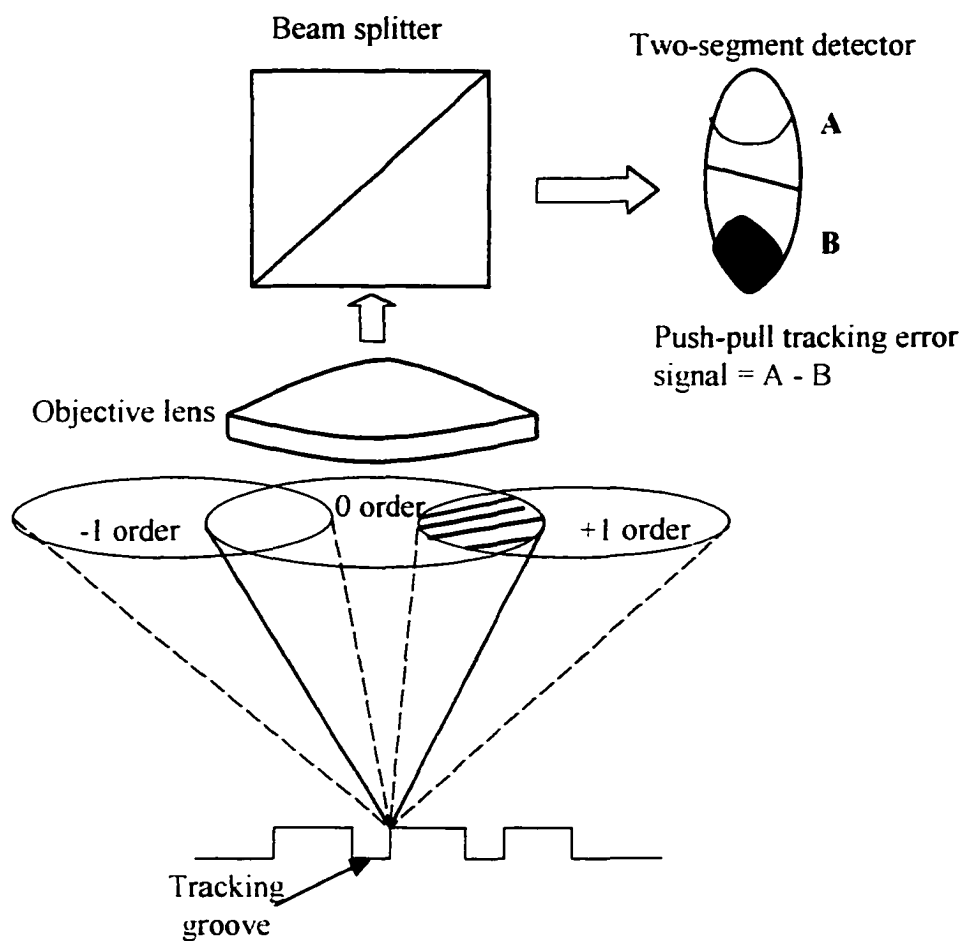


**Figure 5-3.** Schematic of push-pull tracking error signal generation.

Figure 5-4 shows a push-pull tracking error signal from the APSIL system when the light spot crosses several tracks of the recording medium. The phase structure of the medium is obtained by integrating the tracking error signal. As shown in Fig. 5-4, the medium is composed of a small groove of  $0.6 \mu\text{m}$  width and large land of  $1 \mu\text{m}$  width. A push-pull tracking error signal from scanning a phase grating of  $0.4 \mu\text{m}$  track pitch is also obtained from the APSIL system. The result is shown in Fig. 5-5.

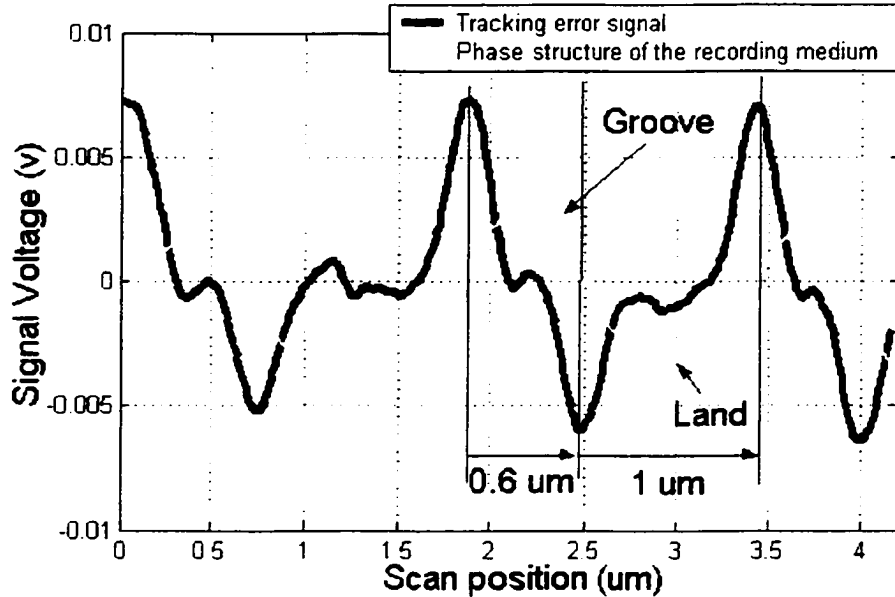


**Figure 5-4.** Tracking error signal from the phase-change medium of  $1.6 \mu\text{m}$  track pitch.

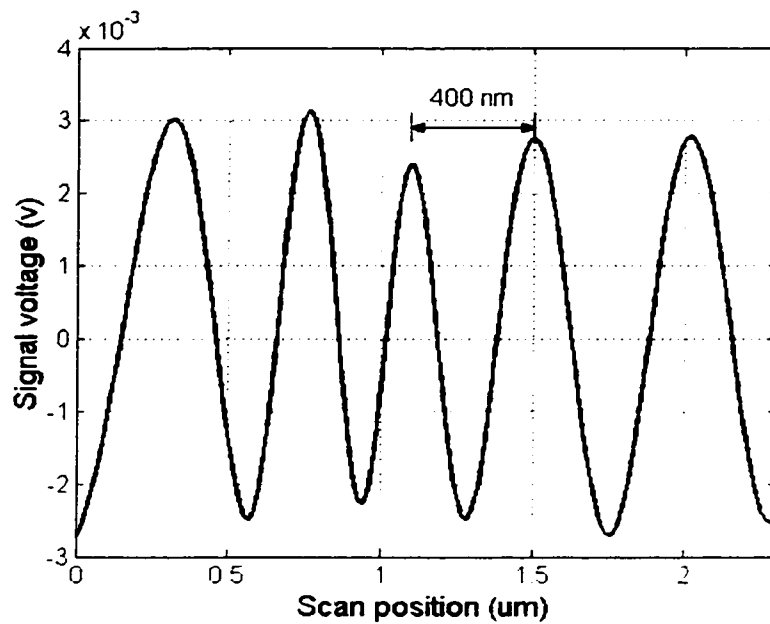


**Figure 5-5.** Tracking error signal from the phase grating of 0.4  $\mu\text{m}$  track pitch.

#### 5.4 Recording Experiment

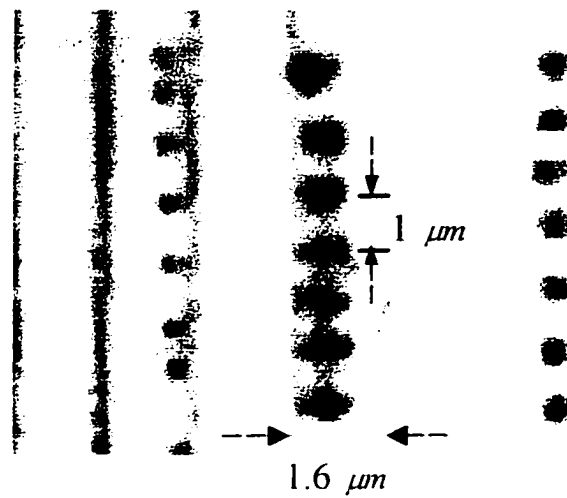
The recording experimental procedure is divided into two steps. The first step is static recording. The second step is non-static recording. For static recordings, the medium is not moving at the moment of data writing. Marks are written individually in a 'step and expose' series. For non-static recordings, marks are written while the medium is moving.

### 5.4.1 Static Recording

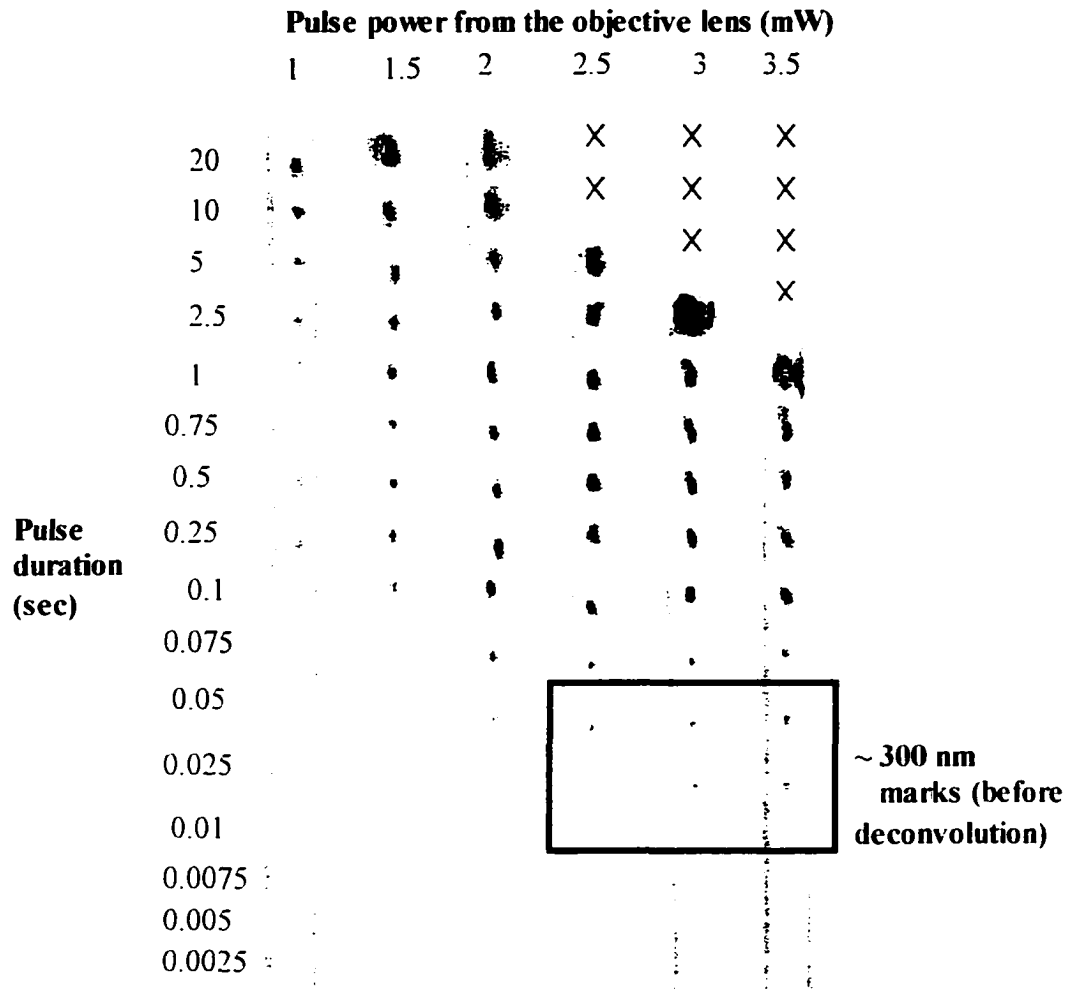
To gain insight to the recording performance of APSIL, static recording in large features of the recording medium (land) is adopted. Figure 5-6 shows recorded marks imaged by a visible light microscope. The marks are written by the laser beam modulated in 1 sec pulses and 1 mW in power out of the objective lens. As shown in the figure, three series of marks are written with spacing of approximately 1  $\mu\text{m}$  in the grooves of a phase-change medium. Mark diameters from far field, SIL and APSIL systems are 750 nm  $\pm$  80 nm, 500 nm  $\pm$  60 nm and 300 nm  $\pm$  60 nm. Mark widths are measured by determining the width of the mark with respect to the known track pitch of 1.6  $\mu\text{m}$ . Precision of the measurements is limited by the resolution of the optical microscope and the variability in the written marks. The point-spread function of the microscope, due to its 0.8 NA objective lens and 500 nm mean wavelength, was not deconvolved to reduce the mark size reported above. The APSIL system demonstrates good potential for high-density recording in comparison with far field and SIL systems. Small marks are easily written by APSIL, and the same laser power as a far-field system can be used with APSIL. No extra power is required.

Figure 5-7 shows a microscope image matrix of marks recorded in lands by static recording. In the matrix, each mark in the same column is written with different pulse duration but a constant power, and each mark in the same row is with a different power but constant pulse duration. The matrix shows the optimal range of the writing power is from 2.5 W to 3.5 W within the range of pulse duration from 10 ms to 50 ms, because ~

300 nm diameter marks are written consistently. The "x" sign in the matrix represents an overexposed mark



**Figure 5-6.** Visible light microscope image of three series of marks written along the vertical tracks of a phase-change medium by the systems of APSIL, far field and SIL, respectively (from left to right).



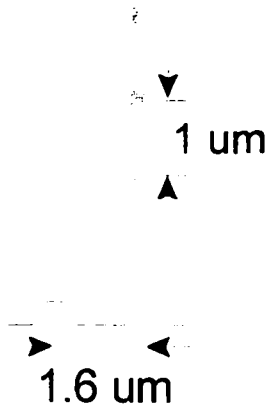
**Figure 5-7.** Microscope image of a matrix of recorded marks by the static recording. The power is measured from the object lens. The "X" sign in the matrix represents an overexposed mark.

### 5.4.2 Non-Static Recording

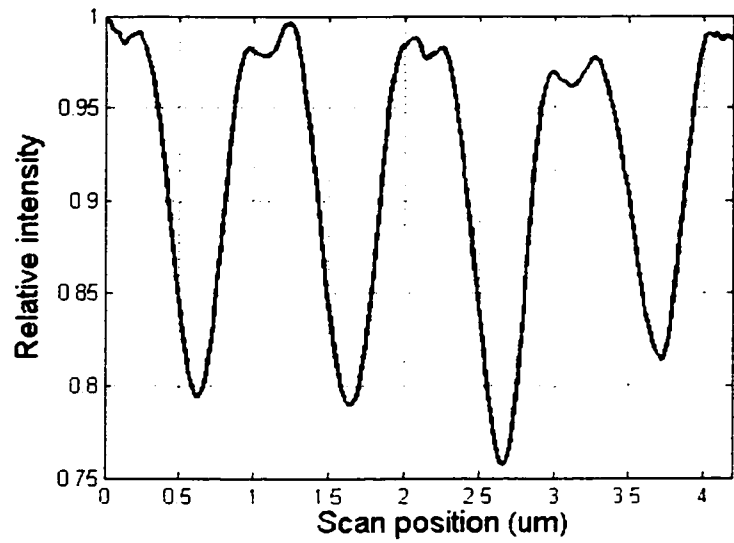
To evaluate the minimum mark size that can be written on the medium by the APSIL system, non-static recording on the groove of the medium is adopted. In non-static recording, the laser is modulated at various frequencies so that spacing between marks varies respect to the frequency as the sample stage is translated at a fixed velocity. While marks are written with increasingly tighter spacing, the challenge is to maintain good contrast during read back. Figure 5-8 (a) shows a microscope picture of a series of marks with 1  $\mu\text{m}$  spacing recorded by laser pulses of 2 mW at 12 Hz and 25% duty cycle from the objective lens. The APSIL readout signal is shown in Fig. 5-8(b), from which the contrast is 0.11. The result is comparable to the contrast of 0.14 from a large mark phase-change recording in a far-field system. The cause for the slightly smaller contrast in APSIL system may be from the back reflection off the flat side of the SIL.

Figure 5-9 (a) shows a microscope picture of a mark series with 500 nm spacing recorded with a laser pulse of 2 mW at 24 Hz and 25% duty cycle. The associated APSIL readout signal is shown in Fig. 5-9 (b), from which the contrast is 0.09. Figures 5-10 (a) and 5-10 (b) show APSIL readout signals from mark series with 333 nm and 250 nm spacing, respectively. Their corresponding readout contrasts are 0.05 and 0.03. Because the microscope used to observe the data marks cannot resolve the marks with spacing below 500 nm, microscope images are not displayed in Fig. 5-10 (a) and (b). Readout signal from a series mark with spacing 220 nm is obtained as well, but the contrast of the signal is difficult to measure, due to laser noise. Since 250 nm spacing mark series can be read back well, the minimum mark size written here is  $\sim 125$  nm.

(a)



(b)



**Figure 5-8.** Microscope image of non-static recording marks and their readout signal. The marks are recorded on a groove of the phase-change medium with  $1 \mu\text{m}$  spacing.

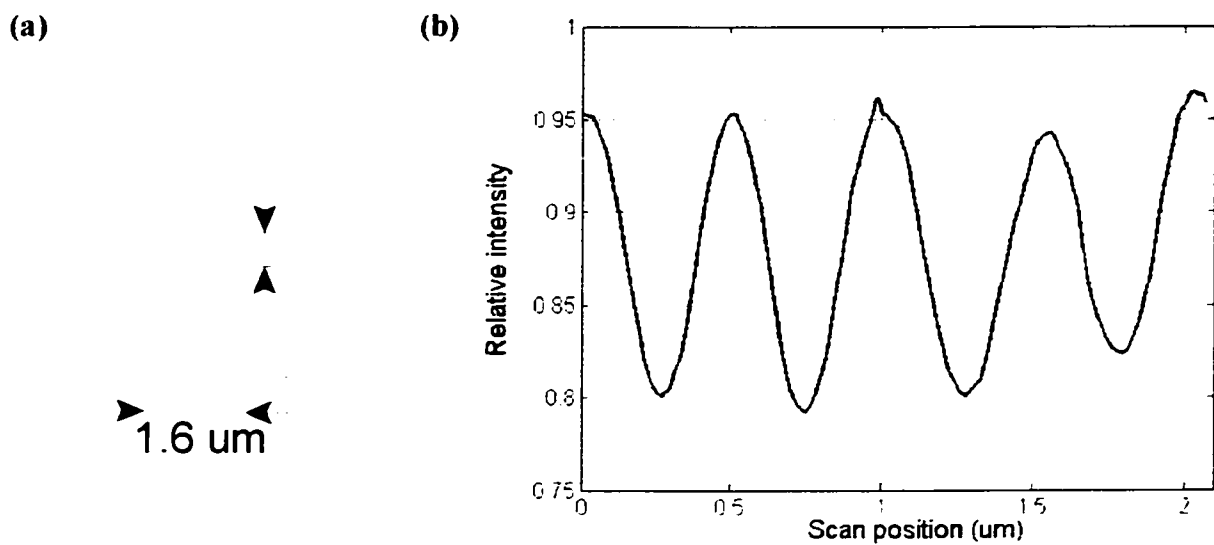
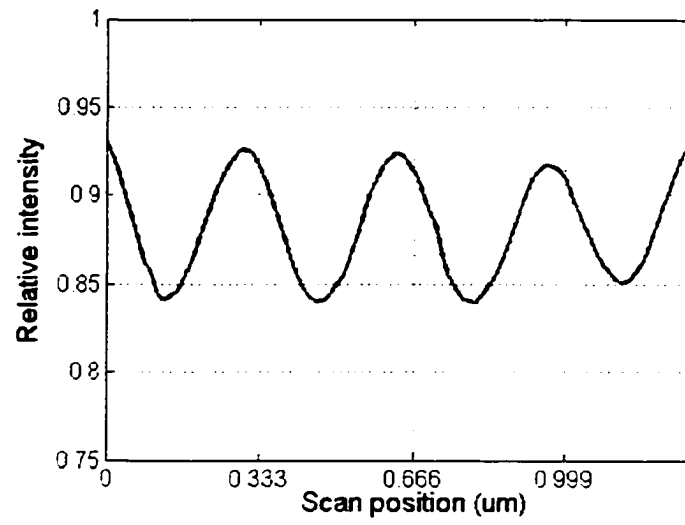


**Figure 5-9.** Microscope image of non-static recording marks and their readout signal. The marks are recorded on a groove of the phase-change medium with 500 nm spacing.

(a)



(b)

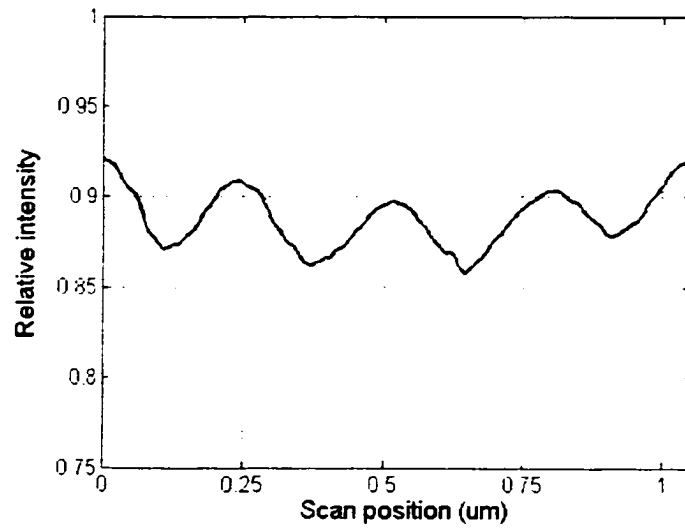


**Figure 5-10.** The readout signal from a series of marks with (a) 333 nm spacing and (b) 250 nm spacing.

Significance of the above result is that it provides a basis to obtain a Modulation Transfer Function (MTF) as shown in Fig. 5-11, which is a plot of contrast versus spatial

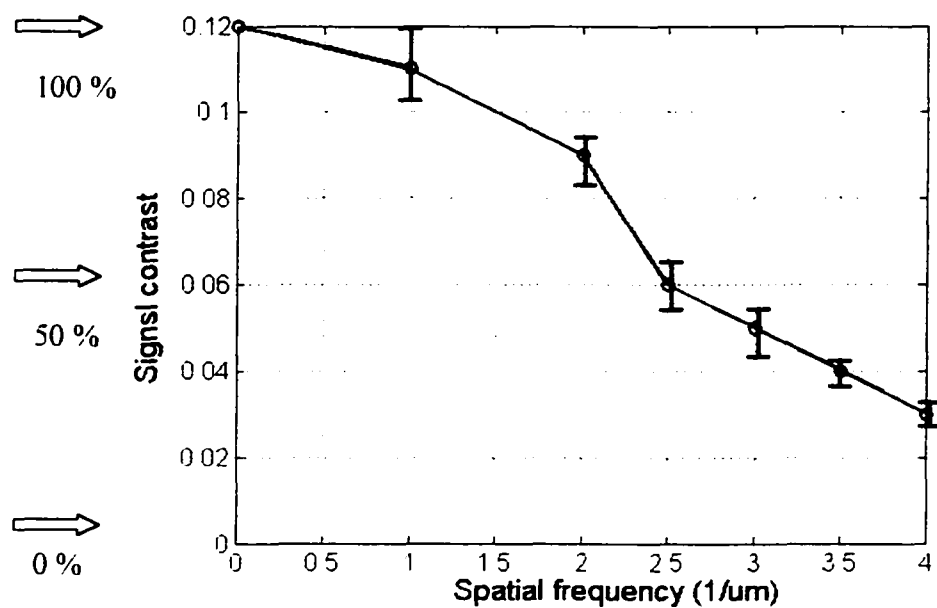


**Figure 5-11.** Experimental modulation transfer function (MTF) of the APSIL system. The cutoff frequency is beyond  $4 \mu\text{m}^{-1}$ .

frequency of the mark pattern. The 0.12 contrast at zero spatial frequency that corresponds to 100% MTF value is obtained when APSIL scans over a large mark. The low readout contrast below mark periods of 0.250  $\mu\text{m}$  is generated in part because the particular phase-change medium used in the experiment is not designed for this laser wavelength or these small marks. Even with these experimental obstacles, the experimental MTF exhibits a cutoff frequency beyond  $4 \mu\text{m}^{-1}$ .

## 5.5 Summary

APSIL system exhibits good phase-change recording performance. The phase-change medium is simply made from a commercial CD-RW. There are no extra layers on the medium to enhance the near-field performance. Tracking error signals are observed with the medium of track pitches of 1.6  $\mu\text{m}$  and 0.4  $\mu\text{m}$ , which indicates that APSIL can be used for tracking in reflection.

In static recording, a  $\sim 300$  nm mark can be written in the groove of the medium, which is smaller than those written by the far field system and SIL system with the same laser pulse. A matrix of data marks is exposed to show optimal range of writing power and writing pulse width for recording. In non-static recording, a series of data marks with 250 nm spacing is recorded and read back well on the lands of the medium. Minimum mark size is  $\sim 125$  nm. The APSIL MTF is obtained experimentally on CDRW media. The result shows that the maximum spatial frequency response of the APSIL system is beyond  $4 \mu\text{m}^{-1}$ .

## **CHAPTER 6**

### **CONSIDERATION AND CONTROL OF WRITING CONDITIONS WITH AN APSIL**

In this chapter, the control of writing conditions with an APSIL probe is investigated with respect to polarization, axial focus and transverse misalignment. Both FDTD simulation and experimental results are presented.

#### **6.1 Introduction**

In Chapter 5, the APSIL system is demonstrated dynamically for high-performance recording and read back with a simple structure phase-change medium. The experimental result shows that the MTF curve cutoff is beyond the spatial frequency of  $4 \mu\text{m}^{-1}$  and the minimum mark size is 125 nm. The 125 nm mark size is 3.2 times smaller than that of the conventional DVD system (400 nm). In other words, the areal capacity density of an APSIL disk has the potential to be 10 times larger than that of a DVD disk. With such progress of the APSIL system, it is important to understand consideration and control of writing conditions with an APSIL probe. Especially, study of writing conditions provides information about tolerance of the system alignments, which determines the value of designed system in practical use.

This chapter investigates control of writing conditions with respect to polarization direction of the illumination source, axial focus position of the objective lens, and beam transverse shift relative to the center of the probe by simulations and experiments. The

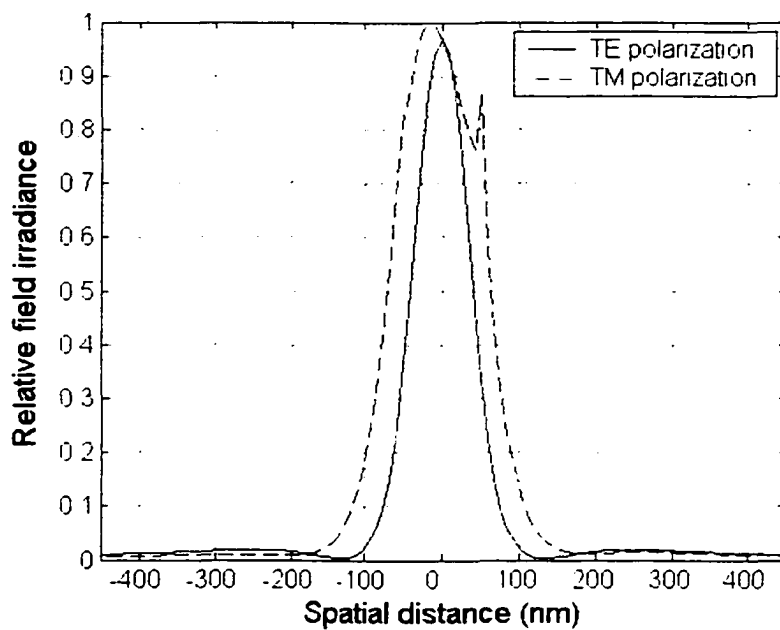
figure of merit for investigated parameters is quality of the spot generated by the probe, including spot size and position. FDTD simulation is used with the illumination of a current source 200 nm above the probe entrance plane, so the evanescent energy from the source cannot reach the entrance plane of the probe. The observation location is 20 nm below the exit plane of the probe. In experiment, an edge-scan test on a phase grating is adopted with the same setup as shown in Fig. 5-1. A half wave plate is used to change the polarization direction of the illumination. NEFUS allows axial focus adjustment. The picomotor is to move the APSIL in x or y directions relative to the illumination spot to change the alignment transversely. Both simulation and experimental results are compared to check consistency.

## 6-2 Polarization Effect

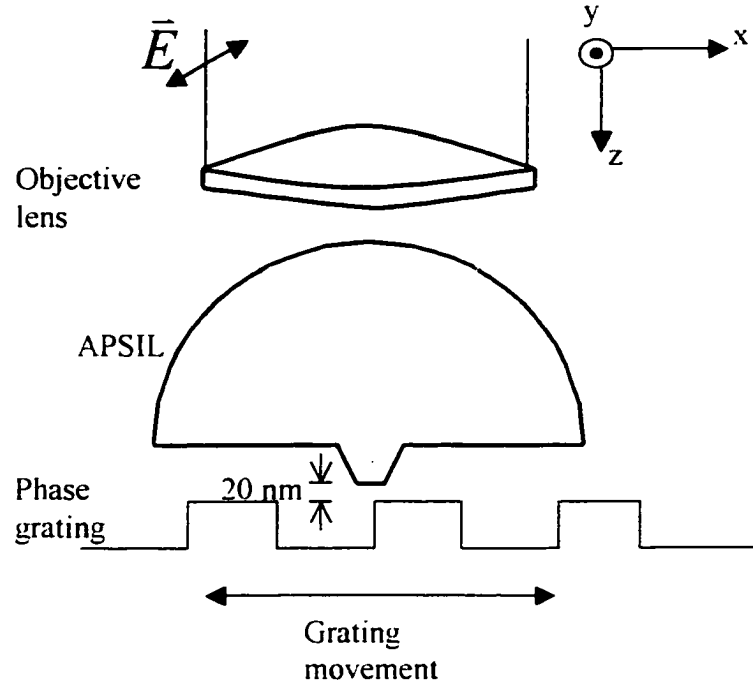
FDTD simulation is used to investigate effects of polarization on the spot profile in air. Figure 6-1 shows simulation results for TE and TM polarizations, respectively when the illumination of a current source is normal incident. As shown in the figure, the TE polarization spot profile is a gaussian shape with a smaller width while the spot profile of TM polarization is a super gaussian shape with a larger width. The  $1/e^2$  spot size difference between the two polarizations is about 50 nm.

Figure 6-2 shows an edge scan experiment setup performed for TE and TM polarization with a phase grating 20 nm away from the exit of the probe. TE polarization exhibits an oscillating electric field in the y direction and is parallel to the grooves of the grating. TM polarization exhibits electric field oscillation in the x direction and is

perpendicular to the grooves of the grating. The grating is translated along the  $x$  direction. Focus position of the objective lens is adjusted during the scan until the sharpest signals are obtained. Figure 6-3 shows the result that the signal curve of TE polarization is sharper than that of TM polarization. In addition, the  $1/e^2$  spot size of TE polarization is estimated to be 40 nm smaller than that of TM polarization.



**Figure 6-1.** FDTD simulation results of spot profile in air for TE and TM polarizations when the illumination of a current source is normal incident.



**Figure 6-2.** Experimental setup for the edge-scan test.

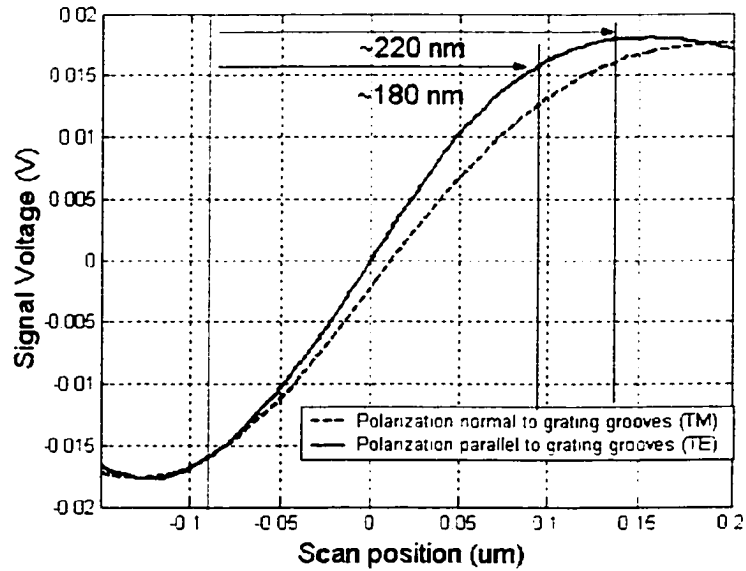


**Figure 6-3.** Experimental edge-scan results for TE and TM polarization

The shape of the spot profile can be outlined from the line-scan profiles of the recorded data marks from different writing powers, because the mark size is determined by the spot size of the writing beam above the threshold level of material phase-change in the recording medium. As shown in Fig. 6-1, the characteristic gaussian TE curve shows small top width and large base, while the characteristic super-gaussian TM curve shows a top width comparable to the base width. Thus, smaller marks can be written by the TE gaussian spot as the power decreases to the threshold level. Mark size can not be significantly reduced by the super-gaussian spot as the power decreases to the threshold level.

Figures 6-4 (a) and (b) show mark scan profiles for data written with TE and TM polarizations, respectively. Polarization of the readout beam in both figures is TE polarization. For TE plots, the  $1/e^2$  width of the scan profile decreases to 220 nm as the writing power is decreased from 2.5 mw to 1.5 mw. This behavior indicates that the spot profile of the writing beam is like a gaussian shape. For TM plots, the  $1/e^2$  width of the scan profile decreases to 280 nm from the writing power of 2.5 mW to 2 mW and then does not change from the writing power of 2 mW to 1.5 mW. This behavior of scan profile indicates that the spot profile of the writing beam is like a super-gaussian shape. Since the width of the scan profile is proportional to the mark size, TE polarized illumination can write smaller marks on the medium than those written by the TM polarized illumination.

Experimental results in Fig. 6-3 and Figs. 6-4 (a) and (b) show good agreement with the simulation results in Fig. 6-1. They both show that the TE polarization spot is

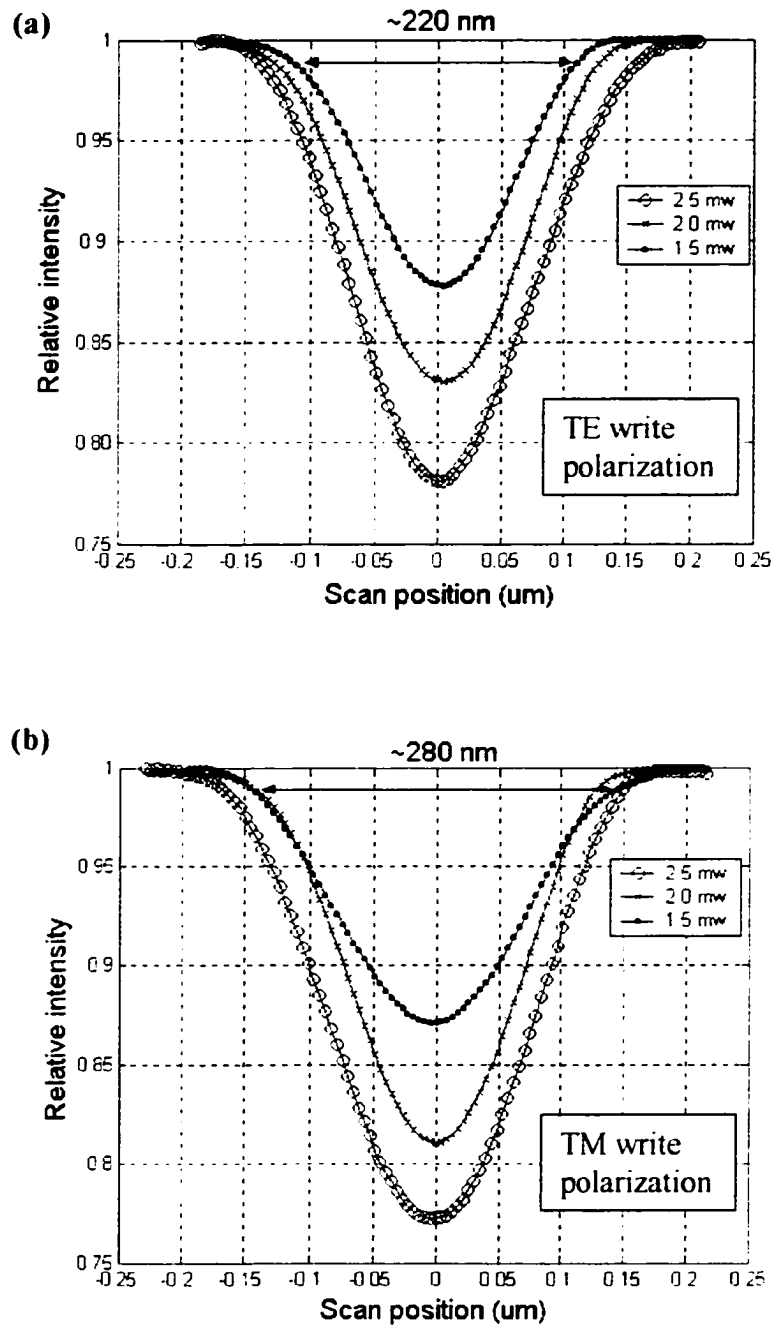


**Figure 6-4.** Mark-scan profiles for data written with (a) TE and (b) TM polarizations. The readout polarization is in the TE direction.

smaller and gaussian shaped, and TM polarization spot is larger and super-gaussian shaped. Therefore, the optimal polarization for the APSIL system is in the TE direction.

### **6-3 Axial Focus Position**

Effects of axial focus position of the objective lens on the spot profile generated by the probe is investigated by an edge-scan experiment. Two focus positions of the objective lens are used. One is to focus at the entrance plane of the APSIL probe; the other is to focus at the exit plane of the probe. The entrance and exit planes are separated by 400 nm. Figure 6-5 shows the outcome of the experiment with TE polarization readout. The signal curve with the focus at the exit plane is much sharper than that with the focus at the entrance plane. Spot size with the focus at the exit plane is estimated to be 190 nm, while the spot size with the focus at the entrance plane is estimated to be 360 nm. However, the light efficiency in reflection with the focus at entrance is 1.5 times better than that with the focus at the exit. Our prior edge-scan experiment with 50 % optical efficiency in reflection was obtained with the focus at the exit plane of the probe.

Axial focus position also produces an effect on the recorded mark size. Figure 6-6 shows a line-scan profile of two marks. The first is written by the focus position at the exit plane, and the second is written by the focus position at the entrance plane. Polarizations of the write beam and readout beam are in the TE direction. As shown in the Fig. 6-6, width and amplitude of the mark scan profile with the focus at the exit plane are smaller than those of the mark scan profile with the focus at the entrance plane. Both

experimental edge-scan results with a phase grating and experimental line-scan results with recorded data marks show that the optimal focus position of the objective is at the exit plane of the probe, because the spot size and recorded mark size are minimized.

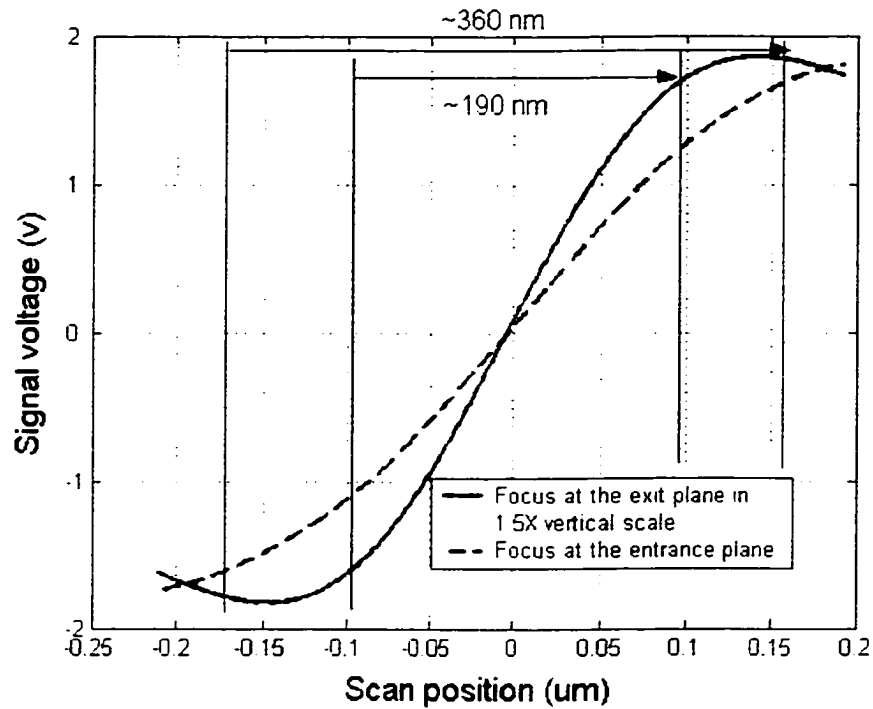


**Figure 6-5.** Edge-scan results for the axial focus position of the objective lens at the entrance plane of the probe and exit plane of the probe. The readout polarization is in the TE polarization.

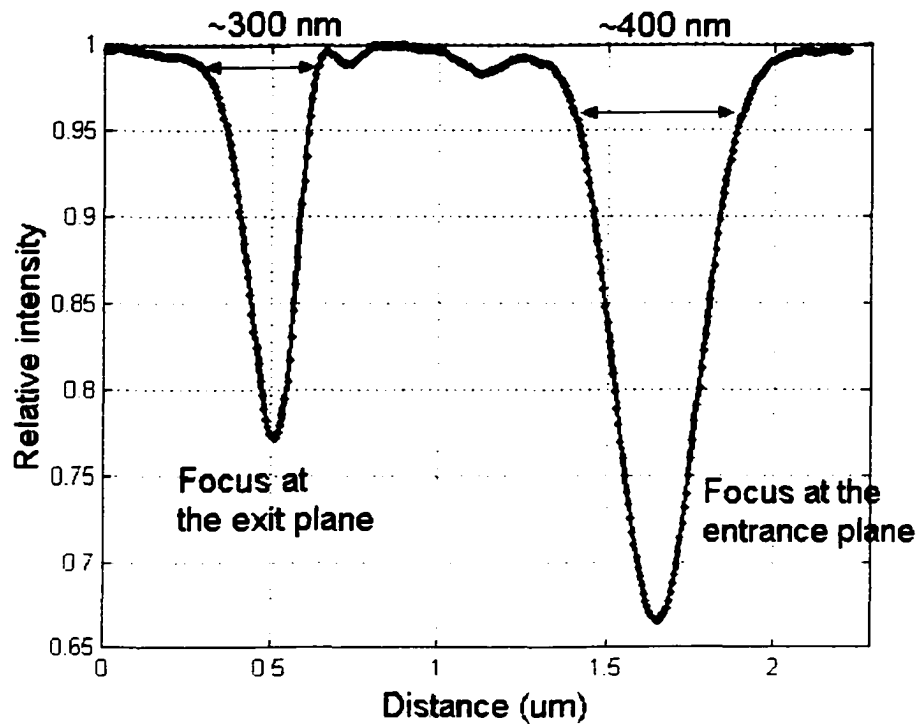


**Figure 6-6:** Line-scan profile of two marks written by the focus position at the entrance plane and exit plane. Polarization of the write beam and readout beam are in the TE direction.

#### 6-4 Transverse Misalignment

FDTD simulation is used to investigate effects of illumination beam misalignment with the center of the APSIL probe. Figures 3-10 (a) and (b) show simulation profiles in air of the TE polarization spot and TM polarization spot, respectively when the illumination of the current source has an incident angle  $\theta_m = 0^\circ, 12^\circ, 25^\circ, 37^\circ,$  and  $50^\circ$  with respect to the center of the probe. From Figs 3-10(a) and (b), changes in both

spot size and shift of the spot position relative to the center of the probe are observed in the TE direction as the incident angle increases. No significant changes in spot size and shift of the spot position are observed in the TM direction until  $\theta = 37^\circ$ .

Effect of the transverse alignment on the spot is also investigated by an edge-scan experiment with a phase grating 20 nm away from the exit plane of the probe. The axial focus position is at the exit plane of the probe, and the readout polarization is in the TE direction. Slope of the signal curve decreases and the position of the curve shifts as the APSIL moves transversely with TE polarization. No significant changes in detected signal with TM polarization occur until a large misalignment distance.

Figures 6-7 and 6-8 show a comparison between results from simulation and experiment with respect to spot size change and spot position shift relative to the center of the probe, respectively when the polarization is TE. The horizontal axes in both plots are misalignment distance relative to the center of the probe. The 0 in both horizontal axes indicates the position of the probe center, which was determined by the sharpest signals in the edge-scan experiment. In Fig. 6-7, the simulation curve and the experimental curve show good agreement on spot size change. If 30 nm spot size change is chosen as the system tolerance budget, the tolerance for transverse misalignment is about 70 nm. In Fig. 6-8, the simulation curve and experimental curve show a similar trend on spot position offset. The trend of the curves is not quite linear, which is different from that in SIL only system [Jo and Milster 2001]. In addition, both simulation and experiment show the spot shifting direction is opposite to the misalignment direction.

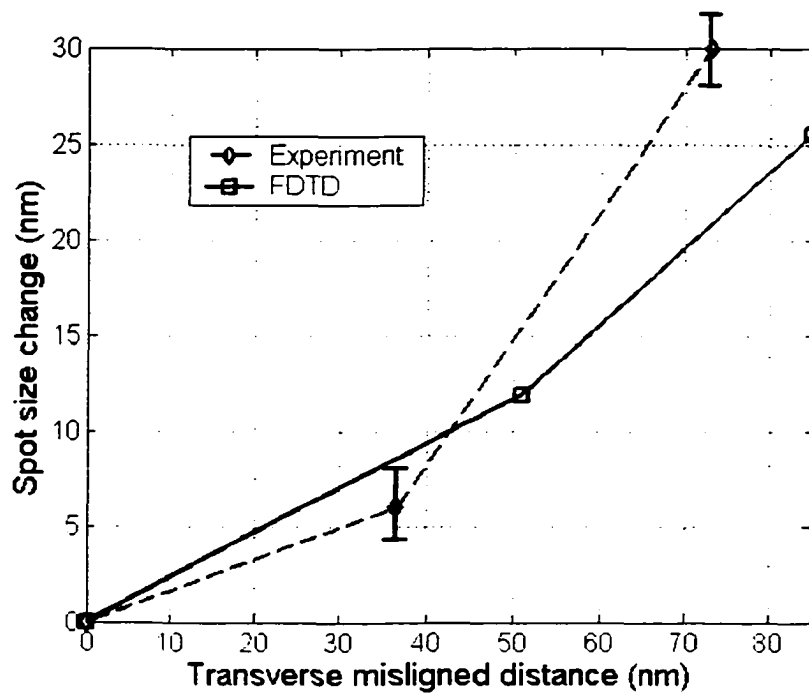


**Figure 6-7.** Comparison between results from simulation and experiment with respect to spot size change when the polarization is TE.

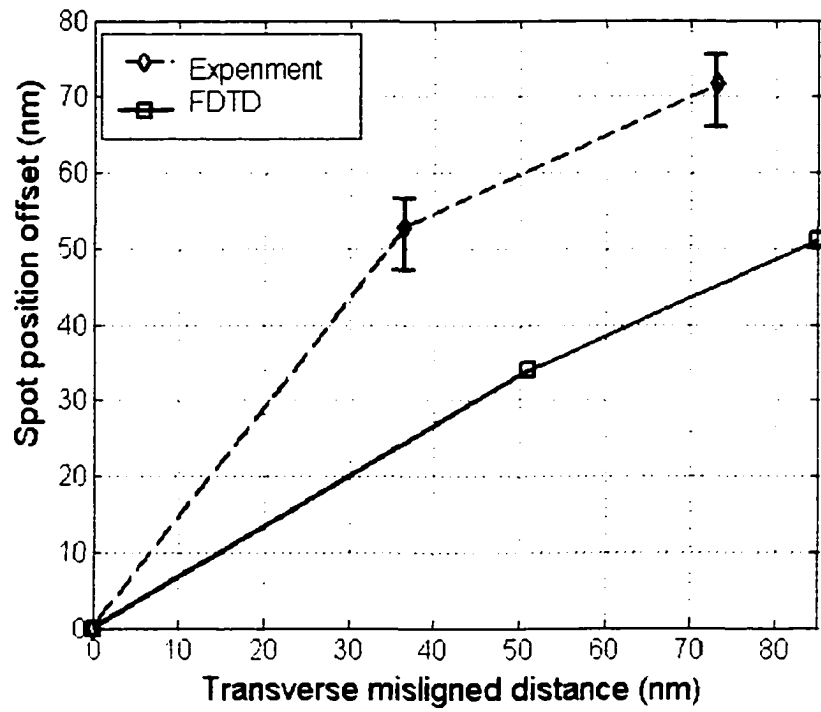


**Figure 6-8.** Comparison between results from simulation and experiment with respect to spot position shift relative to the center of the probe when the polarization is TE.

## 6-5 Summary

Control of writing conditions for an APSIL system are investigated with respect to polarization, axial focus position and the beam transverse misalignment. Both simulations and experiments are used in the investigation. For polarization sensitivity, both FDTD simulation and edge-scan experiments show that the TE polarization spot generated by the probe is smaller than that of TM polarization. In addition, the TE polarization spot shape is like a gaussian distribution and the TM polarization spot shape is like a super-gaussian distribution. Due the size and shape of the spot, smaller marks are written on the medium with the writing beam in TE polarization orientation. With respect to axial focus position of the objective lens, an edge-scan experiment shows that smaller spots are generated with the focus position at the exit plane of the probe than at the entrance plane of the probe. The line-scan experiment also shows that smaller marks are written on the medium with the focus position at the exit plane of the probe. With respect to beam transverse misalignment, spot size change and spot position shift relative to the center of the probe are observed with TE polarization from the simulation and experiment. The tolerance for the beam transverse misalignments is about 70 nm. The spot offset approaches a limit with increasing misalignment distance, which is different from the linear relationship between spot offset and misalignment in a SIL system. Spot size and spot position are not sensitive to transverse misalignment with TM polarization.

## Chapter 7

### CONCLUSION AND FUTURE WORK

#### 7-1 Summary of the Dissertation

This dissertation proposes and demonstrates an innovative technique for ultra-resolution data storage. An original idea that combines two near-field techniques, aperture probes and the SIL, is implemented through modeling, fabrication, testing, phase-change recording, and writing condition studies.

In the modeling, a theory for illumination and signal detection is presented. The power transmission for different near-field transducers illuminated by a lens is calculated versus  $NA$ . A concept of angular selectivity is introduced for near-field transducers, which is found to be a determining factor for the transmission. APSIL, with a broad range of angular selectivity, exhibits superior power transmission compared to AI aperture + SIL, AL aperture, and plasmon-enhanced hole transducers. Plasmon-enhanced holes have very poor transmission due to a narrow range of angular selectivity. In detection, the angular spectrum illustrates advantages of the APSIL system due to wider angular range and larger collection area than a SIL and an aperture probe separately.

Geometrical design considerations are discussed with the modeling. Preferred designs for APSIL and AI aperture + SIL are presented for the illumination wavelength 488 nm. In the APSIL transducer design, probe height 400 nm, probe size 200 nm, and wall angle  $9^\circ$  are chosen due to good spot profile for normally incident light. We also found that probe size smaller than 200 nm cannot reduce the spot size. In the AI aperture

+ SIL transducer design, a  $\lambda/3n \times \lambda/2n$  rectangular hole shape with aluminum thickness of 100 nm shows good performance with respect to spot profile.

Fabrication techniques are developed for APSIL and Al aperture + SIL, respectively through modeling geometrical design. APSIL is fabricated by a holographic exposure technique. An array of dielectric conical probe tips is formed on the bottom of the SIL, although only one of them is used at the time in the experiments. An advantage of using an array of probes is to reduce alignment difficulty. Al aperture + SIL is fabricated by a focused ion beam milling through a homogeneous Al layer. The rectangular shape is well preserved.

$200\text{nm}/e^2$  full-width spot size and 50 % optical efficiency in reflection are measured from the APSIL system by an edge-scan test on a phase grating. The pupil image from the grating shows that APSIL has a wider angular spectrum than SIL or far-field systems. The result agrees with our theory developed for signal detection. Unknown speckles are observed in the pupil, which are probably due to the light scattering off the probe tips. Al aperture + SIL shows very poor performance in signal detection. Experimental results indicate that a large background reflection from the Al layer surrounding the aperture limits the detectable signal.

APSIL is evaluated for high-density recording on a phase-change medium. In a static recording experiment,  $\sim 300$  nm marks are written in the lands of the medium, which are smaller than those written by the SIL or far-field systems with the same laser pulse. In a non-static recording experiment, 125 nm marks are written on the grooves of

the medium. Modulation transfer function (MTF) of the APSIL is evaluated through the non-static recording experiment. The cut-off frequency is beyond  $4 \mu\text{m}^{-1}$ . In addition, the APSIL system demonstrates tracking error signals in reflection from the groove structures with track pitch 1600 nm and 400 nm.

Control of writing conditions for an APSIL system are investigated with respect to polarization, axial focus position and transverse beam alignment. Both simulation and experiment show that the optimal polarization is TE polarization, which generates the smallest spot and a gaussian shape. TM polarization generates a larger spot with a super-gaussian shape. Optimal focus position of the objective lens is at the exit plane of the probe. Experiment results show that smaller spots and smaller marks are observed with the focus position at the exit of the probe, compared to those with the focus at the entrance of the probe. With respect to transverse misalignment, spot size change and spot position shift relative to the center of the probe are observed with TE polarization from simulation and experiment. The spot size increases 30 nm with misalignment of 70 nm. The spot offset approaches a limit with increasing misalignment distance, which is different from the linear relationship between spot offset and misalignment in SIL systems. Spot size and spot position are not sensitive to transverse misalignment with TM polarization.

## 7-2 Significant Results from an APSIL

Our research on near-field APSIL probes makes significant progress on the throughput of sub-wavelength aperture probe technology. The APSIL probe is demonstrated to have 50% optical efficiency in reflection. Thus, > 50% power transmission is achieved, which is about 1 or 2 decades larger than any other developed aperture probes. In addition, APSIL is also demonstrated for tracking in reflection mode, which is the first demonstration of this type with an aperture probe. APSIL is a revolutionary advance of SIL technology. With a small aperture probe attached to the bottom of the SIL, the spot size can be easily reduced without reducing wavelength or increasing the refractive index of SIL and NA of the illumination lens.

APSIL with 488 nm wavelength illumination is observed to produce 200 nm  $1/e^2$  spot size. Compared with a spot size in commercial CD drive (1660 nm) and DVD drive (1080 nm), the spot size in the APSIL system allow the capacity of the disk to be greatly increased. Thus, based on spot size only, the APSIL disk has the potential to yield a factor of 25X the capacity of DVD disks (4.7 GB).

The optical recording performance by the APSIL shows 125 nm minimum mark size and  $4 \mu\text{m}^{-1}$  spatial frequency response. This performance doesn't quite meet to our expectation for the 200 nm spot size. Compared with the minimum mark size in a DVD (400 nm), the mark size is only reduced by a factor of 3.2X. Thus, based on mark size, the APSIL disk only yield a factor of 10X the capacity of DVD disks. In addition, the most recent results from the supersphere SIL system developed in Sony Corporation are

107 nm minimum mark size and  $4.6 \mu\text{m}^{-1}$  frequency response [Kishima *et al.* 2002]. However, the use of small wavelength 405 nm and large marginal ray angle  $50^\circ$  in Sony system may cause tighter tolerance on the element quality and system alignment than the APSIL system. The phase-change medium in their experiment has been optimized for near-field recording by adding a dielectric stack to the recording layer while our medium is made from a commercial CD-RW for 780 nm wavelength without any extra layers on the recording layer.

### **7-3 Suggestions for Future Work**

Additional works are required to improve the optical recording performance as well as to extend the applications in different techniques and other scientific areas. Suggestions for future work include:

- 1) Determination of spot size limit from APSIL. Our simulation study shows that the spot size cannot be further reduced when only decreasing the probe size. The appropriate condition of illumination wavelength, numerical aperture, refractive index of SIL, and probe geometry for producing smaller spot size than 200 nm needs to be investigated. Supersphere SIL may be our choice for APSIL for smaller spot size.
- 2) Development of phase-change medium for near-field recording. The phase-change recording layer is easily ablated by the strong heat from the APSIL probe,

so the recording performance is limited. Protective layers should be added on the recording layer of the media to improve the recording.

- 3) Upgrade of the experiment setup to real dynamic system. Unlike commercial optical data storage systems, our APSIL system cannot read and write data on a spinning disk, due to the lack of dynamic focus and tracking control systems, as well as lack of an air bearing to regulate the air gap. With a dynamic APSIL system, important information such as jitter, data rate, and carrier-to-signal ratio (SNR) can be obtained.
- 4) Extensions of APSIL to other applications, such as biology. APSIL probes can be used in near-field optical microscopy (NSOM) for recognizing and examining human tissues or other biological samples. Due to the high throughput of APSIL, data processing time can be greatly reduced when scanning over large areas of the sample.

## REFERENCES

- Akai, M. M., R. J. Blaikie and S. J. S. O. McNab: *J. Vac. Sci & Technol.* **B16** (1998) 3929.
- Ash, E. A. and G. Nicholls, " Super-resolution aperture scanning microscope, " *Nature* **237**, 510-512 (1972).
- Bethe, H. A., "Theory of Diffraction by small holes," *Phys. Rev.* **66**, 163-182 (1944).
- Betzig, E., M. Isaacson, and A. Lewis, "Collection mode near-field scanning optical microscopy," *Appl. Phys. Lett.* **51**, 2088-2090 (1987).
- Betzig, E., J. K. Trautman, R. Wolfe, E. M. Gyorgy, and P. L. Finn, M. H. Kryder, C. H. Chang, "Near-field magneto-optics and high density data storage," *Appl. Phys. Lett.* **61**, 142-144 (1992).
- Chen, F. and E. Schlesinger, The metallic apertures are fabricated at Carnegie Mellon University.
- Fischer, U. Ch. And D. W. Pohl, "Observation of single-particle plasmons by near-field optical microscopy," *Phys. Rev. Lett.* **62**, 458-461 (1989).
- Ghaemi, H. F., Tineke Thio, D. E. Grupp, T. W. Ebbesen, and H. J. Lezec, "Surface plasmons enhance optical transmission through subwavelength holes," *Phys. Rev.* **58**, 6779-6782 (1998).
- Grupp, D. E., H. J. Lezec, T. Thio, and T. W. Ebbesen, "Beyond the Bethe limit: tunable enhanced light transmission through a single sub-wavelength aperture," *Adv. Mater.* **11**, 860-862 (1999).
- Harootunian, A. E. Betzig, M. Isaacson, and A. Lewis, "Super-resolution fluorescence near-field scanning optical microscopy," *Appl. Phys. Lett.* **49**, 674-676 (1986).
- Haskal, H. M., "Laser recording with truncated Gaussian beams," *Appl. Opt.* **18**, 2143-2146 (1979).
- Hirota, K., J.S. Jo, and T. D. Milster, "High density phase change optical recording using a solid immersion lens," *Proc SPIE* **3401**, 34-39 (1988).

**REFERENCES-Continued**

Hirota, K., T. D. Milster, K. Shimura, Y. Zhang, and J. S. Jo, "Near-field phase change optical recording using a GaP hemispherical lens," *Jpn. J. Appl. Phys. Part 1* **39**, 968-972 (2000).

Hirota, K., T. D. Milster, Y. Zhang, and J.K. Erwin, "Design of a near-field probe for optical recording using a 3-dimensional finite difference time domain method," *Jpn. J. Appl. Phys.* **39**, 973-975 (2000).

Ichimura, Isao, Koichiro Kishima, Kiyoshi Osato, Kenji Yamamoto, Yuji Kuroda, and Kimohiro Saito, "Near-field phase-change optical recording of 1.36 Numerical Aperture," *Jpn. Appl Phys.* **39**, 962-967 (2000).

Jo, J. S. T. D. Milster, "Tolerance issues in solid immersion lens systems". *Proc. of SPIE.* **4342**, 312 (2001).

Kishima, Koichiro, Isao Ichimura, Kimihiro Saito, Kenji Yamamoto, Yuji Kuroda Atsushi Iida, Shin Masuhara, and Kiyoshi Osato, "Challenge of near-field recording beyond 50.4 Gbit/in<sup>2</sup>," *Jpn. J. Appl. Phys.* **41**, 1894-1897 (2002).

Mansfield, S. M. and G. S. Kino, "Solid immersion microscope," *Appl. Phys. Lett.* **57**, 2615-2616 (1990).

Milster, T. D., J. S. Jo, and K. Hirota, "Roles of propagating and evanescent waves in solid immersion lens systems," *Appl. Opt.* **38**, 5046-5057 (1999).

Milster, T. D., "Near-field optics: a new tool for data storage," *Proceeding of the IEEE* **88**, 1480-1490 (2000).

Milster, T. D., "Near-field optical data storage: avenues for improved performance," *Opt. Eng.* **40**, 2255-2260 (2001).

Milster, T. D., F. Akhavan, M. Bailey, J. K. Erwin, D. M. Felix, K. Hirota, S. Koester, K. Shimura, and Yan Zhang, "Super-resolution by combination of a solid immersion lens and an aperture," *Jpn. J. Appl. Phys.* **40**, 1778-1782 (2001).

Partovi, A., D. Peale, M. Wutting, C. A. Murray, G. Zydzik, L. Hopkins, K. Baldwin, W.S. Hobson, J. Wynn, J. Lopata, L. Dhar, R. Chichester, and J. H. Yeh, "High power laser light source for near-field optics and its application to high-density optical data storage." *Appl. Phys. Lett.* **75** 1515-1517 (1999).

## REFERENCES-Continued

Pohl, D. W., W. Denk, and M. Lanz, "Optical stethoscopy: image recording with resolution  $\lambda/20$ ," Appl. Phys. Lett. **44**, 651-653 (1984).

Shimura, K., T. D. Milster, J. S. Jo, and K. Hirota, "Pupil plane filtering for optical pickup heads operation with effective numerical aperture of 1.1 and 2.0," Jpn. J. Appl. Phys. Part 1 **39**, 897-901 (2000).

Synge, E. H., "A suggested method for extending microscopic resolution into the ultra-microscopic region" Philo. Mag. **6**, 356-362 (1928).

Taflove, Allen, *Computational electrodynamics the finite-difference time-domain method* (Artech House, Boston, 1995), Chap. 2 pp. 35-50.

Terris, B. D., H. J. Mamin, D. Rugar, W. R. Studenmund, and G. S. Kino, "Near-field optical data storage using a solid immersion lens," Appl. Phys. Lett. **65**, 388-390 (1994).

Terris, B. D., H. J. Mamin, and D. Rugar, "Near-field optical data storage," Appl. Phys. Lett. **68**, 141-143 (1996).

Thio, Tineke, K. M. Pellerin, R. A. Linke, H. J. Lezec, and T. W. Ebbesen, "Enhanced light transmission through a single subwavelength aperture," Opt. Lett. **26**, 1972-1974 (2001).

Tieke, B. M. Dekker, N. Pfeffer, R. van Woudenberg, G-F. Zhou, and I. P. D. Ubbens, "High data-rate phase-change media for the digital video recording system," in Proc. SPIE joint Int. Symp. Optical Memory and Optical Data Storage. **3864**, 200-202 (1999).

Wilson, Tony and Colin Sheppard, *Theory and practice of scanning optical microscopy* (Academic Press, London, 1984), Chap. 7 pp. 165-193.

Yatsui, T., K. Itsumi, M. Kouroggi, and M. Ohtsu, "Metalized pyramidal Silicon probe with extremely high throughput and resolution capability for optical near-field technology," Appl. Phys. Lett. **80**, 2257-2259 (2002).